

Probing chemical structures and physical processes with nanopores

THÈSE N° 7082 (2016)

PRÉSENTÉE LE 6 JUILLET 2016

À LA FACULTÉ DES SCIENCES ET TECHNIQUES DE L'INGÉNIEUR
LABORATOIRE DE BIOLOGIE À L'ÉCHELLE NANOMÉTRIQUE
PROGRAMME DOCTORAL EN PHYSIQUE

ÉCOLE POLYTECHNIQUE FÉDÉRALE DE LAUSANNE

POUR L'OBTENTION DU GRADE DE DOCTEUR ÈS SCIENCES

PAR

Jiandong FENG

acceptée sur proposition du jury:

Prof. M. Q. Tran, président du jury
Prof. A. Radenovic, directrice de thèse
Prof. M. Mayer, rapporteur
Prof. M. Wanunu, rapporteur
Prof. Ph. Renaud, rapporteur



ÉCOLE POLYTECHNIQUE
FÉDÉRALE DE LAUSANNE

Suisse
2016

Abstract

This thesis develops and applies the nanopore tool to probe chemical structures and physical processes at the single-molecule level: from single ions to DNA molecules. Nanopore experiments electrically measure the ionic transport through the pore and its modulation from the local environment which can be caused by translocations of an analyte such as objects like DNA molecules or change of the physical conditions such as surface charge. Its precision relies on the physical dimension of the nanopore probe. In this thesis, the atom by atom engineering of single-layer molybdenum disulfide (MoS_2) nanopores was achieved using transmission electron microscopy (TEM) or controlled electrochemical reaction (ECR), which further enabled the following investigations.

On the translational side, the key driver of the application of nanopores is single molecule DNA sequencing. The sequence of DNA can be extracted based on the modulation of ionic current through the pore by individual nucleotides. To this end, we realized for the first time with solid-state nanopores, identification of all four types of nucleotides by introducing an ionic liquid based viscosity gradient system to control the translocation dynamics. This method provides a potential route for sequencing with solid-state nanopores.

On the fundamental side, nanopore experiments could probe physics of single ion transport and with subnanometer pores, we discovered Coulomb blockade for the first time in ionic transport, as the counterpart of quantum dots, and proposed a new mesoscopic understanding for biological ion channel transport.

From an engineering perspective, measurement with a single nanopore can avoid averaging over many pores and allow accurately identifying individual parameters for membrane-based processes. With single-layer MoS_2 nanopores, we realized the first exploration of a two-dimensional (2D) membrane for osmotic power generation.

This thesis demonstrates that nanoscopic, atomically thin pores allow for the exploration of applications in DNA sequencing and investigations of fundamental ion transport for biological ion channels and membrane-based processes.

Keywords

Nanopores, DNA sequencing, ion transport, Coulomb blockade, osmotic power generation

Résumé

Cette thèse développe et applique l'outil du nanopore pour sonder les structures chimiques et les processus physiques au niveau d'une seule molécule : des ions simples jusqu'aux molécules d'ADN. Les expériences de nanopore mesurent électriquement le transport ionique à travers le pore et sa modulation due à l'environnement local qui peut être modifiée par des translocations d'un analyte tels que des molécules d'ADN ou des changements des conditions physiques telles que la charge de surface. Sa précision dépend de la dimension physique de la sonde nanopore. Dans cette thèse, la construction, atome par atome, d'un nanopore dans une monocouche de disulfure de molybdène (MoS_2) a été réalisée en utilisant la microscopie électronique à transmission (MET) ou par réaction électrochimique contrôlée (REC). Cela a en outre permis aux investigations suivantes.

Du côté translationnel, le principal moteur de l'application des nanopores est simple : le séquençage de la molécule d'ADN. La séquence d'ADN peut être extraite en fonction de la modulation du courant ionique à travers le pore par les nucléotides individuels. À cette fin, nous avons réalisé pour la première fois avec des nanopores à l'état solide, l'identification de tous les quatre types de nucléotides en introduisant un gradient de viscosité grâce à un liquide ionique pour contrôler la dynamique de translocation. Cette méthode fournit une voie potentielle pour le séquençage avec des nanopores à l'état solide.

Du côté fondamental, des expériences de nanopores pourrait sonder la physique du transport d'ions et, avec des pores subnanométrique, nous avons pu découvrir pour la première fois le blocage de Coulomb pour le transport ionique, comme sa contrepartie liée aux points quantiques, et avons proposé une nouvelle compréhension mésoscopique pour le transport des canaux ionique biologique.

Du point de vue de l'ingénierie, la mesure avec un seul nanopore peut éviter la moyenne sur de nombreux pores et permettre d'identifier avec précision les paramètres individuels pour les procédés membranaires. Avec un nanopore dans une seule couche de MoS_2 , nous avons réalisé la première utilisation d'une membrane à deux dimensions (2D) pour la production d'énergie osmotique.

Cette thèse démontre que les pores nanoscopiques et atomiquement minces permettent l'exploration d'applications dans le séquençage de l'ADN et des enquêtes fondamentales sur le transport des ions dans les canaux ioniques et les processus biologiques membranaires.

Mots Clés

Nanopores, séquençage d'ADN, transport d'ions, blocage de Coulomb, génération osmotique de puissance

Acknowledgment

I enjoyed doing my PhD at EPFL and this is because of many reasons. One of them lies on the Lac Lemman which allows me doing windsurfing in the summer. I also feel lucky to work in EPFL since EPFL provides me the chance to explore science in the way I want owing to its bountiful resources and this cannot happen without the following people.

My thesis advisor-Prof. Aleksandra Radenovic. I have to say I would not have the opportunity to finish my PhD in three years at the age of 24 without her support. The whole story of this PhD started from Aleksandra's support for me to be admitted to EPFL doctoral school without a master degree and this is rare in any European university. Every thesis involves a huge amount of frustrations, in particular at the starting point, and mine was not an exception. However, Aleksandra encouraged me to continue and allowed me to find the way that I would love to work. She is able to find and advise students to exploit their strengths. For example, through my PhD, I was encouraged to largely use my advantage in interdisciplinary knowledge to lead my PhD research. On the other side, she has always been motivating me to improve my software skills. I feel very fortunate and grateful that she could find my advantage and provide me the freedom. Aleksandra is always positive and supportive in research. I always come up with some new ideas and it is her who convinces and supports me to make all these things practically happen. Her enthusiasm and love to science are admirable. One of the many remarkable things about Aleksandra is her ability to find the most exciting topics at very early stage and her courage to enter a new field, which is also reflected in the diversity of the LBEN lab. I am also surprised by her versatility in technology skills, knowledges and even languages, particularly when I knew Aleksandra studied Latin for 8 years. Aleksandra could also find the best resources of the world to use, including both facilities and collaborators. I would like to thank Aleksandra for all the discussions we had and the hard time we suffered together during the peer-review process of the papers we published. It is Aleksandra and the LBEN lab who helped me to delivery these imaginations into practice, which is detailed later in this thesis. I also benefited a lot from the interdisciplinary nature of the lab and I learnt about serveral other topics outside of my thesis from Aleksandra. Last but not least, I am always taught by Aleksandra to persevere when things get difficult, such as motivating me for pursuing the next career. In the Chinese proverb, I think Aleksandra's role of supervising my PhD is comparable to *BoLe who is a horse-judging master in discovering swift horses*.

I have great times with LBEN people both in our lab and beer sites. I would also like to thank Dr. Ke Liu. We joined the lab at the same time and it was Ke who helped me to start. Ke is an experienced TEM user and he drilled most of the TEM pores for this thesis. Ke is also experienced in fabrication and he also helped me a lot in making devices. I was very fortunate and happy to collaborate with Ke and we have been worked effectively to get things done. Ke also organised many events outside of the lab and we had nice parties and food at his place. Michael Graf, our first Swiss in the lab, it is so great to have you in the lab for too many reasons that I could not list them all here. I enjoyed all the time we spent together. Michael is a great friend in many aspects and one epitome is drinking beers. Michael, although your current fabrication job might be a tough thing, I know you will succeed because you are the guy who can always get complex things done. I would also like to thank Michael for the nice programing work and for reading my thesis. Martina Lihter, the fresh PhD student who is always asking "can you explain; can you tell me why, ...". Thank you for asking these questions. Without Martina, the lab and office life would be less dynamical as it is now. Martina, your patience in research, as well as your thirst for knowledge is a great asset. Prof. Po-ling Chang, thanks for the beer time: no beer no data! I would also like to thank Po-ling for the Chinese food he cooked for us and it was great. Dr. Hendrik Deschout, thank you for the discussion in all topics we had. Thanks to Sebastian Davis particularly for reading my thesis and improving the English here. Seb, thank you also for all the time we spent together. I would also like to thank all other members of LBEN and LBEN alumni.

This thesis involved a lot of collaborators and first I would like to acknowledge Prof. Andras Kis. The ground of my PhD lies on the high quality and extraordinary material platform: single-layer MoS₂, which is provided by one of the best 2D material labs in the world-LANES, led by Andras. In particular, I would like to thank Dr. Dumitru Dumcenco for the CVD growth of MoS₂ samples and thank Dmitry Ovchinnikov for measurements with the transistor. I was also very lucky to work with theoretician Prof. Massimiliano Di Ventra of UCSD. It was great to discuss with Prof. Di Ventra as he can always point out the heart of the question and Prof. Di Ventra proposed the additional evidence (current-molarity relation) for the observation of ionic Coulomb blockade. I would also like to thank Prof. Narayana Aluru and his team (Mohammad Heiranian, Vishal Nandigana) at UIUC for the beautiful simulation work on nanofluidics. The scientists and technicians of Center of microtechnology (CMI) and Interdisciplinary Centre for Electron Microscopy (CIME) are also acknowledged for providing the world-class facilities and technologies.

All the peers in nanopore field, thanks for all your work. For the the anonymous reviewers, I am grateful to all of you in case you are not delaying.

The jury members of my thesis: Prof. Minh Quang Tran, Prof. Philippe Renaud, Prof. Michael Mayer, and Prof. Meni Wanunu. Thanks for being on the jury and thanks for the comments, and the discussions.

Thanks to the giants I have been admiring. It is their work which enables us standing on their shoulders.

Finally, I would like to thank my family and friends outside of science. In particular, I would like to thank the support from my parents and my girlfriend Shuling Shen.

Jiandong Feng

Lausanne, May 2016

Contents	
Abstract	i
Acknowledgment	v
Contents	ix
List of Publications	xii
List of Figures	xiii
List of Tables	xvii
Chapter 1. Introduction: nanopores, where physics meets biology.....	1
1.1. Introduction.....	1
1.2. Nanopore: a tiny hole in a membrane	4
1.3. Sequencing DNA with nanopores.....	8
1.4. Challenges and opportunities for solid-state sequencing.....	12
1.5. Nanopores: beyond sensing	15
1.6. Outline.....	17
Chapter 2. Fabrication: engineering individual MoS₂ nanopores.....	21
2.1. Introduction.....	21
2.2. Single layer MoS ₂	22
2.3. Microfabrication of the membrane	23
2.4. Drilling and imaging single MoS ₂ nanopores with TEM.....	29
2.5. Voltage-induced electrochemical reaction in MoS ₂ nanopores	31
2.6. MoS ₂ nanopore formation and characterization	34
Chapter 3. Nucleotide structures probed by MoS₂ nanopores.....	45
3.1. Introduction.....	45

3.2.	Transport dynamics of biomolecules in nanopores	47
3.3.	Control of DNA translocation dynamics in nanopore	50
3.4.	DNA translocation through MoS ₂ nanopores	53
3.5.	Room-temperature ionic liquids as DNA solvent.....	58
3.6.	Slowing down DNA translocation with viscosity gradient.....	59
3.7.	Identification of single nucleotides.....	67
3.8.	DNA sequencing with MoS ₂ nanopores	77
Chapter 4. Mesoscopic physics: ionic Coulomb blockade in nanopores.....		81
4.1.	Introduction.....	81
4.2.	Conventional ion transport through nanopores.....	82
4.3.	Coulomb blockade theory and observation in quantum dots.....	83
4.4.	Observation of ionic Coulomb blockade	87
4.5.	Mesoscopic understandings to biological ion channels	100
Chapter 5. Nanofluidics: ultimate osmotic power generation with 2D membranes		103
5.1.	Introduction	103
5.2.	Electric conductance and surface charge of MoS ₂ nanopores	105
5.3.	Osmotic power conversion measured in MoS ₂ nanopores.....	108
5.4.	Computational nanofluidics model	116
5.5.	Demonstration of a self-powered nanosystem.....	129
5.6.	Single layer MoS ₂ membranes for nanofluidics	132
Chapter 6. Conclusion: a single molecule platform to fundamentals and applications		133
.....		
6.1.	Conclusion	133

6.2. Future directions in solid-state nanopore sequencing.....	133
6.3. Nanopores: artificial ion channels	135
6.4. Understanding the membrane-based process from a single nanopore.....	136
Chapter 7. Nanopores-Bridging engineering and understanding.....	137
Bibliography.....	139
Curriculum Vitae.....	159

List of publications

During the three-year PhD, I wrote the following papers on nanopores. Key results and conclusions of chapter 2 are shown in the 2014 ACS Nano paper (MoS₂ pore fabrication) and the 2015 Nano Letter paper (ECR pore formation). Part of chapter 3 has been published on Nature Nanotechnology in 2015, which reported the identification of single nucleotides by using ionic liquids. Chapter 4 is adapted from the ionic Coulomb blockade paper published on Nature Materials in 2016. The nanofluidic work in Chapter 5 will be published on Nature in 2016.

Liu, K., **Feng, J.**, Kis, A., & Radenovic, A. (2014). Atomically thin molybdenum disulfide nanopores with high sensitivity for DNA translocation. *ACS Nano*, 8(3), 2504-2511.

Feng, J., Liu, K., Graf, M., Lihter, M., Bulushev, R. D., Dumcenco, D., Alexander, D.T.L., Krasnozhon, D., Vuletic, T., Kis, A., & Radenovic, A. (2015). Electrochemical reaction in single-layer MoS₂: nanopores opened atom by atom. *Nano Letters*, 15(5), 3431-3438.

Feng, J., Liu, K., Bulushev, R. D., Khlybov, S., Dumcenco, D., Kis, A., & Radenovic, A. (2015). Identification of single nucleotides in MoS₂ nanopores. *Nature Nanotechnology*, 10(12), 1070-1076.

Feng, J., Liu, K., Graf, M., Dumcenco, D., Kis, A., Di Ventra, M., & Radenovic, A. (2016). Observation of ionic Coulomb blockade in nanopores. *Nature Materials*. DOI: 10.1038/nmat4607.

Feng, J., Graf, M., Liu, K., Dumcenco, D., Ovchinnikov, D., Heiranian, M., Nandigana, V., Aluru, NR., Kis, A., & Radenovic, A. Single-layer MoS₂ nanopores as osmotic nanopower generators. *Nature*, accepted. (2016)

List of Figures

Figure 1.1. The scale of the universe mapped to the branches of science and the hierarchy of science	2
Figure 1.2. The structure of DNA and its building blocks.....	3
Figure 1.3. Molecular representation of the atomic model of the KcsA K^+ channel	5
Figure 1.4. Alpha-hemolysin.....	6
Figure 1.5. Solid state nanopores	8
Figure 1.6. Concept of nanopore sequencing	10
Figure 1.7. MspA nanopore sequencing with DNA polymerase	11
Figure 1.8. Physical approaches for solid-state sequencing.....	14
Figure 2.1. Transition metal dichalcogenide.....	23
Figure 2.2. Process flow for the fabrication of MoS_2 nanopores.....	24
Figure 2.3. CVD growth of monolayer MoS_2	25
Figure 2.4. PMMA-etching based MoS_2 transfer method.....	26
Figure 2.5. Transferred CVD-grown MoS_2 monolayer covering the FIB hole.....	27
Figure 2.6. Verification of the thickness of MoS_2 membrane.....	28
Figure 2.7. EDX mapping of Mo and S elements in the monolayer MoS_2	29
Figure 2.8. TEM images of nanopores with various sizes drilled by a focused electron beam.	30
Figure 2.9. Schematic illustration of preparation of a freestanding MoS_2 membrane ready for electrochemical formation of a nanopore.....	32
Figure 2.10. Voltage-induced ECR.....	33
Figure 2.11. Calibration of conductance-pore size equation	35
Figure 2.12. Current-voltage characteristic of nanopores	36
Figure 2.13. Proposed mechanism of ECR based MoS_2 nanopore fabrication.....	37
Figure 2.14. Ionic current-steplike features during the nanopore formation	39
Figure 2.15. Power density spectrum noise analysis of an ECR fabricated MoS_2 nanopore	41

Figure 2.16. pNEB plasmid DNA translocation through an ECR nanopore.....	42
Figure 2.17. Verification of single pore formation by DNA translocation	43
Figure 3.1. DNA translocation velocity	46
Figure 3.2. Scaling exponents and entropic barrier for biomolecules through nanopore.....	49
Figure 3.3. Passive and active control of translocation dynamics.	51
Figure 3.4. Enzyme based approach to control translocation dynamics	52
Figure 3.5. Schematics of DNA translocation through MoS ₂ nanopores.....	53
Figure 3.6. DNA translocation through MoS ₂ nanopores..	54
Figure 3.7. Concatenated events of pNEB translocation in 5 nm and 20 nm MoS ₂ nanopores.	56
Figure 3.8. Lambda DNA translocation through a 20 nm MoS ₂ nanopore.....	57
Figure 3.9. Ionic liquids properties and interactions with DNA.	59
Figure 3.10. Schematic and characterization of the RTILs/ KCl viscosity gradient system in MoS ₂ nanopores.	60
Figure 3.11. Current-voltage characteristics of MoS ₂ nanopores and COMSOL simulations of the ionic transport through a MoS ₂ nanopore.....	62
Figure 3.12. Slowing down DNA translocation.	64
Figure 3.13. pNEB translocation traces through a MoS ₂ pore under ionic liquid/KCl condition	65
Figure 3.14. Single molecule DNA translocation through a nanopore probes the dynamics of Kramer's theory.....	66
Figure 3.15. Differentiation of 30mer oligonucleotides in the MoS ₂ nanopore.....	68
Figure 3.16. Scatter plots of 30mer oligonucleotides translocation,	69
Figure 3.17. Differentiation of single DNA nucleotides in the 2.8 nm MoS ₂ nanopore.....	71
Figure 3.18. Identification of single nucleotides in a MoS ₂ nanopore.....	72
Figure 3.19. Identification of single nucleotides in a 3.3 nm MoS ₂ nanopore.....	74
Figure 3.20. Recorded current blockade under different voltages.	75
Figure 3.21. Pore size dependent differentiation/identification of four nucleotides based on ionic current drops.....	76
Figure 3.22. Improved signal to noise ratio (> 100).....	77

Figure 3.23. Sequence-specific current trace of 30mer DNA	78
Figure 4.1. Ohmic behavior with linear I - V characteristics.	83
Figure 4.2. Proposed energy-level diagram of the single quantum dot.....	85
Figure 4.3. The energy diagrams of a quantum dot with multiple levels and the Coulomb oscillations.....	87
Figure 4.4. Schematics of single ion transport through a sub-nm MoS ₂ nanopore.....	89
Figure 4.5. Current–voltage characteristics (I - V) of a 0.6 nm MoS ₂ nanopore.....	90
Figure 4.6. Valence-dependent ion transport.	92
Figure 4.7. Current-molarity relation	94
Figure 4.8. The barrier heights for Coulomb blockade and dehydration	95
Figure 4.9. pH gated ionic transport.....	97
Figure 4.10. Current-voltage I - V measurements of an estimated 0.3 nm MoS ₂ pore ..	98
Figure 5.1. Reverse Electro Dialysis (RED)	104
Figure 5.2. Electrical conductance and chemical reactivity of the MoS ₂ nanopore...	105
Figure 5.3. Conductance as a function of pH.....	106
Figure 5.4. Simulated conductance of a 6 nm nanopore as a function of pore surface charge	107
Figure 5.5. Operation schematic of osmotic energy harvesting.....	109
Figure 5.6. MD simulated concentrations as a function of the radial distance from the center of the pore.....	110
Figure 5.7. Osmotic power generation.....	112
Figure 5.8. Electrode potential contribution.....	113
Figure 5.9. Power generation under different pH conditions.....	114
Figure 5.10. Power generation for two pores (4 nm and 15 nm)	115
Figure 5.11. Schematic of a typical simulation box in MD	118
Figure 5.12. Short circuit current as a function of the concentration ratio.	122
Figure 5.13. MD simulation of short-circuit current vs concentration gradient	124
Figure 5.14. Conductance of the nanopore as a function of the reciprocal thickness of the membrane.	125

Figure 5.15. Potassium and chloride concentrations as a function of the radial distance from the center of the pore for single and multi-layer membranes.....	126
Figure 5.16. The open circuit electric field across the membrane for different number of MoS ₂ layers	127
Figure 5.17. Variation of short-circuit current as a function of diameter.	128
Figure 5.18. Demonstration of a self-powered nanosystem.....	130
Figure 5.19. Characterization of a single-layer MoS ₂ transistor with nanopores and SMU131	

List of tables

Table 5-1. Data extracted from measurements by subtracting the electrode contribution	113
Table 5-2. Ion selectivity at different salt gradient conditions.....	115
Table 5-3. Membrane thickness vs power generation.....	116
Table 5-4. The Lennard-Jones parameters and charges.	118
Table 5-5. The individual contribution of ions to the current and the potassium selectivity coefficient of the pore.	122
Table 5-6. The residence time of potassium ions inside the λ layer at 1 V.	127

Chapter 1. Introduction: nanopores, where physics meets biology

1.1. Introduction

Science is the collective human efforts to understand and predict the universe: all of time, space and its contents, including planets, stars, galaxies, the contents of intergalactic space, the smallest subatomic particles, and all matter and energy[1, 2]. This scaling of the universe is mapped to the different branches of science, such as physical science and life science, as shown in **Figure 1.1**. Scientists have been developing tools to help characterize and then understand the universe, from the Hubble space telescope, which images the deep universe, to transmission electron microscopes which can now look at individual atoms. In the wide scale of the universe, the fundamental biological process which concerns one of the basic questions that humans ask ourselves constantly: how do we function, lies in the range of 10^{-10} to 10^{-6} m. To watch or manipulate things in such a range requires physical probes that could translate the information into a signal that can be read and understood. This is the range where physics meets biology.

Most of the new discoveries in biology rely on novel physical probes, which allow us to see reality from an unprecedented dimension. An epitome is the discovery of the double helical structure of deoxyribonucleic acid (DNA), which relies on the advance in X-ray crystallography[3]. Physical tools enable both new discoveries and verification of existing understandings. Among the physical tools people have developed more recently, single molecule platforms attracted considerable interest since they can provide direct information of an independent event without averaging a large number of processes[4, 5]. For example, optical approaches like super-resolution microscopy could illuminate the cellular or even sub-cellular scale beyond the diffraction limit[6-8]; electric methods, like the patch clamp technique[9], are able to monitor individual ion channels in cells. From a more general point of view, such a connection with physical tools applies not only to biology but also to all natural sciences.

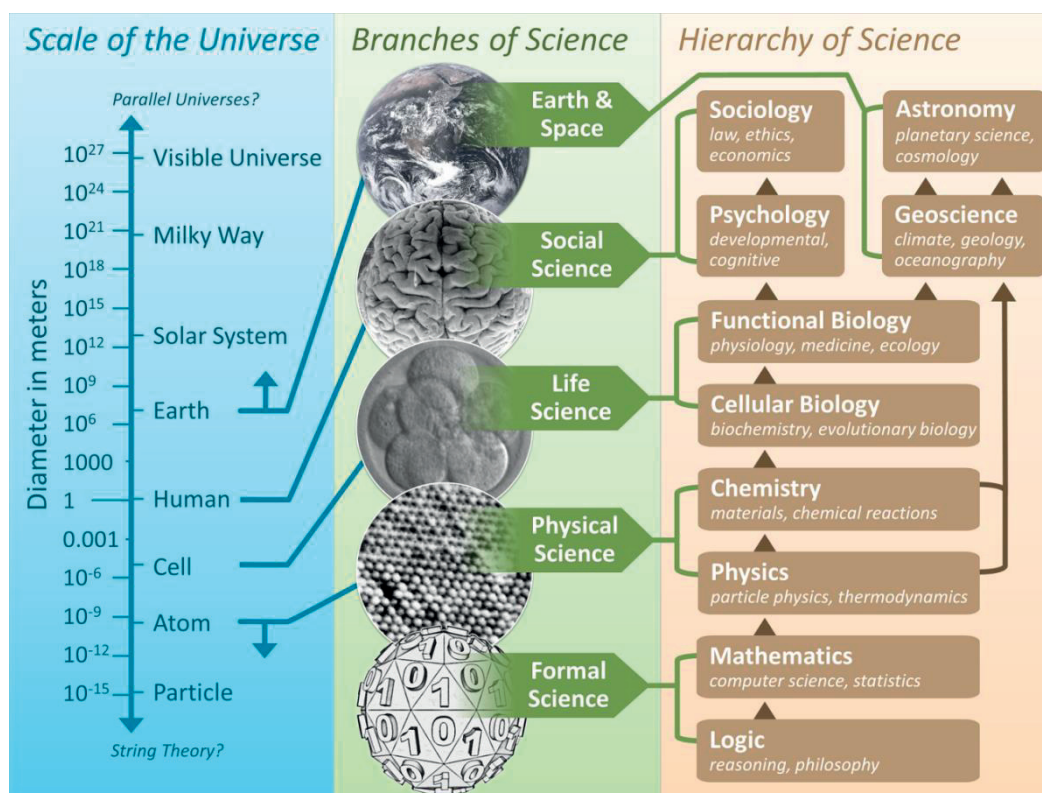


Figure 1.1. The scale of the universe mapped to the branches of science and the hierarchy of science[1]. Figure credit: Eric Fisk.

The playground of biology lies in the sequence of DNA, which contains the genetic information and thus a central problem in biology is to develop physical tools for DNA sequencing. DNA is the programming language of life which contains the genetically encoded information to synthesize proteins that perform most biological activities. From a physical point of view, it is a charged molecule built from four monomers. These building blocks of DNA are called nucleotides, including adenine (A), thymine (T), guanine (G) and cytosine (C). The DNA molecule itself is a chain of covalently bonded nucleotides with deoxyribose sugars and phosphate groups. Due to the hydrogen bond formation between A and T or G and C, two single strand DNA molecules could hybridize into a double strand DNA in a complementary way, forming the double helix structure which is so recognizable[10]. The DNA molecule has a diameter of about 1.1 nm for single strand and 2.2 nm for double stranded DNA. The spacing between two neighboring bases is about 0.3 nm[11]. **Figure 1.2.** illustrates its structure in detail. This dimension sets the spatial resolution required by the physical tools intended to probe it. First generation DNA sequencing was based on

the work of Fred Sanger, known as DNA sequencing with chain-terminating inhibitors and electrophoresis. Using Sanger sequencing, the human genome project was first started in 1990 and finally completed in 2003, costing a total budget of 3 billion dollars. Current second generation DNA sequencing is featured with commercialized massively parallel approaches like Illumina sequencing. The ideal sequencing would be pure physical and single molecule technology, thus eliminating biochemical and biochemical steps.

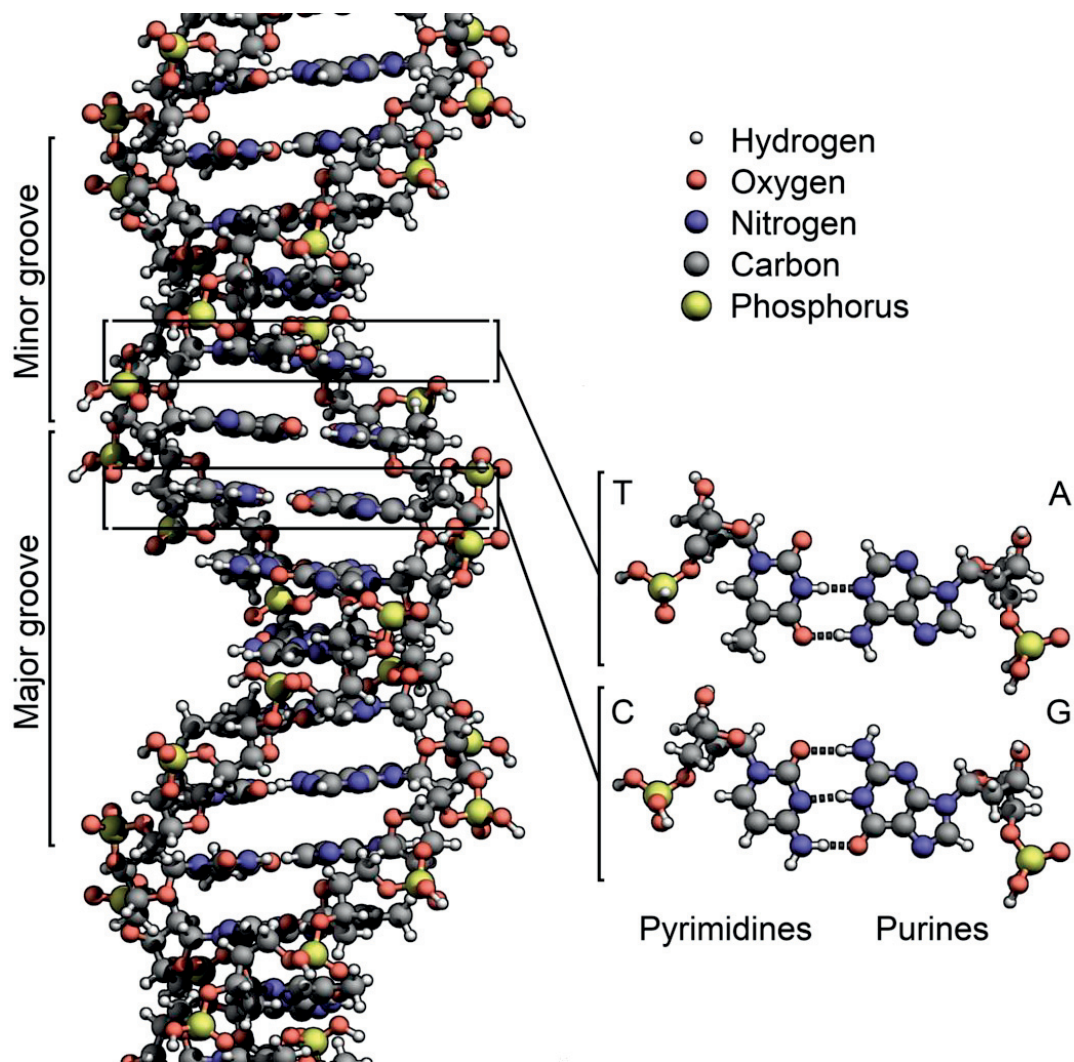


Figure 1.2. The structure of DNA and its building blocks nucleobases-cytosine (C), guanine (G), adenine (A), or thymine (T), deoxyribose and a phosphate group. Base pairing occurs due to the hydrogen bond formation between A and T or C and G. The double helix has a diameter of about 2.2 nm. Figure credit: Richard Wheeler.

Chapter 1. Introduction: nanopores, where physics meets biology

This thesis pursues applying physical tools for observing basic phenomena in physics and biology, in order to understand the physics behind them. The physical tool used in this thesis is a nanopore platform, which enables probing chemical structures of DNA molecules and physical processes of ion transport at the nanoscale.

1.2. Nanopore: a tiny hole in a membrane

What is a nanopore? A nanopore is a nanometer sized hole in a membrane[12]. More specifically, nanopores can be classified as biological pores[13] and solid-state pores[14]. Biological pores are formed from specific transmembrane proteins that spontaneously insert themselves into a lipid membrane. One of their natural forms is known as membrane ion channels, which transport matter and information between the environment and cells[15]. Ion-channel electrophysiology employs these individual ion channels as probes to investigate cell communications[16]. Ion channels have very small pore diameters (most channels are subnanometer size) and they are extremely sensitive and selective[17]. For example, the L-type calcium channel is only 0.7 nm in diameter[18] and potassium channels which selectively transport potassium ions, can be activated by voltage[19] or calcium[20], depending on its protein structure (**Figure 1.3**). Ion channels are also basic tools for biotechnology. Gene-expressed, light-sensitive ion channels can be employed to use light to control cells in living tissue, typically neurons. This neuromodulation method is better known as Optogenetics[21, 22].

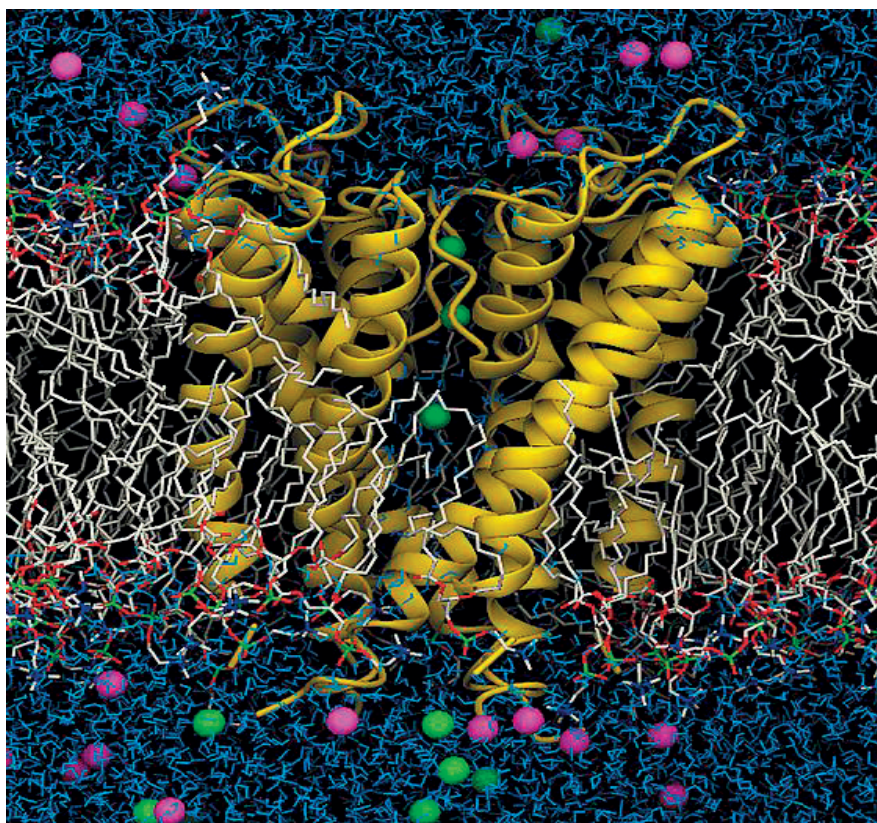


Figure 1.3. Molecular representation of the atomic model of the KcsA K^+ channel embedded in an explicit DPPC phospholipid membrane bathed by a 150 mM KCl aqueous salt solution[23]. K^+ : Green, Cl^- , Pink. Figure reproduced from Nature Publication[24] with permission.

Membrane channels slightly larger in size can also serve as transporters for other solutes. Protein nanopores can be constructed using a class of molecules, termed porins[25]. For example, as shown in **Figure 1.4**, a transmembrane pore can be formed by the bacterial toxin, alpha-hemolysin which is remarkably stable and widely tested in many laboratories as a sensor[26]. Recently, another geometrically well-defined protein pore using *Mycobacterium smegmatis* porin A (MspA) was also reported, with a narrow constriction of 1.5 nm, slightly larger than the size of single-stranded DNA[27]. Natural protein nanopores can also be engineered to meet biosensing requirements, using bioengineering methods like protein engineering or genome editing[28-30].

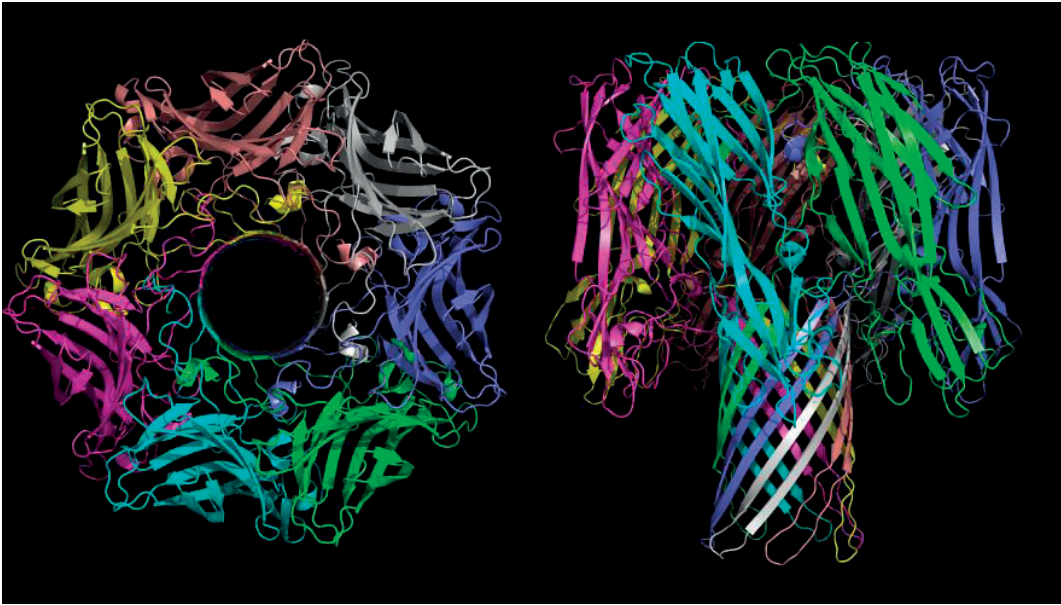


Figure 1.4. Alpha-hemolysin, *Staphylococcus aureus* alpha toxin from *S.aureus*. Figure reproduced from Science[26] with permission.

Another family of nanopores is the so-called the solid-state nanopore, artificial holes fabricated by engineering tools in membranes made from hard solid materials[14]. Engineering solid-state nanopores has been a long-term goal of nanotechnology. Engineering tools, such as microfabrication, electron microscopy and scanning probe microscopy, on solid-state materials have allowed us to build materials atom by atom, to the precision that nature does. In addition, engineering approaches allow scaling of the device by which we could design and create the nanopore in almost any size we want. This is something that protein nanopores cannot realize although tiny changes in size can be made via bioengineering techniques, while engineering approaches could easily make pores from a single nanometer to hundreds of nanometers in a thin membrane (typically 20 nm thick silicon nitride)[14]. For example, ion beam sculpting allows rearrangement of the surface of materials via both sputtering and depositing[31]. The atomic-scale erosion process of sputtering removes atoms from the hard materials, causing a pore to open. The ion beam can also stimulate the lateral transport of matter into current features which shrinks the pore. This process allows fabrication of individual solid-state nanopores down to a diameter of 1.8 nm in thin silicon nitride membranes[31, 32]. Another way of fabricating nanopores with nanometer precision is based on the use of focused electron beams in a transmission

electron microscope (TEM) via electron irradiation[33]. Nanopores are formed due to sputtering, localized heating fluidizes matter and surface tension when in contact with an electron beam. The TEM based technique also allows imaging of the pore at high resolution immediately after the drilling process, providing direct structural information of the fabrication. Both approaches above rely heavily on high-end instrumentation and this thesis invented a new scalable and cost-effective method to produce solid-state nanopores at atomic resolution (**Chapter 2**). Up to now, solid-state nanopores have been made on many different materials, even in a two-dimensional crystal, like graphene - a single atomic layer of graphite[34]. Graphene nanopores have a thickness of only 0.3 nm, thinner than any protein nanopore[35-37]. If we could engineer solid-state nanopores in two dimensional (2D) materials in subnanometer range atom by atom, it would be a new dimension nature never achieved. In addition to controlled engineering in dimension and materials used according to needs, compared to protein nanopores, solid-state nanopores have also the advantage of stability in various environmental conditions and its integrability to electronics[38-40]. However, fabricating solid-state nanopores with a resolution comparable to proteins is still a challenge, particularly in the subnanometer range. Pore surface chemistry and charge vary from pore to pore, limited by the top-down engineering approaches used. Such bottlenecks in fabrication are also opportunities for physicists and engineers. This thesis classifies current solid-state nanopores into two generations, as shown in **Figure 1.5**. The first generation of solid-state nanopores: pores are made in microfabricated thin membranes (typically 20 to 30 nm in thickness) by TEM irradiation or ion beam sculpting, with typically diameters larger than 3 nm. The second generation of solid-state nanopores: nanopores are made in 2D materials, which is featured with atom by atom fabrication. However, the current two generations are both made using top-down approaches. I suspect that the next generation of solid-state nanopores would benefit from a programmed bottom-up approach, eliminating the problems of surface charge and chemistry distribution. DNA origami is a good starting point in this direction[41].

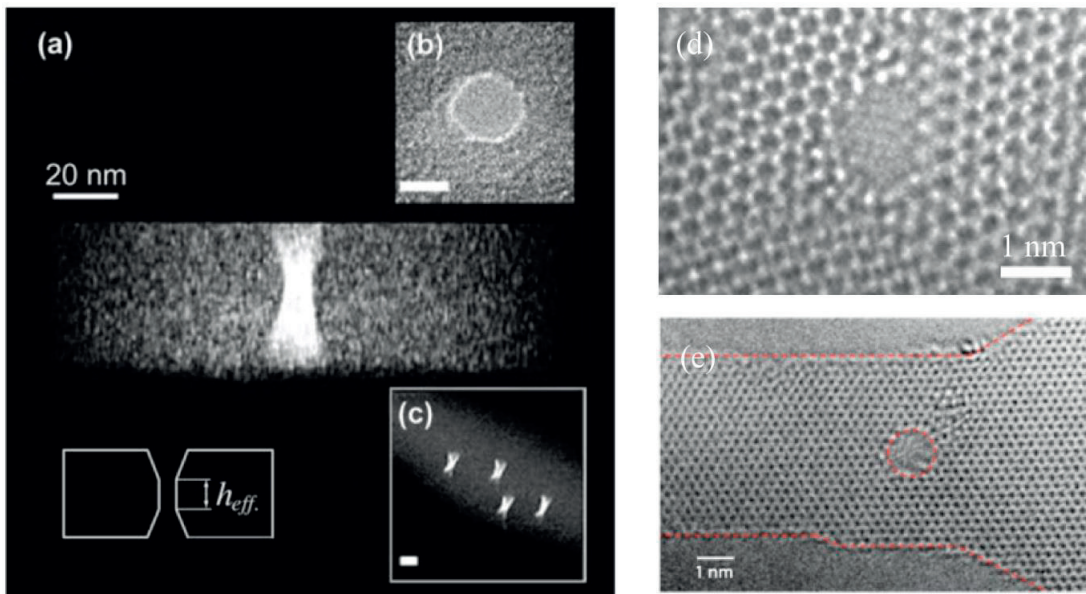


Figure 1.5. Solid-state nanopores. **(a)**, **(b)** and **(c)**. first generation of solid-state nanopores made in silicon nitride membranes, with a 20 nm diameter and large effective thickness. **(a)** sideview from tomography, **(b)** top view, and **(c)** side view of a nanopore array. Figure reproduced from [42] with permission **(d)** and **(e)** present examples of second generation solid-state nanopores. TEM image of a 1 nm pore made in 0.7 nm MoS₂ membrane **(d)** and a 1-nm graphene pore in a patterned graphene nanoribbon FET device **(e)**. Figure credit: Henny Zandbergen (from <http://ceesdekkerlab.tudelft.nl/>).

Nanopores as physical probes have the desirable dimension that fundamental biology asks, from atoms like charged ions to long biomolecules like DNA. We could already watch electrophysiology and control lives via light with ion channels in Optogenetics. What else can the nanopore tool bring to us?

1.3. Sequencing DNA with nanopores

The first thing a nanopore probe can do is single molecule detection – a sensor that detects a nanoscale object which can be DNA, RNA, protein or their complex structure/modifications and any other organic or inorganic molecules/particles in aqueous or non-aqueous solution [12, 43]. The idea is simple and it originates from the Coulter counter or something even earlier, known as resistive-pulse technology [44].

This label-free sensing method is very elegant and straightforward and it utilizes the change of conductance of ions through the single pore due to the presence of a particle, which is slightly smaller than the size of the pore. Coulter patented this method for counting red blood cells in the 1950s[44]. The resolution of this technique lies in the size of the probe: the nanopore we design and it can be applied to any object on the scale where this classical physical law still applies.

Let us now consider if we have a tiny membrane channel with 1.6 nm in diameter embedded in an impermeable lipid bilayer membrane, separating two chambers containing aqueous electrolytes. A current carried by the ions can be measured with standard electrophysiological techniques when a transmembrane voltage is applied. The current could be blocked when something gets into the pore. Around 1990, David Deamer and George Church, independently came up with the idea: if a chain of nucleotides-the DNA molecule, can be electrophoretically driven through a nanopore, the bases would similarly modulate the ionic current through the nanopore. The sequence of DNA could then be recognized based on the changes in the ionic current due to individual nucleotides[25], as shown in their patent (**Figure 1.6**). Subsequently, this nanopore sequencing concept was first experimentally tested in the 1996 landmark paper via translocating single-stranded DNA through an alpha-hemolysin pore[45], which showed the potential to distinguish short DNA homopolymers composed of different nucleotides.

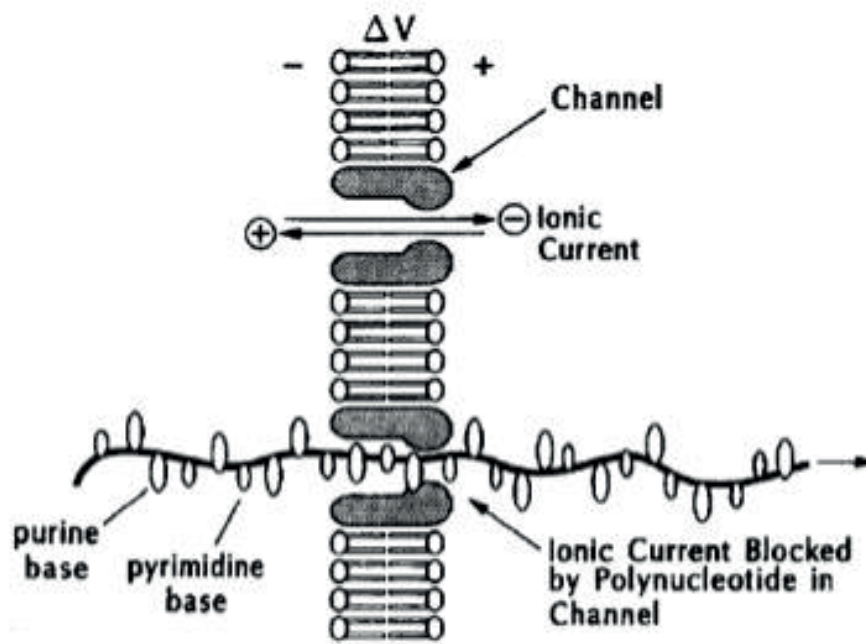


Figure 1.6. Concept of nanopore sequencing in US patent 5,795,782[46].

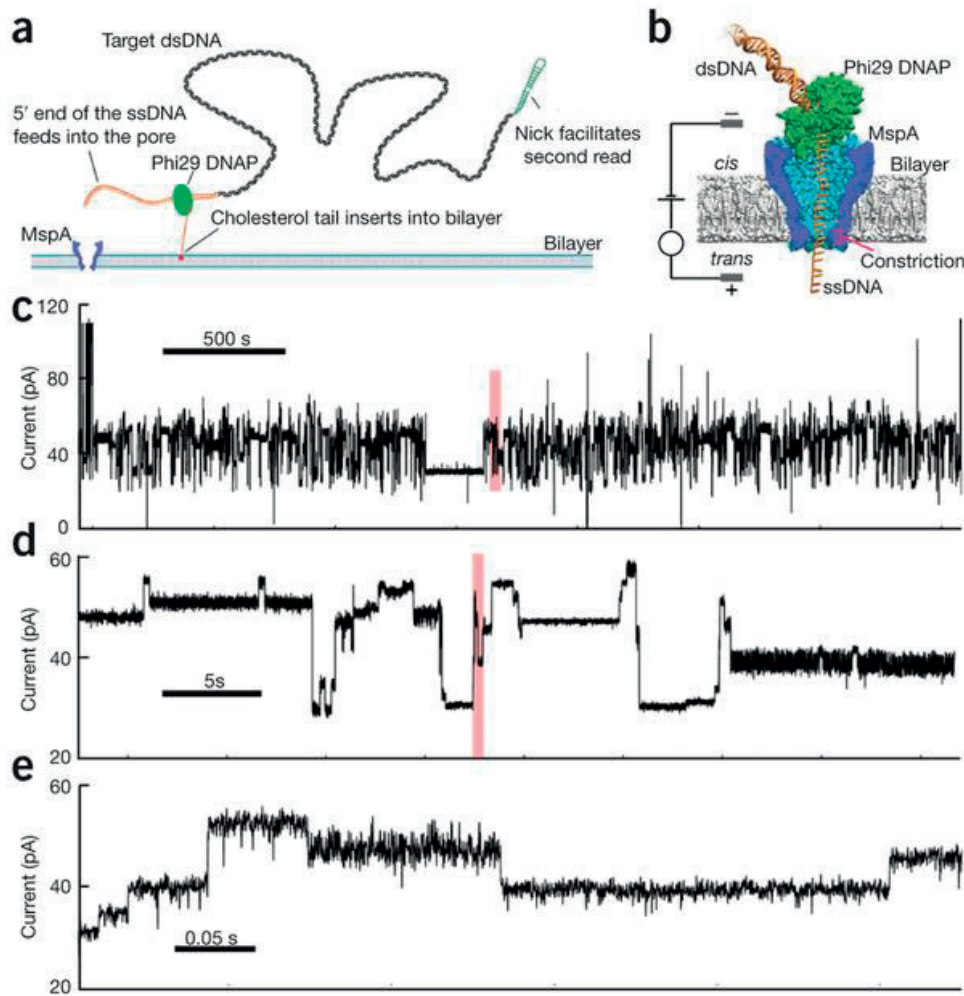


Figure 1.7. a, b. MspA nanopore sequencing with DNA polymerase Phi29. c, d, and e are the corresponding current trace showing distinguished levels for DNA sequencing. Figure reproduced from Nature Publication[47] with permission.

Later in 2004, NIH launched the \$1000 genome project and started to provide a significant amount of funding to support nanopore research. The delivery of practical nanopore sequencing was about 16 years later (2012), and now starts to be commercially available after almost 20 years[48]. Nanopore sequencing was demonstrated using a protein nanopore with a polymerase or helicase acting as a molecular motor to ratchet DNA in a controllable manner[49]. A combination of several nucleotides inside the pore would produce a corresponding level in current trace, depending on the physical geometry of the protein pore used. For instance, the *Mycobacterium smegmatis* porin A has an effective sensing length of 4-nucleotides (1.2 nm) and the sequencing is based on identifying all combination of 4 nucleotides,

Chapter 1. Introduction: nanopores, where physics meets biology

resulting in a total number of 256 levels[47], as shown in **Figure 1.7**. Testing or bioengineering protein pores with a shorter sensing length then is the next task to improve the sequencer performance.

The potential and scope of nanopore sequencing are enormous owing to its portability, remarkably low cost, single-molecule detection, label-free property, fast sequencing speed, and general applicability to other platforms of molecular diagnostics. Nanopore sequencing has the chance to revolutionize the whole of biotechnology and medical treatment, promoting the delivery of the era of personal medicine. In addition, nanopores are a general sensing platform which can extend to other target analytes. It should be noticed that as a label-free technology, nanopore cannot determine the identity of a molecule but the physical information such as dimension and charge. Probing the chemical structures using nanopores for unknown species would rely on the combination with other techniques. This case is similar to identifying the structure of organic molecules using a combination of ultraviolet-visible, infrared, nuclear magnetic resonance, and mass spectrum. It might be more accurate to say nanopore sequencing is at the end of resistive-pulse technology and once it is possible, nanopore sensing platforms should widen its application to all the rest of analytes from nucleobases to cells and their modifications[12].

1.4. Challenges and opportunities for solid-state sequencing

Given the success of sequencing using protein nanopores and the same basic sensing principle for solid-state nanopores and biological pores, what can solid-state nanopore bring to us?

The physics of ionic current flow through a small pore imposes a fundamental limit on resolution: the sensing length or so-called Deamer limit where how many nucleotides are modulating the current at a time due to dimension-dependent electric field distribution in the pore[25, 45]. The current analysis for MspA pore, is based on analysis of a combinations of 4 nucleotides (256 levels)[47]. The most sensitive nanopore sequencer should have a size just larger than single strand DNA (1.1 nm) and should also be as thin as possible to hold the minimum number of nucleotides at any one time. This requirement requires the thinnest membrane which graphene can

offer. With only 0.3 nm in thickness and a 1.2 nm diameter, graphene nanopores can in principle provide a sensing length shorter than 4 nucleotides. Considering the access resistance effect due to electric field distribution around the pore, the sensing length can at least be reduced to 2 nucleotides[50], which is also theoretically shown to be possible using molecular dynamics simulations[51-53]. This sensitivity would enable DNA sequencing with higher accuracy and even protein sequencing, in a more distant future. Nonetheless, the lack of temporal resolution complicates reads of sequences with graphene nanopores.

From an engineering point of view, in contrast to biological pores, solid-state nanopores can operate in various liquid media and pH conditions, their production is scalable and compatible with nanofabrication techniques, and they do not require the excessive use of biochemical reagents. The mass fabrication of complementary metal–oxide–semiconductor (CMOS) technology would push the production of solid-state nanopore devices to a scale that can realize individual sequencing, the playground for personal medicine. These advantages are expected to make solid-state nanopore sequencing cheaper than sequencing with biological pores[38-40].

However, solid-state nanopore sequencing has yet to be delivered due to various technical difficulties. In both biological and solid-state nanopores, achieving optimal translocation speed remains a significant challenge. In nanopore sequencers based on biological pores, enzyme-driven translocation speeds are on the order of 2.5 to 70 nt/sec and currently too slow, and limited by the use of enzyme[49]. Therefore, to achieve genome sequencing, thousands, even millions of biological pores need to be integrated to one sequencer. In solid-state nanopores, the average voltage-driven translocation speeds are on the order of 3000-50,000 nt/ms, with the large range due to factors such as differing pore sizes (1.5-25 nm) and applied potentials (100-800 mV)[54]. These speeds limit the ability of solid-state nanopores to reach single-nucleotide resolution and is one of the major obstacles to using solid-state nanopores to sequence DNA. The ideal speed should be as fast as possible as long as it satisfies those requirements of signal to noise ratio of the state of the art current amplifier. The final goal can only be realized based on advances in engineering.

As well as translocation speed, solid-state nanopores also face problems with low ionic current signal-to-noise ratios and relatively large sensing regions[14]. Reducing

the noise in solid-state devices is also challenging but owing to previous experience in noise reduction in semiconductor devices, various efforts have been made to realize extremely low noise, like using a thick passivation polymer coating[55] or glass substrate[56] which results in lower noise than protein pores. The size of the sensing region is due to the thickness of the pore membranes, which are typically 10-20 nm thick, a size that can accommodate 30-60 nucleotides at a time[14]. As mentioned before, graphene nanopores, with ultimate thickness should address this issue in principle[35-37]. However, except the lack of temporal resolution, pristine graphene nanopores exhibit strong hydrophobic interactions with DNA, which limits their long-term use due to clogging and means that surface functionalization of the graphene is required. To this end, seeking other alternative 2D materials as nanopore membranes has been another task for solid-state nanopore sequencing. Single-layer boron nitride has also been tested as nanopore membrane[57].

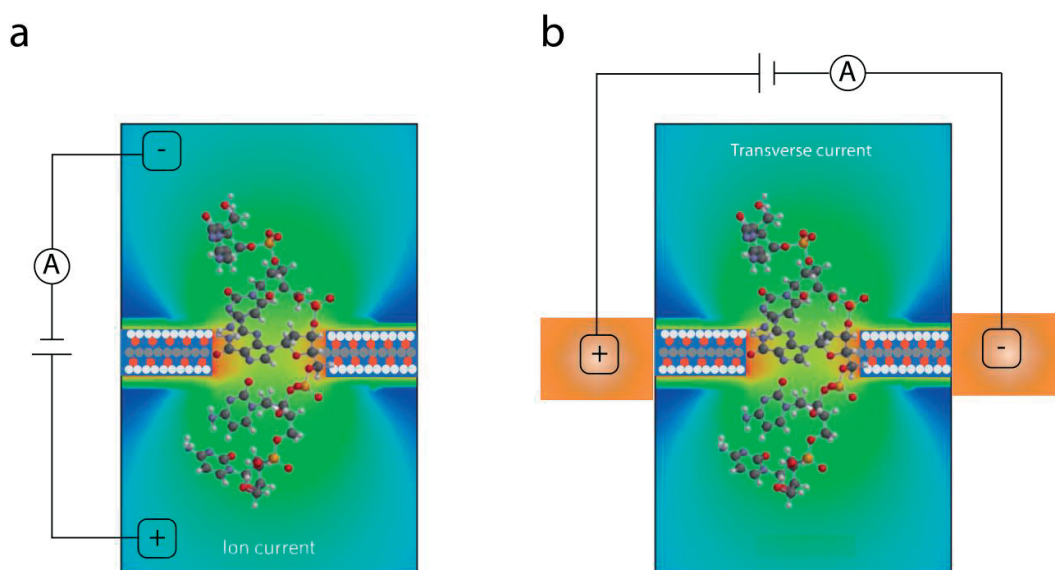


Figure 1.8. Physical approaches for solid-state sequencing. **(a).** Using ionic current **(b).** Using transverse current either tunnel or field effect. The color gradient indicates the electric field around a nanopore when the membrane is biased. Figure adapted from Nature Publication[40] with permission.

The solid-state nanopore has the integrability to platforms with other sensing mechanisms and typical examples are listed in **Figure 1.8**. These approaches can differ from the basic nanopore sensing, such as using electron tunneling current[58, 59] and a field effect transistor[60, 61]. The tunneling current flows transverse to the

long axis of the DNA molecule and conducts through a single nucleotide when it is passing the pore. This approach is first proposed by Massimiliano Di Ventra[58] and experimentally demonstrated by Kawai and colleagues[59, 62]. Another transverse approach is measuring the field effect of DNA on the drain source current of the transistor [60, 61, 63]. The difference in physics and device geometry may produce a sensitivity difference, in terms of the measured signal to noise ratio with state of the art low noise amplifiers under the comparable bandwidth. Most notably, unlike ionic approach which needs the isolation on ionic reservoirs, transverse devices can be readily parallelized on one chip. Thus the total number of integrated individual sensors on one chip can have much higher density than ionic sensing and therefore solid-state devices allows for faster reading.

Last, the scaling in solid-state nanopore, like varying the pore size, can allow not only DNA sequencing but many other kinds of sensing applications. The pore size can be designed based on the dimension-requirement of the target analyte or mixture of analytes and this scaling should apply to any object that is charged. In addition, applicability to un-charged particles is also possible since one could also integrate other driving forces, like using a pressure difference.

However, for solid-state nanopores, notwithstanding many fantastic works which have been performed since its invention, the resolution is still in long DNA molecule/protein level, for example the typically used lambda DNA, and there is no progress towards sequencing, in contrast to the success of the protein nanopore sequencer.

To summarize, solid-state nanopores can deliver the ultimate sequencer with optimized sequencing speed, scaled fabrication and integrability. These features still make solid-state nanopore attractive. If protein nanopores are the 4th generation in DNA sequencing, solid-state sequencing will be the 4.5th generation which is pure physical, ultimate sequencing speed (only limited by state of the art current amplifier), mass fabrication, and multiplexing, but before this, the above problems should be solved one by one.

1.5. Nanopores: beyond sensing

Nanopores have started from membrane channels, and now arrive at artificial pores but this is not the end. Nanopore-based sensing applications, including the key driver: DNA sequencing, have been a very productive topic and nanopore sequencing is believed to be one of the key outcomes of nanotechnology. Apart from sequencing, nanopore sensing has been applied to DNA, RNA, protein, complex of biomolecules, small molecules, non-natural polymers, metal ions, nanoparticles and their modifications. Numerous efforts have also been made in engineering protein nanopores and identifying materials as nanopore membranes, such as mutation of protein structure[30], carbon nanotubes[64] and 2D materials[65] or even DNA nanostructures[41, 66]. Various fabrication methods have also been proposed like ion beam sculpting[31], TEM based electron beaming irradiation[33] and recent voltage-induced dielectric breakdown[67]. Such efforts in engineering should enable further research beyond sensing.

Biological Physics: Starting from the membrane channels, nanopores are artificial ion channels. The feature "artificial" indicates its all advantages for probing physics of ion transport. People can engineer any structure they want according to their needs, and furthermore artificial nanopores, particularly solid-state nanopores can operate at extreme conditions that are not limited by the physiological environment and stability of ion channels[68]. From the point of view of dynamics, the time dependent signal contains lots of kinetic information, for example, probing the surface charge fluctuations[69] and gating effect. Ion transport is a very interesting field and it is important to the function of our bodies. The artificial ion channel, as a physical probe, may allow investigations that have not been possible with natural ion channels.

Nanopores can serve as single molecule force spectroscopy since applied force information could be directly obtained from the electric field, as shown in the pulling experiments of DNA-protein complex[70], DNA hairpin unzipping[71], DNA coil entropic elongation[72], protein folding[73] and nucleosomal DNA tail[74]. Nanopores can also be integrated with optical tweezers to allow the direct force measurement[75]. Recently, single-molecule picometer resolution nanopore tweezer[76] was realized as the MspA nanopore could detect the picometer movement of DNA molecule controlled by the helicase employing the same principle of enzyme enabled nanopore sequencing.

Chemistry: A nanopore membrane is a reactor. Nanopores can also be used as nanoreactors to study covalent chemistry at the single-molecule level, such as the formation and cleavage of arsenic-sulfur bonds in alpha-hemolysin pores[77]. Nevertheless, probing such reactions in protein nanopores still relies on resistive-pulse technology and the pore is also involved in reaction. An exception is the mixed reaction inside the pore, like synthesis of individual nanoparticles[78]. Nanopores can also be equipped with an enzyme, then one could study enzyme kinetics. Electrochemistry at the nanopore is also very interesting since one could adjust the bias across the membrane and monitor the reaction using the changes in the current baseline. Nanopores are a powerful tool to study single molecule chemistry since they can host and monitor chemical process at the same time.

Engineering: To eliminate averaging over many pores with various diameters, ion transport in nanoscale should be ultimately probed with an individual fluidic channel, which nanopores can offer. A single nanopore system is an ideal tool to study nanofluidic phenomena such as water desalination or osmotic power generation[79]. Controlled experiments with a single nanopore allow the identification of each key parameter individually and thus provide direct suggestions for the scaling-up of the process to an industrial level.

1.6. Outline

This introduction **Chapter 1** reviews the background, current status and potential power of nanopore research. In conclusion, nanopores are an elegant and powerful tool to probe science at tunable scale. This thesis focuses on nanopores for probing chemical structures, in particular single DNA nucleotides and physical processes of ion transport: ionic Coulomb blockade and osmotic power conversion.

Chapter 2 presents the technical background of all investigations: the fabrication of the nanopore device and the measurement platform. This thesis chases the ultimate nanopore device: controlled small diameter, and atomic thickness. Both requirements are fulfilled with nanopores made in a single layer molybdenum disulfide which offers a 2D platform (0.7 nm in thickness) for nanopore engineering. This chapter describes the microfabrication of the nanopore membrane, TEM based MoS₂ drilling

Chapter 1. Introduction: nanopores, where physics meets biology

and a novel scalable nanopore fabrication approach based voltage-induced electrochemical reaction. The electrochemical reaction on the surface of single-layer MoS₂ is initiated at the location of defects or single atom vacancy, followed by the successive removals of individual atoms or unit cells from single-layer MoS₂ lattice and finally formation of a nanopore. The atomic resolution and accessibility of the fabrication approach and the use of 2D materials such as single layer MoS₂ have set the technical stage of the following investigations.

Chapter 3 shows the probing of the chemical structures of DNA molecules- single nucleotides, with MoS₂ nanopores which is the ultimate sensing application of solid-state nanopores. Nanopores in 2D materials have demonstrated their capability of unprecedented spatial resolution towards DNA sequencing. DNA translocations in MoS₂ nanopores are demonstrated, showing high sensitivities. In addition, compared to graphene, DNA does not stick to MoS₂ nanopores owing to the enriched hydrophilic sides near the pore and thus MoS₂ nanopores shows extremely good stability (up to days) for translocation experiments. However, the high translocation velocity (3000-50000 nt/ms) of DNA molecules moving across such membranes limits their usability. We introduced a viscosity gradient system based on room-temperature ionic liquids (RTILs) to control the dynamics of DNA translocation through a nanopore fabricated in a single-layer MoS₂ membrane. This allows us for the first time to statistically identify all four types of nucleotides with solid-state nanopores according to their current blockage signatures in translocation experiments. This method paves the way for future low-cost and rapid DNA sequencing with solid-state nanopores.

Chapter 4 reveals probing mesoscopic physical law of ion transport in nanopores. Emergent behaviour from electron-transport properties is routinely observed in systems with dimensions approaching the nanoscale. However, analogous mesoscopic behaviour resulting from ionic transport has so far not been observed, most probably because of bottlenecks in the controlled fabrication of sub-nanometre nanopores for use in nanofluidics. This chapter reports measurement of ionic transport through a single sub-nanometre pore junction, and the observation of ionic Coulomb blockade: the ionic counterpart of the electronic Coulomb blockade observed for quantum dots. The findings demonstrate that nanoscopic, atomically thin pores allow for the

Chapter 1. Introduction: nanopores, where physics meets biology

exploration of phenomena in ionic transport, and suggest that nanopores may also further our understanding of transport through biological ion channels.

Chapter 5 presents probing nanofluidic phenomena: ultimate osmotic power generation through 2D membranes. A single pore with well-defined geometry is the best system to test our fundamental understanding of nanofluidic process' since all parameters can be addressed individually, in contrast to averaging many pores. Power generation from the osmotic pressure difference between fresh water and seawater is an attractive, renewable and clean energy harvesting method. For this task, 2D material membranes are expected to be the most efficient since water transport through a membrane scales inversely with the membrane thickness. This chapter demonstrates the use of single-layer MoS₂ nanopores as osmotic nanogenerators. A large, osmotically induced current is observed from salt gradient with estimated power density of up to 10^6 Wm^{-2} which can be attributed mainly to the atomically thin membrane of MoS₂. Our results suggest that MoS₂ membranes are promising candidates for osmotic power harvesting.

Finally, **chapter 6** and **chapter 7** will review all investigations made in this thesis based on a single nanopore probe and propose the future directions on what else nanopore tools can bring us and what else we can learn from nanopore experiments.

Chapter 2. Fabrication: engineering individual MoS₂ nanopores

2.1. Introduction

Fabrication of nanostructures with sub-nanometer, or even single-atom precision has been a long-term goal for nanotechnology. The rise of graphene[80] and recently other 2D materials, such as the single-layer molybdenum disulphide (MoS₂)[81], offers an ideal platform for such a purpose, due to their highly ordered lattice in two dimensions. Fabrication of solid-state nanopores that are used in single-molecule sensing would benefit tremendously from such a nanoscale fabrication method. Conceptually, nanopore sensing is based on a single, nanometer sized aperture located on a nanometer thin membrane; by monitoring the changes in the ionic current, it is possible to detect electrophoretically driven biomolecular translocations in a high throughput manner, while revealing localized information of the analyte[14, 25]. Solid-state nanopores exhibit relatively lower single molecule detection sensitivity compared to bio-pores due to their intrinsic thickness and lack of control over surface charge distribution[14]. During a typical translocation experiment in 30 nm thick SiN_x membranes, DNA regions approximately 30 nm long and containing ~100 base pairs (bps) are residing within a nanopore at any given time. Therefore, single base resolution is not expected here. Recently, thin membranes have been proposed to extend the applications of solid-state nanopore to, e. g., detection of short DNA oligomers and differentiation of short nucleotides homopolymers[82]. The merits of this novel approach are two-fold. First, the thin membrane can amplify both baseline and signal amplitude without increasing noise levels, resulting in a greatly enhanced signal to noise ratio (SNR)[83]. Furthermore, ultra-small nanopores (1 – 2 nm) can be further adapted to mimic biological nanopores, where a narrow constriction (1.2 nm for MspA and 1.5 nm for alpha-hemolysin)[27, 84] and small sensing length (0.5 nm) could facilitate single nucleotide identification along DNA strands. This concept can be exploited using the 2D material graphene, a single atomic layer of carbon which can extend over macroscopic scales in two dimensions (mm in size) while being atomically thin (few Å) in the perpendicular dimension[80].

Several groups already demonstrated the use of graphene as a nanopore membrane for detecting DNA translocation [35-37]. Using a modern transmission electron microscope (TEM), nanopores in graphene can be sculpted atom by atom with diameters that can be tailored for various applications[50, 85, 86]. Another advantage for graphene, as predicted by theoretical calculations [63, 87], is its potential use in a transistor integrated with a nanopore where DNA translocation can modulate the tunneling current or gate the transistor channel. We recently demonstrated the first realization of simultaneous detection of DNA translocation with two synchronized signals, the ionic current in the nanopore and local potential change in the graphene nanoribbon transistor[61]. Apart from all these encouraging achievements, it is worth noting that the strong π - π interaction between graphene and DNA[88] leads to undesirable adsorption of DNA on graphene, which may hinder the DNA translocation through graphene nanopores. Some groups have exploited surface modification[89], atomic layer deposition[36] and high pH and ionic strengths[35] to minimize surface interaction. The first two approaches ultimately increase the sensing length to few nanometers which is not desirable for single nucleotide resolution. An alternative solution is to use other 2D materials such as insulating boron nitride (BN)[57] as the membrane material. To this end, this section studies the use of utilizing MoS₂, a newly emerging transition metal dichalcogenide-based material, as a nanopore membrane.

2.2. Single-layer MoS₂

MoS₂ has drawn attention as a promising material with potential applications complementary to graphene due to the presence of a bandgap and versatile chemistry [90], which makes it attractive in various applications including catalysis, energy storage, sensing and electronic devices such as field-effect transistors[81] and logic circuits[91]. The thickness of single-layer MoS₂ is ~ 6.5 Å, comparable to the thickness of graphene (3.5 Å) while the spacing between two neighboring nucleotides along ssDNA (3.2 – 5.2 Å). Both exfoliation[92] and chemical vapor deposition (CVD)[93, 94] can be used to produce thin layers MoS₂ with good quality[92-94].

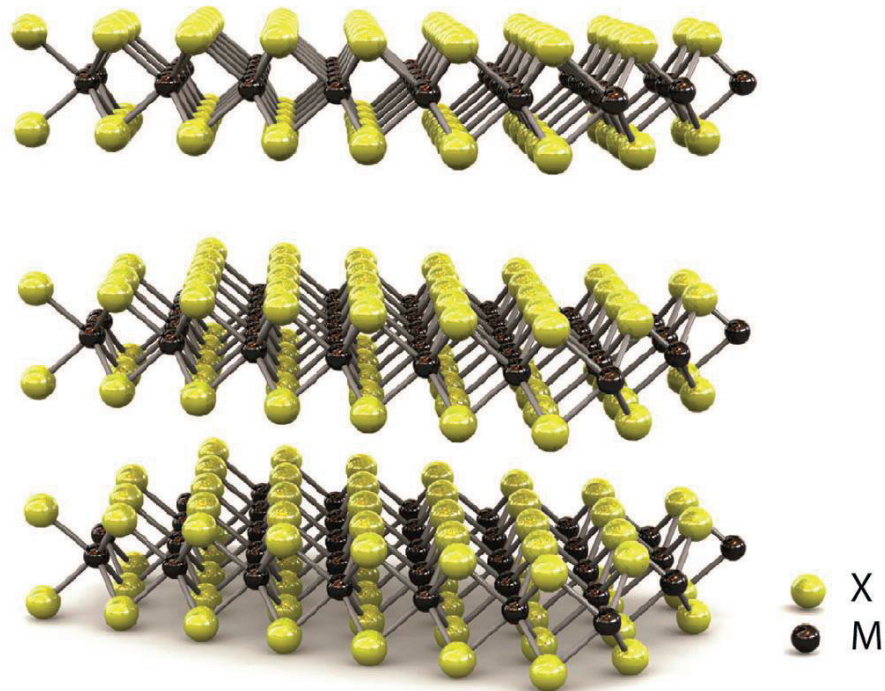


Figure 2.1. Three dimensional representation of transition metal dichalcogenide (MX₂). Figure credit: Andras Kis. Figure reproduced from Nature Publication[81] with permission.

2.3. Microfabrication of the membrane

Prior to nanopore fabrication, we first create freestanding MoS₂ membrane on a predesigned supporting opening. This process involves clean-room process that has been done at the EPFL Center for Micro/Nanotechnology (CMi). The process flow is given in **Figure 2.2**.

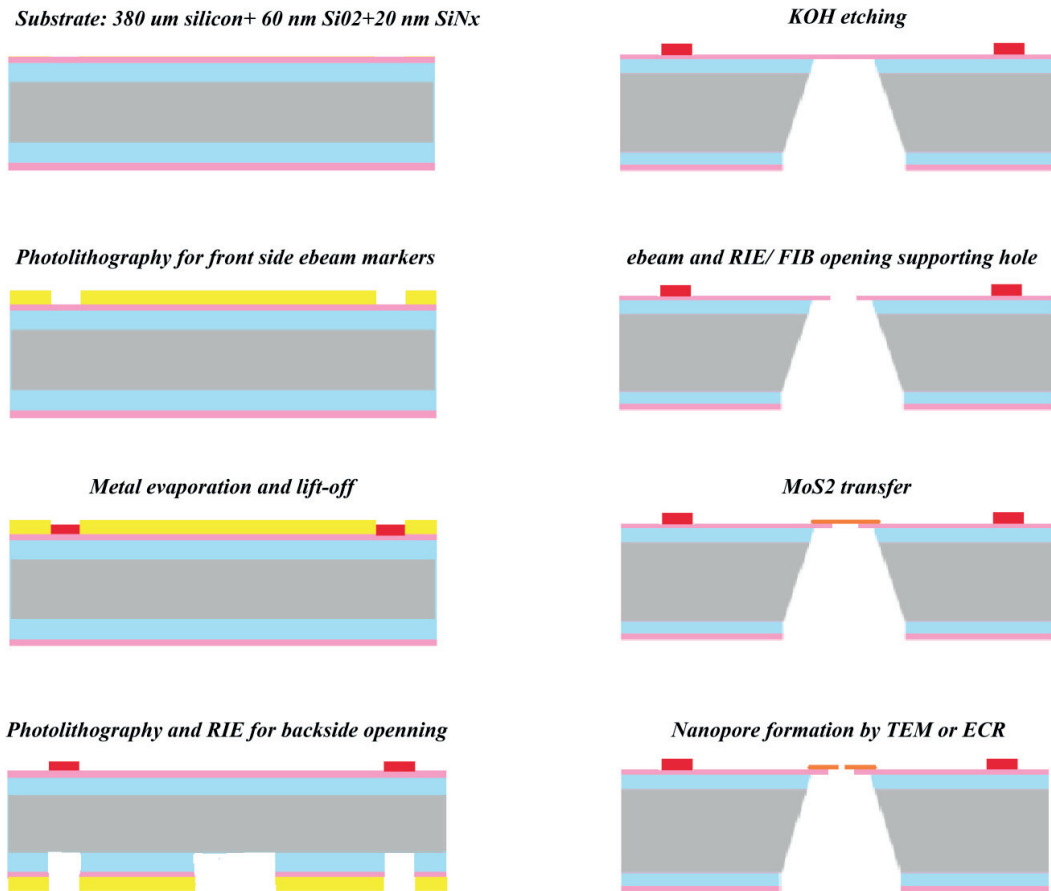


Figure 2.2. Process flow for the fabrication of MoS₂ nanopores.

At the beginning (2013), we used the widely adopted micromechanical exfoliation method[34] to exfoliate few-layer MoS₂ from natural MoS₂ bulky material onto the surface of substrates covered with 270 nm SiO₂ chips with fiducial markers. Later in 2014, Dr. Dumitru Dumcenco at Prof. Andras Kis's lab (Laboratory of Nanoscale Electronics and Structures) achieved chemical vapor deposition (CVD) growth of high-quality monolayer MoS₂ sample[95] (**Figure 2.3**). The CVD-grown sample was then implemented to our nanopore membrane fabrication, in replacement of the exfoliation method.

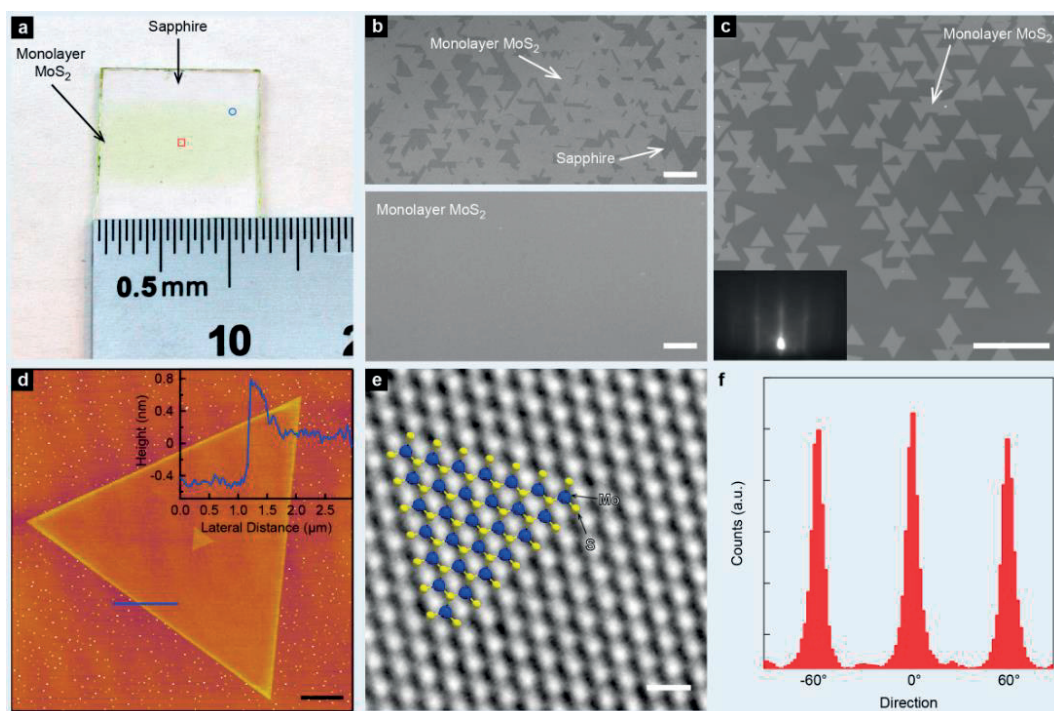


Figure 2.3. CVD growth of monolayer MoS₂. **a.** CVD-grown MoS₂ on sapphire substrate. **b.** Optical image of CVD MoS₂ scale bar length is 20 μm for top and 10 μm for bottom. **c.** long-range structural order confirmed by optical imaging (scale bar length is 50 μm) and Reflection high-energy electron diffraction pattern. **d.** Atomic force microscope images and thickness profile (2 μm scale bar). **e.** High resolution TEM image. **f.** Orientation histogram from **e.** Figure reproduced from ACS Publication[95]. Copyright (2015) American Chemical Society.

Subsequently, this flake (either exfoliated or CVD-grown) was transferred onto a square-shaped opening (ranging from 50 nm to 500 nm in size to reduce electric noise when flake in contact with ionic buffer) on the SiN_x supporting membrane using a standard graphene transfer method [96], as sketched in **Figure 2.4.**

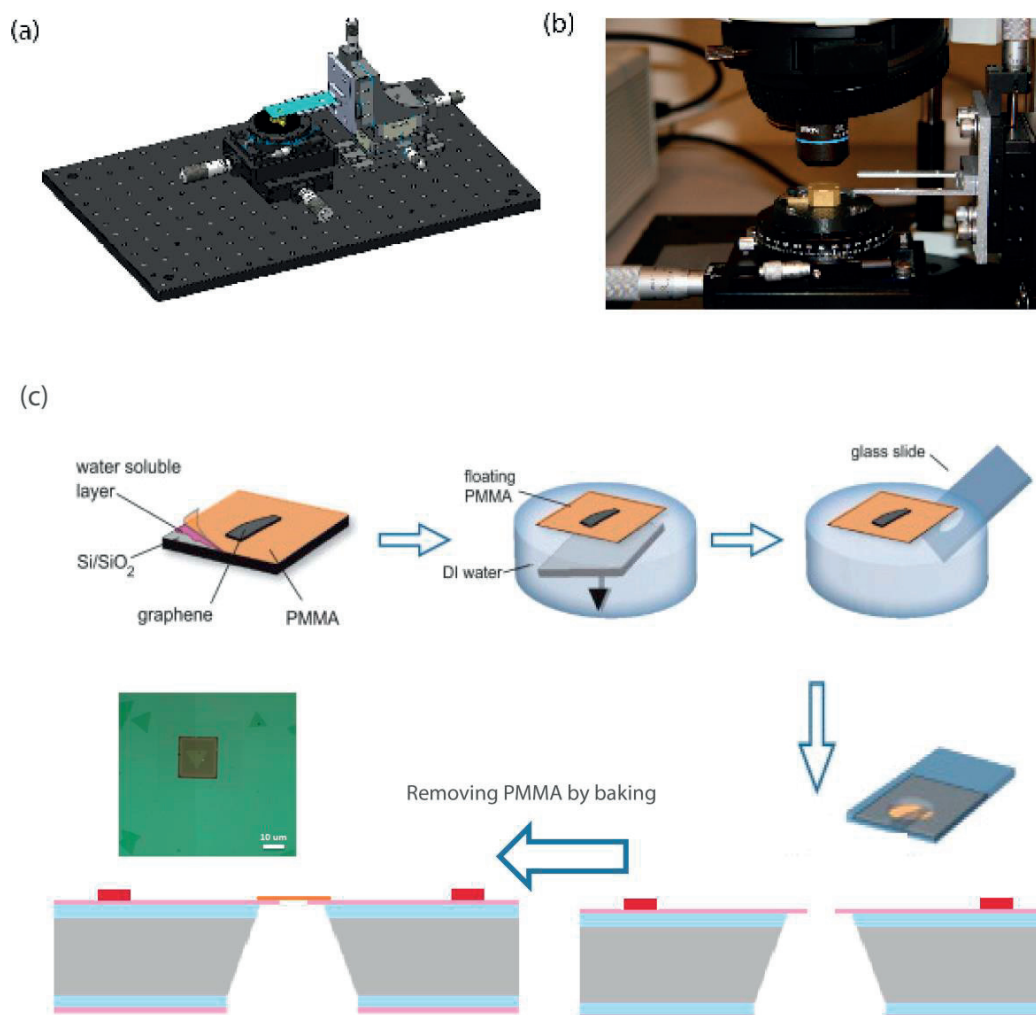


Figure 2.4. (a) and (b) show the custom-made transfer stage on an optical microscope, (c). PMMA-etching based MoS₂ transfer method. The MoS₂ sample is first coated with PMMA and detached by KOH etching. A coverslip is used to transfer the PMMA-MoS₂ flake to the pre-designed location. In the final step, PMMA is removed by annealing at 400⁰C under a H₂/Ar flux. Figure adapted from LANES.

The opening on SiN_x supporting membrane can be pre-designed by electron beam lithography followed by reactive ion etching or focused ion beam. A typical optical image of the transferred triangular flake of CVD-grown monolayer MoS₂ on the supporting silicon nitride membrane is shown in **Figure 2.5 b**. The freestanding MoS₂ membrane above the FIB defined opening can be further identified under TEM with low magnification (5 k×) as shown in **Figure 2.5 c**.

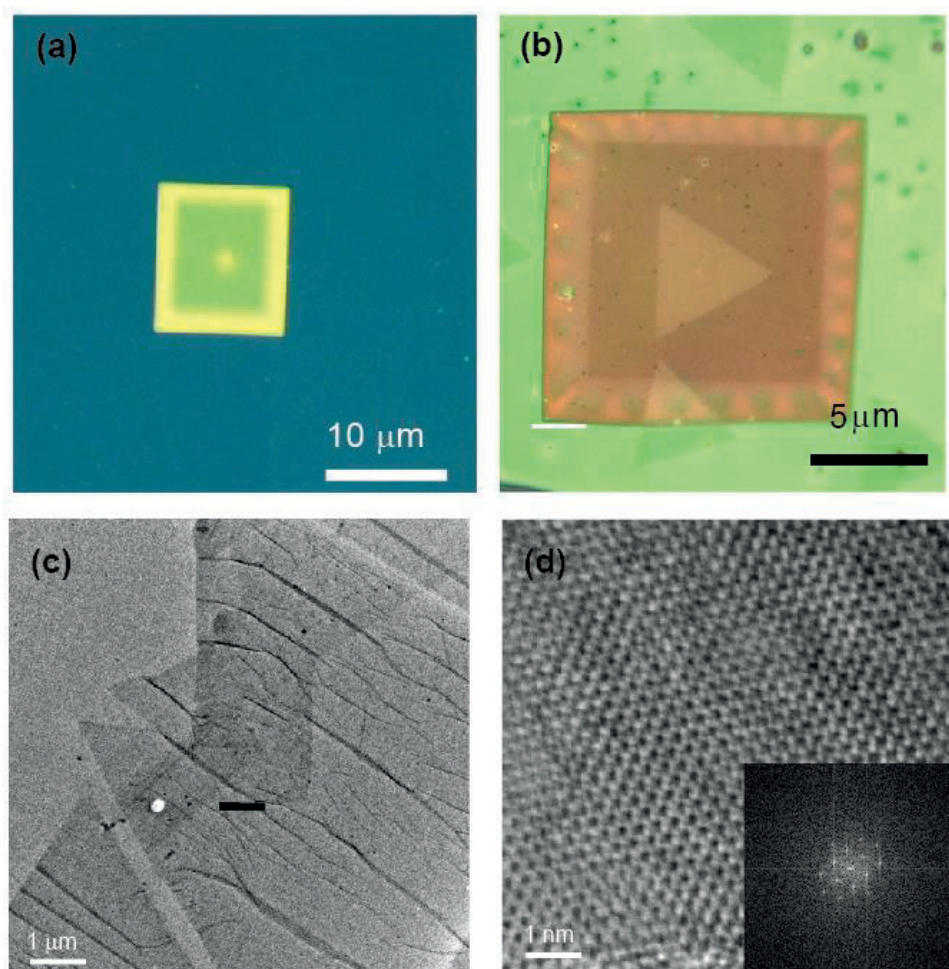


Figure 2.5. **a.** An optical image of the SiN_x membrane with a FIB drilled hole in the center. **b.** An optical image of the SiN_x membrane with transferred triangular CVD-grown MoS₂ monolayer. **c.** Low magnification TEM image of transferred CVD-grown MoS₂ monolayer covering the FIB hole. The FIB hole is indicated by the black arrow. **d.** Conventional high-resolution TEM image of the lattice of MoS₂ suspended over the FIB hole. The corresponding diffractogram is shown in the inset. Reprinted with permission from[97]. Copyright (2015) American Chemical Society.

To further verify the thickness of the chosen flake, we used atomic force microscopy (AFM) to obtain its height profile, as shown in **Figure 2.6 a and b**. The thickness is 9 Å from AFM measurements and is indicative of a monolayer, which is consistent with the optical observation. MoS₂ flake is further characterized by Energy-dispersive X-ray spectroscopy (EDX) in TEM to reveal the chemical composition. Elements of Mo

and S are abundant in the triangular areas as shown in **Figure 2.7**. When moving to the high magnification (1 M ×) and focusing on the freestanding portion of MoS₂ over the FIB opening, the atomic structure of MoS₂ can be clearly resolved as shown in **Figure 2.5 d**, and the diffractogram reflects the hexagonal symmetry of MoS₂, as shown in the inset of **Figure 2.5 d**.

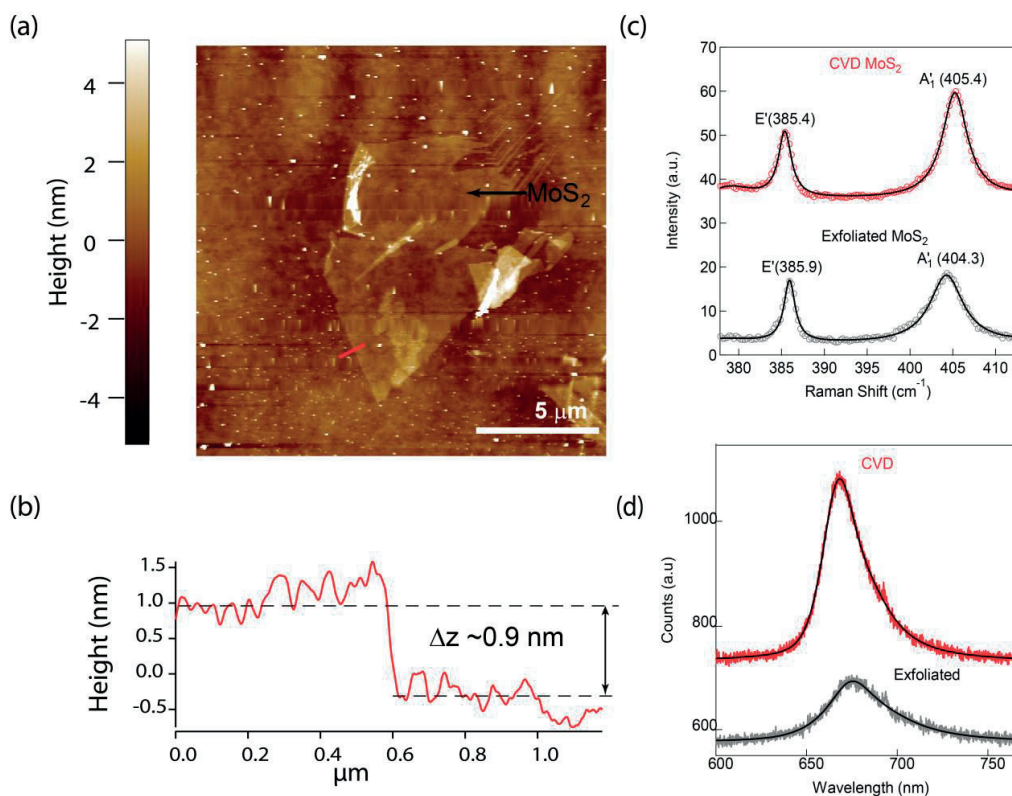


Figure 2.6. Verification of the thickness of MoS₂ membrane. **(a)** AFM image of MoS₂ membrane and **(b)** the thickness profile showing 0.9 nm thickness which corresponds to theoretical single layer thickness of MoS₂ 0.7nm. Reprinted with permission from[98]. Copyright (2015) American Chemical Society. **(c)** and **(d)** are the Raman spectra and photoluminescence spectra of as-grown monolayer MoS₂ on sapphire and monolayer MoS₂ exfoliated from bulk crystals and transferred onto sapphire, respectively. The contamination in AFM image may come from the polymer residual. Both Raman shift and photoluminescence excitation peak confirm the monolayer quality. Figure reproduced from ACS Publication[95]. Copyright (2015) American Chemical Society.

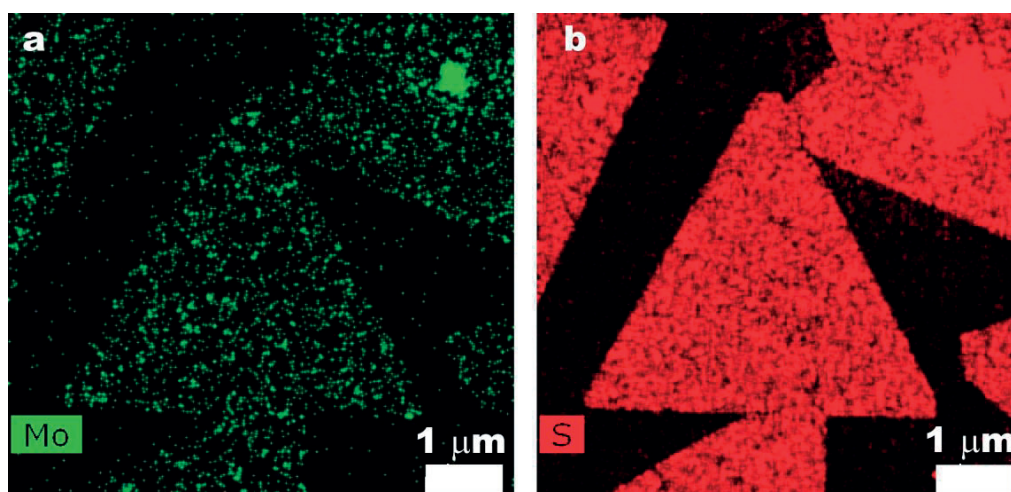


Figure 2.7. EDX mapping of Mo and S elements in the monolayer MoS₂ film composed of triangular single-crystal domains transferred on the supporting SiN_x membrane. FEI Tecnai Osiris TEM is operated in the STEM mode at 200 kV to achieve high speed and high sensitivity EDX measurements. To unambiguously decouple S from Mo Electron Energy Loss Spectroscopy (EELS) analysis of the samples would be required. Reprinted with permission from [97]. Copyright (2015) American Chemical Society.

2.4. Drilling and imaging single MoS₂ nanopores with TEM

The traditional method of fabricating nanopores with nanometer precision is based on the use of focused electron beams in transmission electron microscope (TEM) via electron irradiation. Nanopores were drilled using a JEOL 2200FS high-resolution transmission electron microscope. Nanopores are formed due to sputtering, localized heating fluidizes matter and surface tension when in contact with an electron beam.

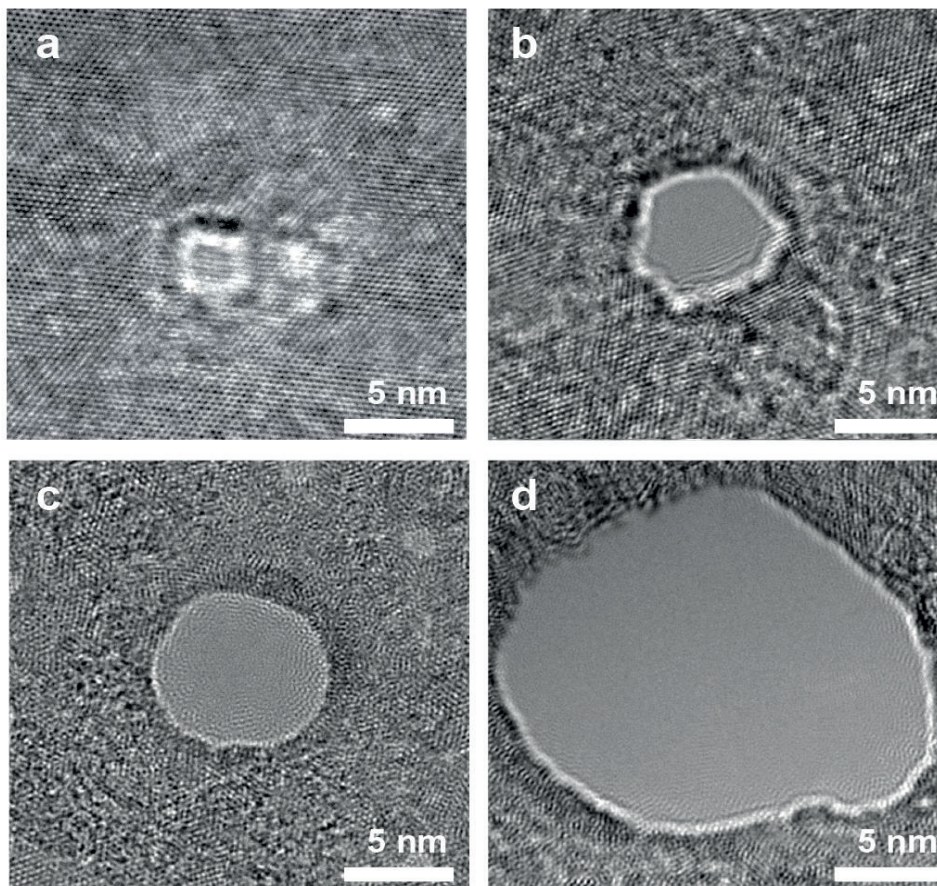


Figure 2.8. High-resolution TEM images of nanopores with various sizes drilled by a focused electron beam. **a.** 1 nm, **b.** 5 nm, **c.** 7.5 nm, **d.** 20 nm. The lattice of MoS₂ is visible under such a magnification. Controlling the shape of MoS₂ pores by TEM drilling is difficult as the drilling process is very fast. Reprinted with permission from [98]. Copyright (2015) American Chemical Society.

Drilling process lasts only for several seconds after which a nanometer-sized pore appears in single layer MoS₂, in contrast to the minute-drilling process with 20 nm silicon nitride membrane. Therefore, a good thermal and mechanical stability is highly preferred for such a short drilling period, especially in the case of small pores. We prefer to blank the beam for several minutes before the drilling process in order to minimize the drift for the both beam and the sample. The beam is then focused to the desirable location for pore drilling. TEM images are taken immediately after pore drilling. Most devices are drilled under 200 keV and other TEM parameters like used

spot size vary from pore to pore. **Figure 2.8 a-d** shows several examples of nanopores with various sizes. Therefore, we want to infer that nanopores can be sculpted atom by atom using a highly focused electron beam, where both the diameter and the shape of the pore can be tuned at the atomic level. However, it is difficult to achieve high quality TEM images since electron irradiation can also damage the sample during imaging, particularly in the case of 2D materials, like graphene or MoS₂. Therefore, to avoid the damaging, lower beam energy (60 keV or 80 keV) is also suggested.

2.5. Voltage-induced electrochemical reaction in MoS₂ nanopores

MoS₂, as a member of transition metal dichalcogenide (TMD) family, has rich electrochemical properties such as catalytic hydrogen generation[99]. During the past several decades, scanning probe microscopes (SPMs) such as scanning tunneling microscopes (STM) and atomic force microscopes (AFM), demonstrated ability to craft nanostructures with an atom/molecule resolution. In SPM, using tip-induced electrochemical reaction, it is possible to engineer nanostructures or make holes in layered TMDs (WSe₂, SnSe₂, MoSe₂ or MoS₂). The mechanism can be understood as a surface electrochemical reaction scheme induced via the electric field generated by the SPM tip[100, 101]. The oxidation process starts preferably at the surface defects when the voltage threshold (1.2 V in the case of WSe₂)[101] for oxidation is reached and allows variety of nanoengineering means. However, it is still challenging to make nanopores on suspended membranes using SPMs, while on the other hand implementation of SPMs instrument in nanopore fabrication is comparable to TEMs in terms of cost and complexity.

Here we present *in-situ* application of the electrochemical reaction (ECR) for fabrication of individual nanopores on single-layer MoS₂, with the electric field generated by Ag/AgCl electrodes away from the membrane. ECR starts for a certain critical voltage bias at a defect/vacancy present in the MoS₂ membrane.

Importantly, in the course of ECR fabrication we observe – and we are able to control – the successive removal of single or few MoS₂ units from the monolayer MoS₂ membranes. In this way we accomplish the atom-by-atom nanopore engineering. To

Chapter 2. Fabrication: engineering individual MoS₂ nanopores

the best of our knowledge, this is the first example of nanopore engineering on single-layer MoS₂ membranes with atomic precision utilizing ECR.

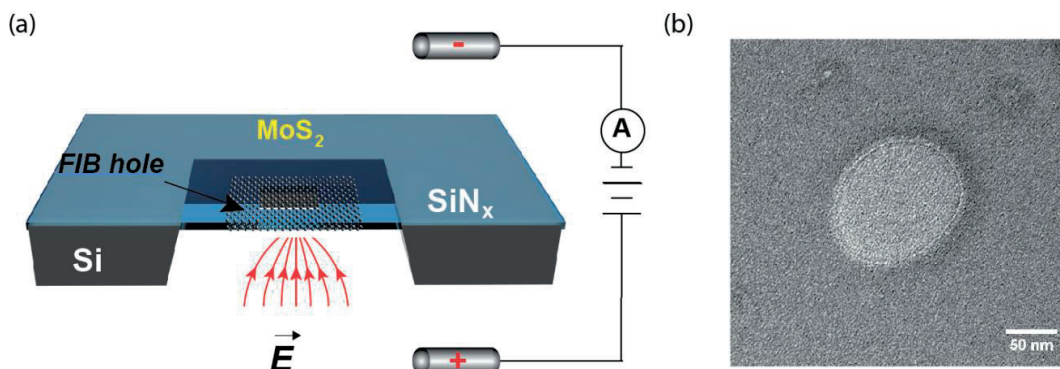


Figure 2.9. **a.** Schematic illustration of preparation of a freestanding MoS₂ membrane ready for electrochemical formation of a nanopore. In the center of the supporting 20 nm thick SiN_x membrane a single focused ion beam, FIB hole is drilled to suspend a small portion of an intact monolayer MoS₂ flake. A single chip is mounted in the flow-cell for typical translocation experiments. A pair of Ag/AgCl electrodes connected to a preamplifier is used to apply transmembrane voltage. **b.** TEM image of free-standing MoS₂ membrane on a 100 nm FIB opening. Reprinted with permission from[97]. Copyright (2015) American Chemical Society.

The procedure for fabricating MoS₂ nanopores using ECR is schematically illustrated in **Figure 2.9 a**, where two chambers (*cis* and *trans*) are filled with aqueous buffer (1M KCl, pH 7.4) and biased by a pair of Ag/AgCl electrodes which are separated by a single-layer MoS₂ membrane. Freestanding MoS₂ membrane prior to ECR is shown in **Figure 2.9 b**. The presence of an active site such as single-atom vacancy[102] facilitates the removal of individual atoms and MoS₂ unit cells from MoS₂ lattice by ECR at voltages higher than the oxidation potential of MoS₂ in aqueous media. This process is facilitated by the electric field focusing by the pore itself.

When an intact MoS₂ membrane is mounted into a custom made microfluidic flow-cell filled with an aqueous buffer, transmembrane potential is applied using a pair of Ag/AgCl electrodes. For a voltage bias below the potential for electrochemical oxidation, small leakage current is normally detected, typically on the order from tens to hundreds of picoamperes depending on the number of defects in the 2D membrane[103]. The leakage current displays a non-ohmic characteristic. To reach

the critical voltage bias value for ECR, the potential is gradually stepped, as shown in **Figure 2.10**. When the applied voltage is stepped up to 0.8 V (a critical voltage, indicated by the arrow), an increase of baseline current immediately occurs. This time-point indicates the nanopore creation which is associated to the electrochemical dissolution of MoS₂ enhanced by the ion flow focused on the active site.

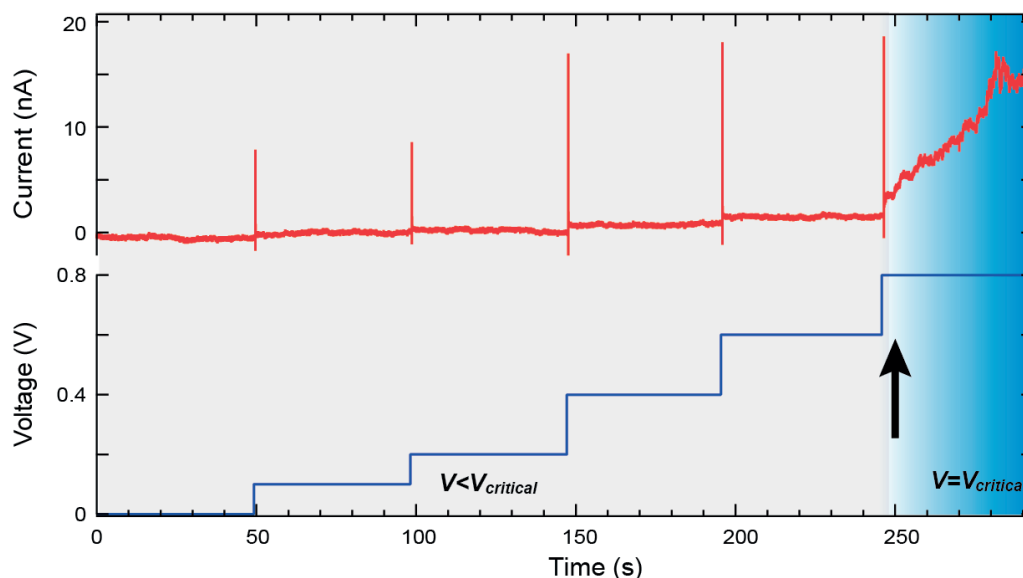


Figure 2.10. Voltage-induced ECR. A representative ionic current trace measured for an MoS₂ membrane. Voltage is stepped by 100 mV with a 50 s holding, and the leakage current increases in accordance, being steady for a constant voltage. Sharp peaks at each voltage step originate from the capacitance charging. After a critical voltage, 800 mV is applied, the electrochemical reaction, ECR starts (indicated by the black arrow), the current keeps increasing which triggers the feedback control to switch off voltage bias in order to halt the pore growth. Reprinted with permission from[97]. Copyright (2015) American Chemical Society.

In contrast to the avalanche-like dielectric breakdown process in silicon nitride, where a typically 10-minute waiting time for the filling of charge traps[104] under the application of critical voltage (> 10 V) is needed before breakdown occurs, electrochemical dissolution happens spontaneously at the critical voltage.

In addition, the observed rise of ionic current shows a quite slow rate (~ 0.4 nA/s). The control on the nanopore size is obtained by using an automatic feedback to cut off

the voltage once the desired current/conductance threshold is reached. This feedback also helps to avoid multiple pore formation. Owing to the limited rates of electrochemical reaction, the MoS₂ nanopore sculpting process is quite slow, occurring on time scales of dozens of seconds to several minutes. **Figure 2.10** gives an example of ionic current trace to reach the threshold of 20 nA, for the critical voltage of 0.8 V.

2.6. MoS₂ nanopore formation and characterization

Taking the advantage of existing theoretical insights to model the conductance-pore size relation, the conductance of the nanopore (G) can be described by[105]

$$G = \sigma \left[\frac{4L}{\pi d^2} + \frac{1}{d} \right]^{-1} \tag{2-1}$$

where σ , L and d are the ionic conductivity of solution, membrane thickness and nanopore diameter, respectively. In order to verify the applicability of above hall equation, we first calibrate it with TEM-drilled MoS₂ nanopores where we can directly obtain pore size. These calibration results are given in **Figure 2.11**. Using a nonlinear fit, we find L with a value of 1.6 ± 0.2 nm, reflecting an atomically thin feature of the MoS₂ membranes. We find σ with a value of 17.5 ± 1.5 S m⁻¹, which is in a good agreement with ionic conductivity of 2 M KCl (20 S m⁻¹)[105]. Therefore, both fits are suitable.

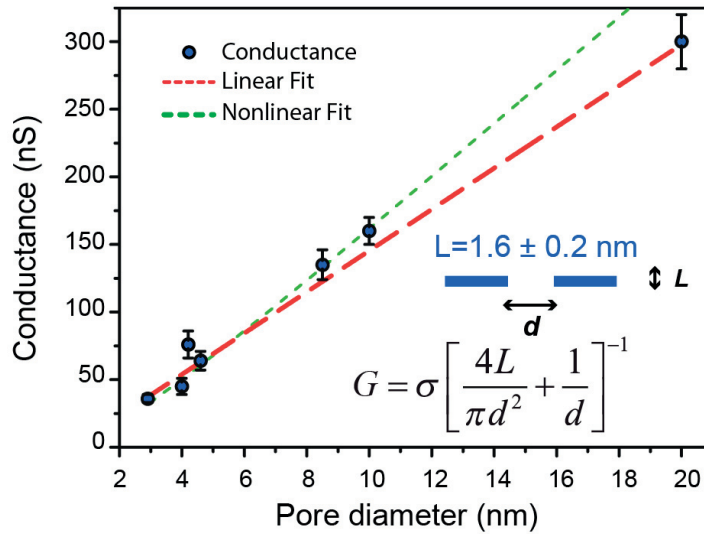


Figure 2.11. Calibration of conductance-pore size equation using TEM drilled MoS₂ nanopores. Conductances are derived from linear fits of IV measurements in 2 M KCl with bias voltage swept from -0.5 V to $+0.5$ V. In order to exclude either leaking pores $G > 300$ nS or clogged pores $G < 10$ nS, we used only devices displaying conductances higher than 10 nS and lower than 300 nS. Error bars of the pore diameters indicate the asymmetry of the pores. Inset shows a simple scheme for the thin membrane with a nanopore and related equation to describe conductance, where G is conductance, σ is ionic conductivity, L is thickness and d is pore diameter. The nonlinear fitting (green line) is based on the eq. 1 shown in the inset to subtract L . And the linear fitting (red line) is based on the simplified equation 2.1, $G = \sigma d$, to subtract σ . Reprinted with permission from [98]. Copyright (2015) American Chemical Society.

Using this relation in combination with feedback on ECR that immediately stops the voltage once the desired pore conductance that corresponds to a certain pore size is reached, we were able to fabricate pores ranging in diameter from 1-20 nm. **Figure 2.12 a** reveals current-voltage (I-V) characteristics of MoS₂ nanopores fabricated by ECR with different estimated sizes ranging from 1 nm to 20 nm. The symmetric and linear I-V curves also imply the well-defined shape of the fabricated pores. Similarly, as shown in the inset of the **Figure 2.12 a**, I-V characteristics across the membrane have been investigated in situ before and after ECR, confirming the pore formation.

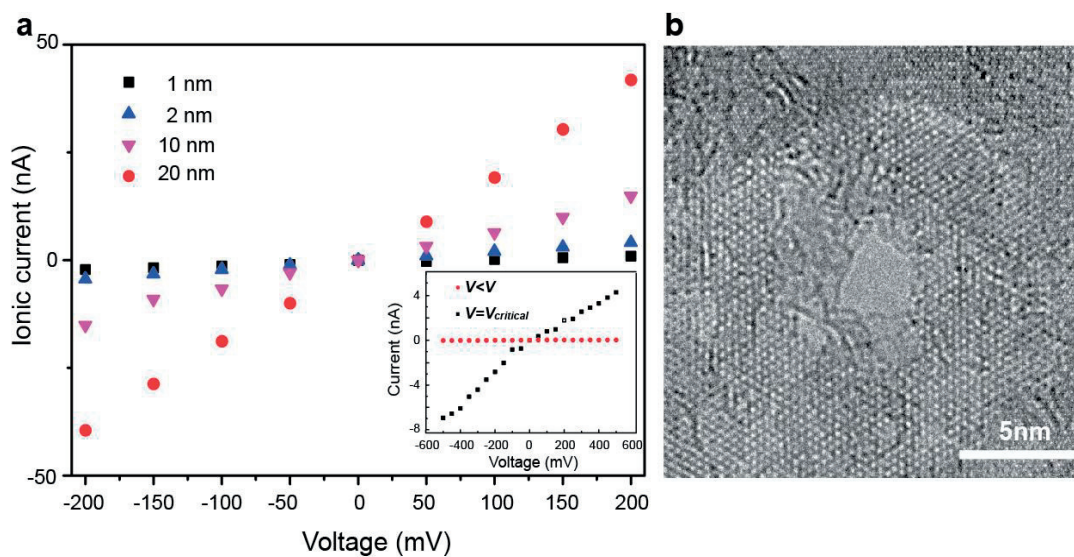


Figure 2.12. (a) Current-voltage (IV) characteristic of nanopores ranging in diameter from 1 to 20 nm - all nanopores are created via electrochemical reaction. Inset shows IV characteristics for the system below and at the critical voltage. **(b)** Cs-TEM image taken at 80 keV incident beam energy verifies the nanopore formation and estimated size (3.0 nm) of nanopore created using ECR. (Diameter measured in image ~3 nm). Reprinted with permission from[97]. Copyright (2015) American Chemical Society

To further verify the size of fabricated MoS₂ nanopores, TEM has been used to image the newly formed nanopore. Exposure of 2D materials to electron radiation can induce large area damage and also open pores, as reported for both graphene[106, 107] and MoS₂[107]. To minimize this risk we imaged the pore using Cs-corrected high-resolution TEM (Cs-TEM) at primary beam energy of 80 keV, using a double-corrected FEI Titan Themis 60-300 keV. (We note that, while Cs-corrected scanning TEM (Cs-STEM) gives more directly-interpretable atomic structure contrast, its application here was precluded because of residual hydrocarbon contamination from the prior ECR process condensing rapidly under the Å-sized probe during imaging. A better sample cleaning procedure would be required to realize successfully Cs-STEM imaging of the ECR pore.) We first aligned the imaging condition on the unsuspending portion of MoS₂ outside of the FIB opening and then quickly scanned the suspended monolayer region to find and image the ECR-fabricated pore, all the while taking care to irradiate it minimally **Figure 2.12 b** shows the resultant image of an ECR-fabricated MoS₂ nanopore, corresponding to its pore size confirmed by the current voltage characteristics taken after ECR.

The reliability of fabricating MoS₂ nanopores using the ECR technique is 90% and is under commercialization. A few graphene membranes have also been tested by this method and higher voltages (2-3 V) are required to fabricate pores. More details can be found in our published paper Feng et al.

The described ECR-based pore formation method benefits from the unique crystal structure of transition metal dichalcogenide (MX₂) where atoms are situated in two planes and linked by metal-chalcogenide bonds while in the case of graphene, carbon atoms are in the same plane and 3 bonds need to be removed to release one carbon atom. In addition, to remove carbon atoms, graphene needs to be oxidized to a higher valence state which presumably requires a higher voltage bias.

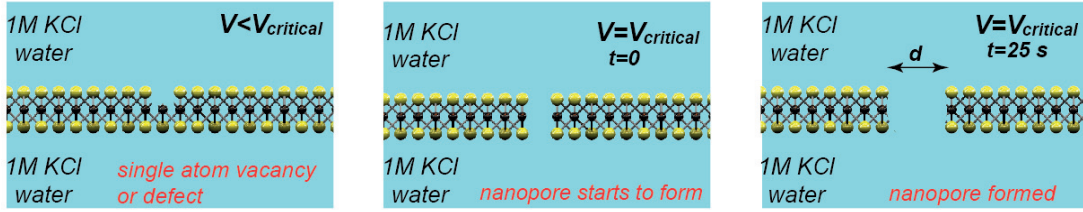
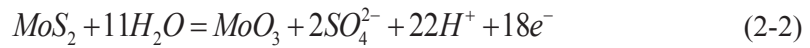


Figure 2.13. Proposed mechanism of ECR based MoS₂ nanopore fabrication. A side view of the monolayer MoS₂ lattice, emphasizing the lattice having single atom (S) vacancy before ECR $V < V_{critical}$, MoS₂ lattice at $V = V_{critical}$ and MoS₂ lattice when nanopore is formed. Reprinted with permission from[97]. Copyright (2015) American Chemical Society.

Despite different chemical compositions of transition metal dichalcogenides (MX₂), the pore formation mechanism is in general governed by the electrochemical oxidation reaction that occurs at the location of the defect and requires comparable field strengths to those encountered in SPMs[100, 101]. In our case, mechanical avulsion is highly unlikely to occur since the force is insufficient, similarly to measured results by SPM experiments. The critical voltage 1.2 V for WSe₂ is in good agreement with our observations (0.8 V for MoS₂), especially if we consider the position in energy of the surface band edges. The physics of the electrochemically fabricated nanopores is determined by the focused electrical field and surface chemistries. The electric field concentrates at surface irregularities or defects which can be considered as surface active sites, and focuses current flow at the site of the pore, and thus locally enhances the electrochemical dissolution, as shown in **Figure 2.13**. The surface dissolution chemistries can be understood as a surface bound oxidation scheme with hole capture and electron injection to produce the MoS₂ oxidation state as shown in[108],



where MoS₂ is oxidized into MoO₃ which detached into the solution. We believe this reaction is highly likely to happen considering the electrical potential (voltage bias) range we work with. Due to the current technical limitations of electron energy loss spectroscopy (EELS) analysis in the nanopore vicinity, we cannot exclude the possibility that MoS₂ is oxidized to other valence states. Once an active site is

removed by the process described above and very small nanopore formed **Figure 2.13**, due to the fact that the nanopore has a much larger resistance than the electrolyte solution, the flux of the ions will converge towards the pore. This focused ionic current through the pore will locally enhance the electrochemical dissolution as previously described by Beale model[109]. In addition, it is possible that the high number of dangling bonds within the nanopore contributes to the more favorable enlargement of a single nanopore rather than nucleation of the many pores. Of course in the presence of many defects, correlated to the material quality in the suspended area, it is hard to eliminate the possibility that one has created multiple pores. By applying a bias voltage higher than the critical voltage at the beginning of the fabrication process it might be possible to observe the formation of multiple pores. Given the stochastic nature of the pore creation process, with our configuration of voltage steps, multiple simultaneous nanoscale ECR events are highly unlikely. Furthermore, feedback control on the applied voltage to obtain the desirable conductance ensures the formation of a single nanopore. Finally, the formation of a single nanopore is verified by TEM imaging. By establishing the correspondence of nanopore conductance to TEM images of their size, in the future we hope that this step could be omitted.

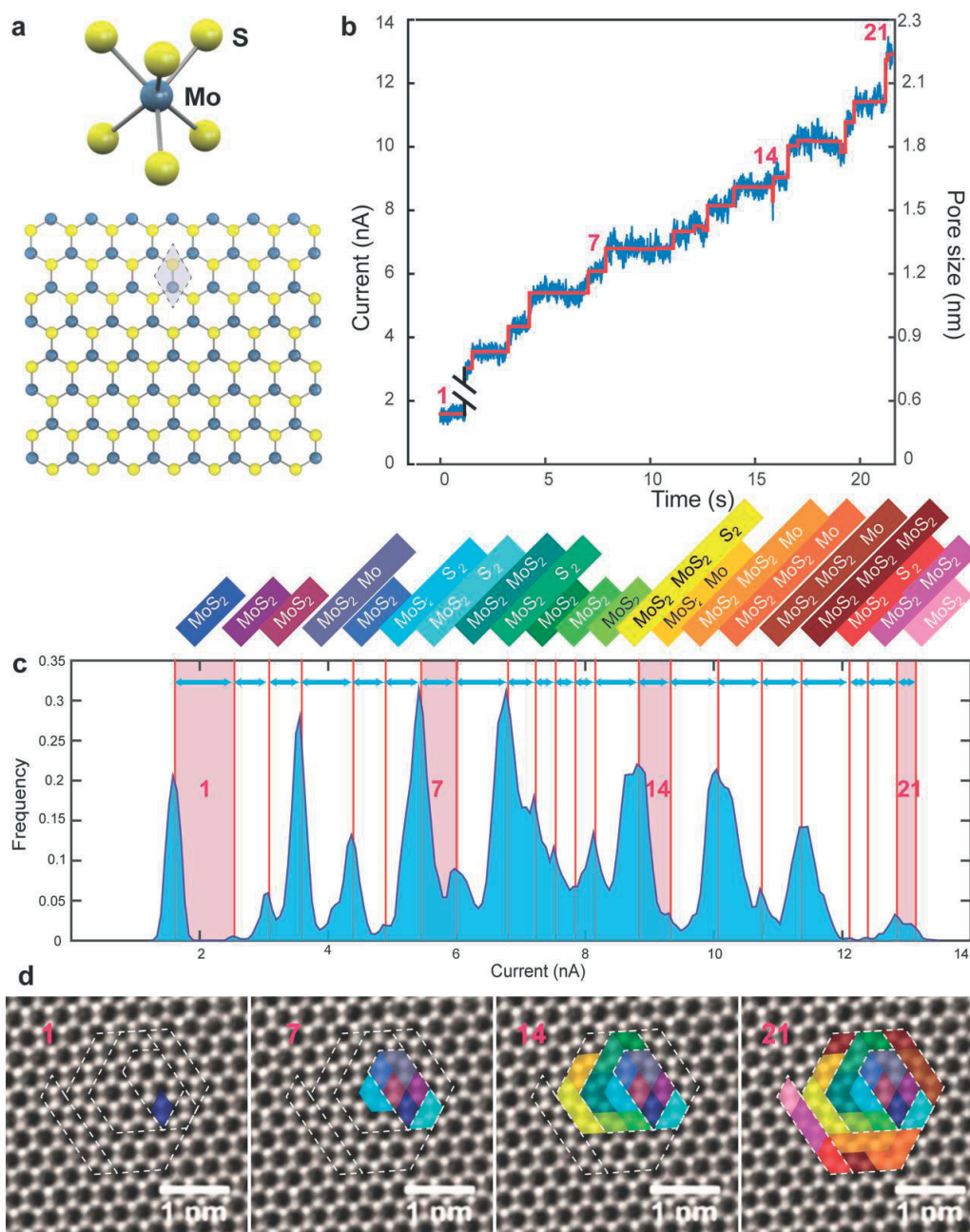


Figure 2.14. (a) A top view of the monolayer MoS₂ lattice, the unit cell (parameter $a=3.12 \text{ \AA}$) is shown in grey[110]. (b) Ionic current -steplike features during the nanopore formation in **Figure 2.10**. A custom Matlab code is used to detect steps in the raw trace[111]. (c) Histogram of the trace shown in (b) with the corresponding color coded atom groups cleaved in each step during the pore formation. (d) Illustrative schematic that presents a possible outline for nanopore creation. Polygon removal corresponds to the current histogram trace. Cs-STEM micrograph of

suspended single layer MoS₂ with superimposed polygons corresponding to atomic groups cleaved in the steps 1,7,14 and 21 during the pore formation. The coloring of atom groups cleaved in each step (c) and corresponding area polygons shown in the d starts from violet, blue, cyan and green to yellow, orange, brown, red and magenta – analogous to the visible spectrum sequence. Reprinted with permission from[97]. Copyright (2015) American Chemical Society.

The power of ECR-based nanopore fabrication technique, apart from the advantages of being a fast and cheap production lies in the possibility of fine-tuning the diameter of nanopores with unprecedented, single-atom precision. The low nanopore enlarging speed is due to low voltages and the electrochemical dissolution nature of the process. **Figure 2.14 b** is a 25-second long, continuous pore conductance trace that shows atomic precision during nanopore sculpting process. The trace starts from the critical point indicated in **Figure 2.10**. Fitting to the conductance-nanopore size relation, we can estimate a pore diameter growth rate of about 1 Å per second. After 25 seconds a pore with a diameter 1.9 nm (area of 2,9 nm²) has been formed. The area of such a pore is equivalent to almost exactly $N = 34$ unit cells of MoS₂ where the area of the unit cell $u = 0.0864$ nm² (**Figure 2.14**). Reprinted with permission from[97]. Copyright (2015) American Chemical Society.

To our surprise, the growth curve is not linear but step-like, as shown in **Figure 2.14 b**. Necessarily, the effective size of the pore enlarges with the same step-like characteristic. To gain insights into these step-like features, we plotted the histogram of current values from this trace in **Figure 2.14 c**, where 21 individual peaks can be extracted from the histogram.

The sequence of the pore size enlargement steps may be normalized by the unit cell area u and a sequence of MoS₂ formula units and Mo and S atoms cleaved (corresponding to 21 current steps) to form the pore may be inferred. The area of polygons corresponding to the cleaved atom groups follows the honeycomb structure of single-layer MoS₂, as presented schematically in **Figure 2.14 a** and in the cleavage steps superimposed on a Cs-STEM image of MoS₂ lattice, **Figure 2.14 d**.

Here presented, step-like features are commonly observed when working with low voltages ranging from 0.8-2 V. The observed atomic steps here reveal the ultimate precision (single atoms) that can be reached in engineering nanostructures.

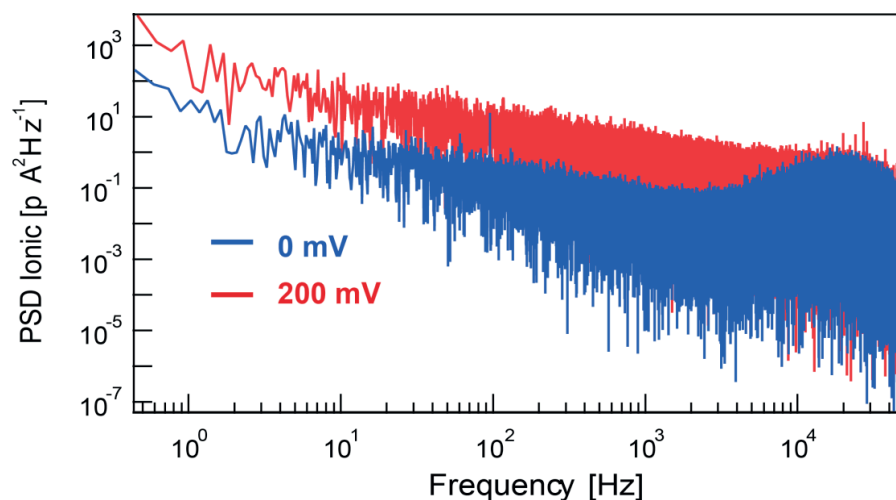


Figure 2.15. Power density spectrum (PSD) noise analysis of an ECR fabricated MoS₂ nanopore at the transmembrane voltages of 0 mV (blue) and 200 mV (red), respectively. A short fragment at each voltage of ionic current trace is chosen for such an analysis. Reprinted with permission from [97]. Copyright (2015) American Chemical Society.

To test the performance of ECR-fabricated pores, we performed DNA translocation experiments and detected the translocation events by the current drops below the baseline current. ECR fabricated MoS₂ nanopores consistently produces low- $1/f$ noise on the current baseline, which is slightly higher than TEM drilled MoS₂ nanopores (**Figure 2.15**). The major contribution to the $1/f$ noise in 2D membrane nanopores [112] can be attributed to mechanical fluctuations of the thin membranes. Higher frequency fluctuations are produced by the method itself. Fluctuation noise can be significantly reduced by using a smaller supporting opening [50], or operating at low temperatures.

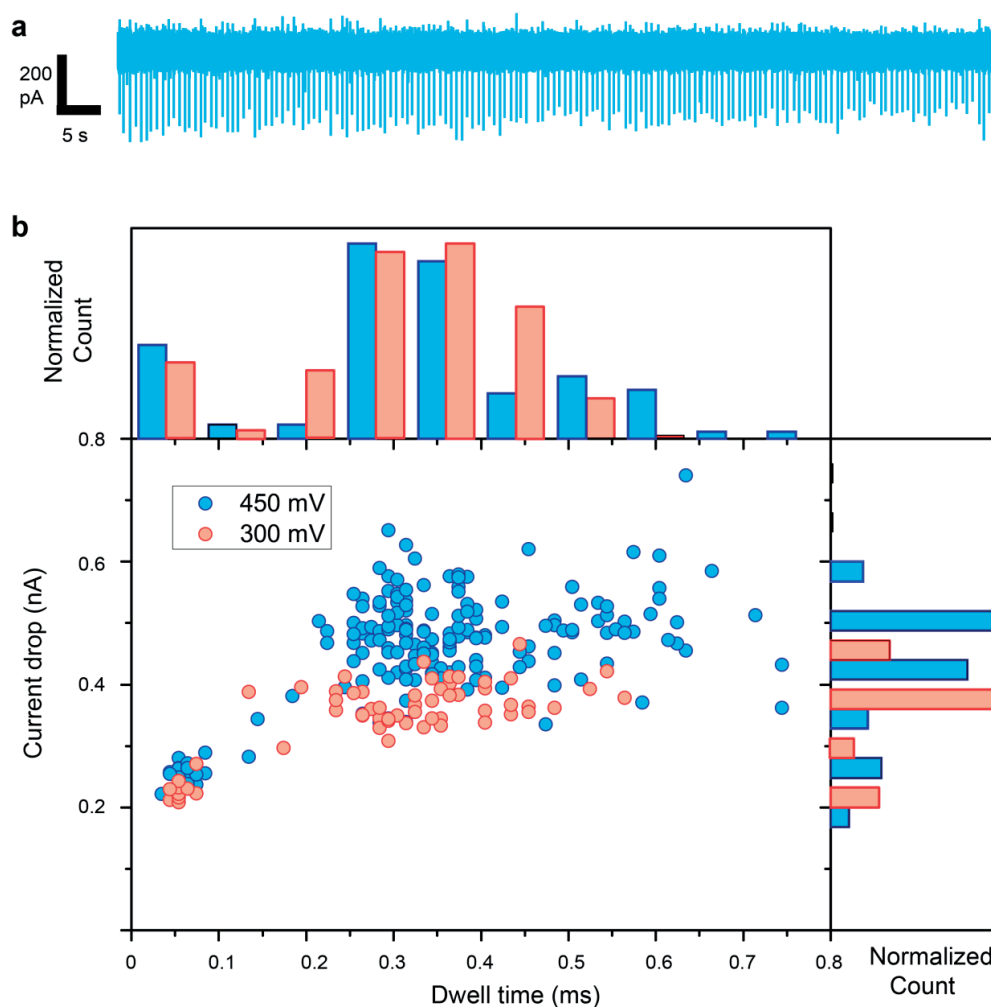


Figure 2.16. (a) A typical trace of pNEB plasmid DNA translocation through an electrochemically etched nanopore recorded at 450 mV. The trace is downsampled to 10 kHz for display. (b) Scatter plot of events collected at 300 mV and 450 mV bias. Event detection is performed using OpenNanopore[111] Matlab code. Expectedly, the increase in the bias shortens the translocation time and enhances the current drop. Considerably longer term operation of the nanopore device is possible since DNA does not adhere to MoS₂. Reprinted with permission from[97]. Copyright (2015) American Chemical Society.

To show the ability of ECR fabricated nanopore for DNA detection, 2.7 kbp pNEB plasmid DNA is translocated through a relatively large MoS₂ nanopore (30-40 nm) to eliminate the pore-DNA interaction and multiple conformation issues. **Figure 2.16 a.** displays only one-level events indicating an extended (unfolded) DNA conformation, with SNR >10. Scatter plots are used to describe the statistics of DNA translocation as

shown in **Figure 2.16 b**. The signal amplitude also increases linearly with the applied voltage, which is 0.5 nA for 450 mV and 0.38 nA for 300 mV as shown in the histogram **Figure 2.16 b**. Dwell times are also comparable with DNA translocation through a TEM-drilled MoS₂ nanopore of a similar diameter, for the same DNA and under same bias conditions. In addition, λ -DNA (48 k bp) is also translocated through an ECR-fabricated nanopore shown in (**Figure 2.17**). A noticeable advantage of this nanopore fabrication method is that DNA translocations can be performed *in situ* after ECR and size-control allows on-demand adaptation of the pore size, allowing sizing for the different types of biomolecules, e.g. proteins[113] or DNA-protein complexes[114].

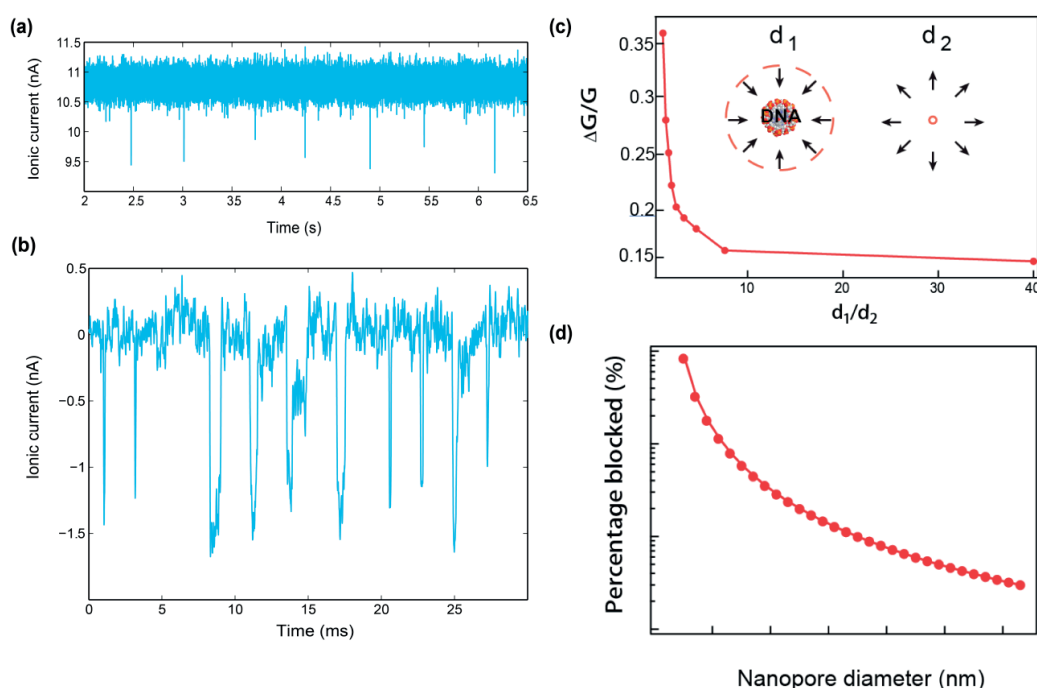


Figure 2.17. Verification of single pore formation by DNA translocation. **(a)** Long trace showing the lambda-DNA translocations through a 4.3 nm ECR fabricated MoS₂ nanopore recorded in-situ right after pore formation at 300 mV. **(b)** Concatenated lambda-DNA translocation events. **(c)** Simplistic analytical model that relates normalized conductance drops to the ratio of the sizes of the 2 pores. Initial nanopore diameters are set to $d_1=4.2$ nm and $d_2=0.1$ nm. We varied the sizes of the both pores while keeping the total conductance fixed. **(d)** Percentage of the blocked ionic current as a function of nanopore diameter. More rigorous model is provided by Garaj et al.

Chapter 2. Fabrication: engineering individual MoS₂ nanopores

[50]. Surprisingly our simplistic model agrees well with Garaj et al. [50] Reprinted with permission from [97]. Copyright (2015) American Chemical Society.

In addition, to verify the single pore formation for the small nanopore sizes < 5 nm, λ -DNA (48 k bp) is also translocated through 4.3 nm large ECR-fabricated nanopore (**Figure 2.17 a and b**). As shown in **Figure 2.17 c**, obtained from the simplistic model that assumes two pores, conductance drop will strongly depend on the ratio of the two pore sizes. The experimentally observed blockage 11% (**Figure 2.17 d**) is in a good agreement with the assumption of single 4.3 nm pore. For the larger pore sizes 15-30 nm this simplistic analytical model is less reliable since the conductance drop caused by DNA translocation varies slightly.

Apart from nanopore sensors, other applications can be further explored based on the conductance quantification such as selective ion transport, nanoionics [115], and atomic switches or as platforms for understanding electrochemical kinetics [116]. To conclude, we present the atomically controlled electrochemical etching of single-layer MoS₂ which we employ to engineer nanopores with sub-nanometer precision. The fabricated MoS₂ nanopores are carefully characterized by I-V characteristics and their size confirmed by TEM. We attribute the fabrication process to the local concentrated field at surface defects and the electrochemical dissolution of the MoS₂. The intrinsic electrochemical reaction kinetics permits the ultimate precision for nanopore fabrication. We have observed the step-like features in the ionic current traces, which we attribute to the successive removal of individual atoms. Finally, DNA translocation has been performed to demonstrate the ability such nanopores in detecting molecules. The ECR nanopore fabrication technique presented here offers a well-controlled method to engineer nanopores at single-atom precision and also paves a practical way to scale up the production of 2D nanopores and commercialize nanopore-based technologies.

Chapter 3. Nucleotide structures probed by MoS₂ nanopores

3.1. Introduction

Recent years witnessed significant demand and research activity in the development of new DNA sequencing technologies. Nanopore-based sequencing presents attractive alternative to existing technology since in its concept it should provide a fast, single-molecule, label free, amplification free, inexpensive, high-throughput sequencing technology. Biological pores, alpha-hemolysin and MspA have already reported experimental realization of single-nucleotide resolution[49, 117]. Recently, Oxford Nanopore has announced their first-generation sequencer using bio-engineered pores. However, the abovementioned sequencing using bio-engineered pores requires enzymes, which limits the sequencing speed of single pore to 70 nt/s. This is no significant improvement on traditional methods (practical use requires integration of nanopore array) and keeps the costs high due to the use of enzymes. This is not what researchers originally expected from nanopore sequencing. Moreover, ditching the proteins could also pave the way to even cheaper devices that take advantage of semiconductor manufacturing technology to mass-produce and shrink these sequencers. Besides using SiN_x, recently advance in employing solid-state materials as ultrathin membranes for nanopore varies from SiN_x, single-wall carbon nanotubes[64], graphene[35] to DNA origami[66] and graphene nanopore has addressed the required spatial resolution while the fast DNA translocation dynamics makes sequencing with solid-state pores a challenge.

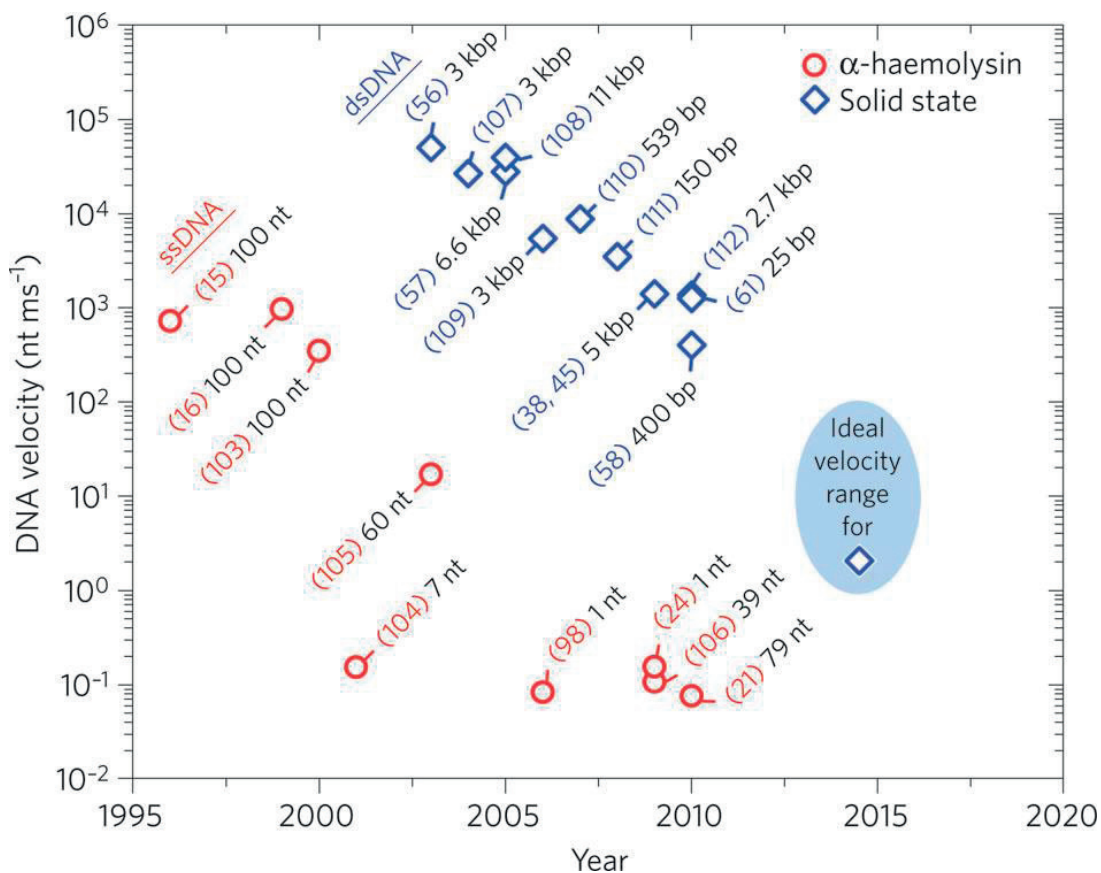


Figure 3.1. Average DNA translocation velocity in nucleotides per millisecond (on a logarithmic scale) versus year for both ssDNA and dsDNA and for both α -haemolysin and solid-state nanopores. Figure reproduced from Nature Publication[54] with permission.

In this chapter, we demonstrate for the first time single-nucleotide identification using solid-state nanopores with optimal speed for DNA sequencing 1-50 nt/ms. To realize this, we made a pore in atomically thin MoS₂ and combined it with a viscosity gradient system based on a room-temperature ionic liquid (RTIL).

Single-layer MoS₂ is sufficiently thin to allow single nucleotide fingerprinting, while the viscosity gradient system based on the room temperature ionic liquid (RTIL) as solvents for DNA translocation provides the means to slow down the DNA translocation through the nanopore which would otherwise be too fast. By implementing the viscosity gradient, we improve current temporal resolution in solid-

state nanopores by 2 to 3 orders of magnitude and without compromising the signal-to-noise ratio. This improvement puts us in the ideal velocity range for DNA sequencing as indicated in **Figure 3.1**, taken from a review paper written in 2011[54]. As predicted, in early 2014 we have reached the optimal speed for DNA sequencing using solid-state nanopores.

The use of MoS₂, a material with direct bandgap, opens up the possibility of high-throughput sequencing technology by means of transverse based detection. In our recent work with graphene nanoribbons we have already established standards that correlate events in transverse current with the one in ionic current[61] facilitating the obvious transition.

On the other hand, the use of RTILs opens new avenues in single-molecule sensing since the chemical programming of RTILs based on metal chelate ions can provide means of specific bonding to the bases. This approach is not only restricted to sequencing but also can be extended to amino acids and fingerprinting of short peptides in pores.

Our finding in this chapter paves the way for future rapid and cheap nanopore sequencing. In addition, viscosity gradient system based on RTILs presents novel platform with various interesting novel unexplored research areas in nanofluidics, thermodynamics and kinetics.

3.2. Transport dynamics of biomolecules in nanopores

In nature, translocation of biological molecules through tiny holes formed by transmembrane protein in membranes performs important role for cellular behavior. Therefore, understanding the nature of the translocation process has drawn many attentions in biophysics.

Nanopores offer the possibility of revealing intra-molecular features in biopolymers. When the polymers are driven across the pores by external electric field in a single-molecule manner, we could investigate various key physical properties of a polymer based on this translocation process, such as the scaling behavior, mechanical

properties and polymer collapse. From a typical DNA translocation event, we need to extract the information of how a polymer is translocated through the pore, what is its velocity, what is the role of the interaction with the solvent and pores, and the driving electric field.

Investigation on the translocation dynamics can be realized by compiling the dependence of translocation time on target factors. The dependence of translocation time on DNA length plays a key role in understanding the transport process and scaling behavior of long polymers. The scaling can be attributed to a force balance of viscous drag on self-avoiding walk DNA coil outside the pore and the applied electric force during translocation, which yielded $t \sim L^{2\nu}$, where L is the contour length of the DNA molecule and ν is the Flory exponent. Details of the demonstration can be found in the force balance model adopted by Storm et al.[72]. When studying the length dependence, Storm et al.[72] found that an exponential dependence on DNA length in 10 nm pores, where $t_d \sim L^{1.27}$ (**Figure 3.2 a**). In contrast to large pores, in 4 nm pores, Wanunu et al.[118] showed dsDNA obeys a more complex length scaling. The prominent timescale for short lengths follows a power-law dependence on length, where the power is equal to 1.40. For longer polymer lengths, much stronger power-law dependence emerges: power = 2.3, which might be attributed to additional mechanisms of external DNA interactions with the silicon nitride membrane (**Figure 3.2 b**).

The translocation dynamics can be divided into three distinct stages. Away from the pore, DNA motion is purely diffusive due to the negligible electric field. Within the area of capture radius, DNA is accelerated towards the pore by the electric force, and then one end of DNA finds the pore and starts translocation. In addition to drag forces, since DNA translocation requires threading one end of the polymer into the pore, entropy reduction happens during translocation process. For a self-avoiding polymer of length N , the number of configurational states per volume, accessible to it in the bulk scales as $Z_b(N)$ [119, 120]. Now consider the translocating polymer in a nanopore made in 2D membranes, for which there are n monomers on one side and $N-n$ monomers on the other. Since this situation can be seen as two strands of polymers with one end tethered on the membrane, the number of configurational states of this polymer is given by the product of $Z_w(n)$ and $Z_w(N-n)$, which reaches a minimum

when $n = N/2$. The entropic barrier for the polymer translocation is thus can be written as,

$$\Delta S = \log \frac{Z_b(b)}{Z_w^2(N/2)} \quad (3-1)$$

While the entropic barrier, obtained above from the partition function is an equilibrium property, it states the favorite thermodynamical state is non-translocating, contributing to the entropic part for the free energy. When DNA translocation is governed by an energy barrier, its rate J , according to classical Kramer's theory[121, 122], can be written in the form,

$$J = \omega \exp[(q\Delta V - U) / k_B T] \quad (3-2)$$

where U is the height of the barrier and q is the effective charge of the DNA fragment within the potential gradient area, ΔV is the potential difference and $k_B T$ is the thermal energy.

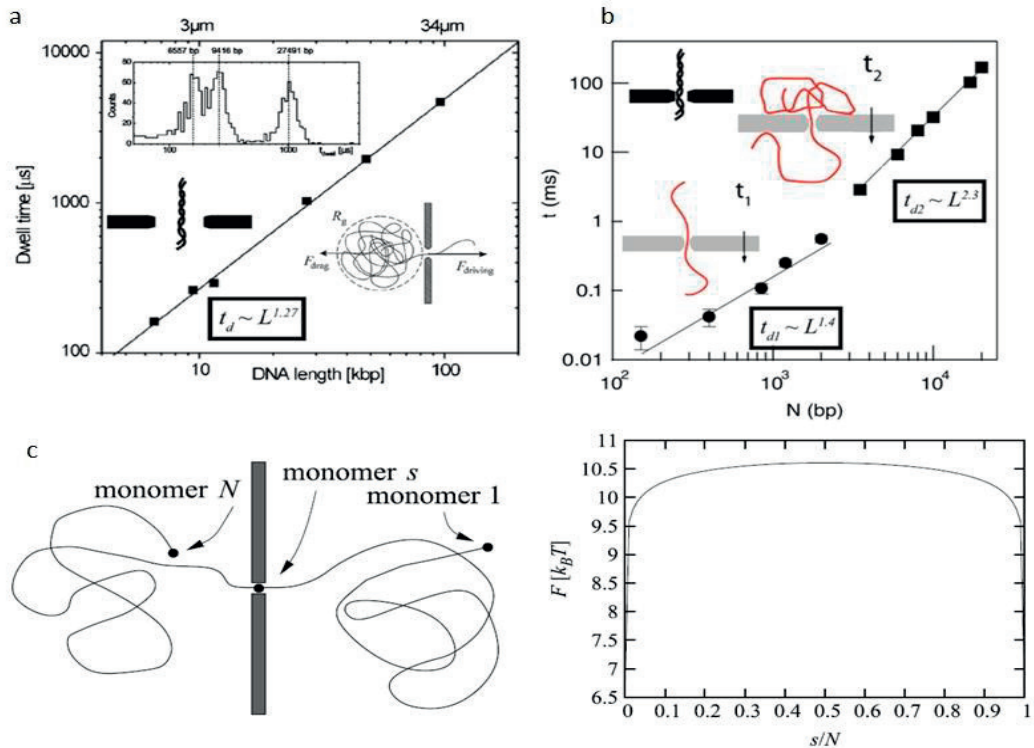


Figure 3.2. Scaling exponents and entropic barrier for biomolecules through nanopore. (a). Translocation time vs. DNA length for dsDNA through a 10 nm SiO₂ pore[12,

72]. Reproduced with permission. **(b)**. Translocation time vs. DNA length for dsDNA through a 4 nm pore[12, 118]. Reproduced with permission. **(c)**. Left: snapshot of a translocating polymer through a 2D nanopore. Right: the quantity $s(t)$ is termed as the reaction co-ordinate borrowed from chemical physics parlance. The reaction co-ordinate $s(t)$ denotes the monomer index located at the pore at time. The entropic barrier as a function of the reaction co-ordinate s/N [120].

3.3. Control of DNA translocation dynamics in nanopore

Various ways to slow down DNA transport velocities have been demonstrated. These methods can be summarized as passive and active controls. Passive control of DNA translocation speed has been achieved by controlling the electrophoresis condition, including temperature, electrolyte, viscosity, pore-DNA interaction and the electrical bias voltage across the nanopore[123-125]. In 2005 Fologea et al added glycerol into buffer to increase the viscosity and consequently reduce the mobility of DNA by 5 times[123]. Kowalczyk et al slowed down DNA translocation 10-fold by manipulating counter-ions binding strength[125]. Numerous reports use either chemical or biological modification of the surface of solid-state nanopore to control the translocation speed via pore translocating molecule interaction. Meller Group has developed the surface charge methods to control DNA translocation dynamics. Recently, they use light to control the surface charge of the pore wall to slow down translocation[124]. Active control by optical tweezers[75, 126], magnetic tweezers[127], atomic force microscope[128] can also manipulate translocation. For an example, Keyser et al, have used optical tweezers for direct force measuring and manipulating DNA in nanopores[75]. One end of the DNA molecule is attached to a micro-meter sized bead, which is then optically trapped in the focus of an infrared laser. Subsequently, they insert individual DNA molecules into a single nanopore and arrest the DNA during voltage-driven translocation by manipulating the bead position. Due to the force balance, the electric force acting on DNA can be measured with high accuracy using the reflected light from the bead. Substantial reductions of the translocation rate can be achieved with processive DNA enzymes, such as DNA polymerase[49], which limit the translocation rate by binding to the DNA strand and preventing it from moving into the narrow confines of the pore faster than the enzyme processing rate for DNA synthesis; or by successive unzipping of DNA oligos,

which then becomes the rate-limiting step for the translocation process[129]. Examples of passive and active control of translocation dynamics are shown in **Figure 3.3**.

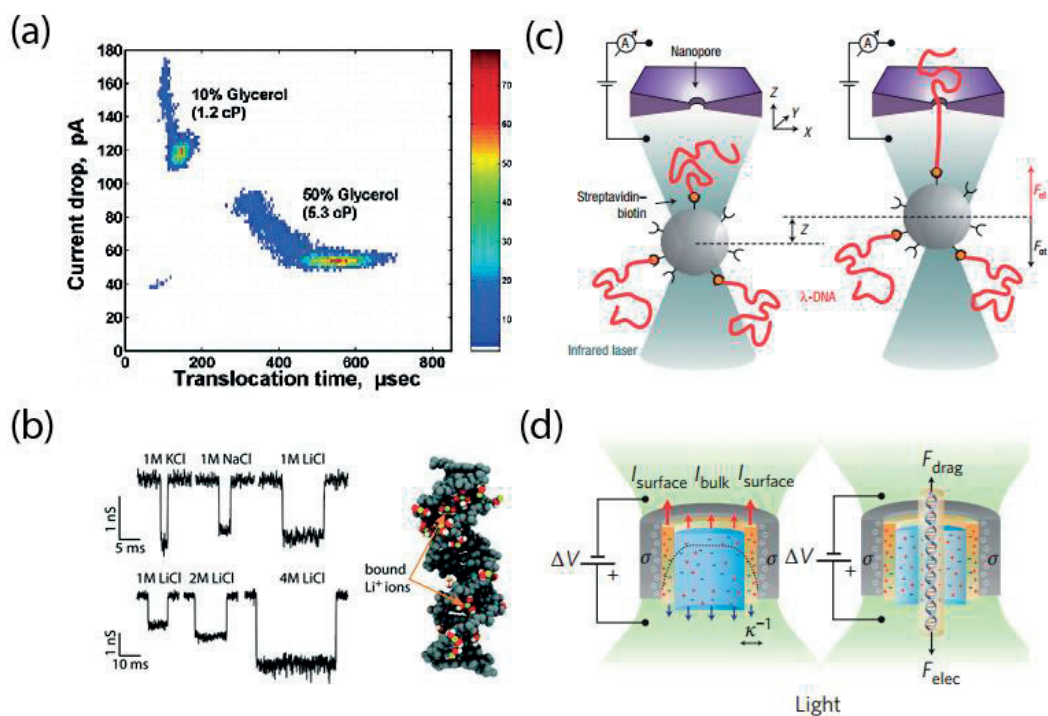


Figure 3.3. Passive and active control of translocation dynamics. **(a)**. Glycerol was added to water to increase the viscosity and decrease the translocation speed[123]. Reprinted with permission from[123]. Copyright (2005) American Chemical Society **(b)**. Slowing down DNA translocation by changing the counter ion bonding[125]. Reprinted with permission from[125]. Copyright (2012) American Chemical Society. **(c)**. Control and manipulation of translocation by optical tweezers (top), which also allows force and position measurement[75]. Figure reproduced with permission. **(d)**. Optoelectronic control of translocation dynamics via light induced regulating of surface charge in nanopore[124]. Figure reproduced with permission.

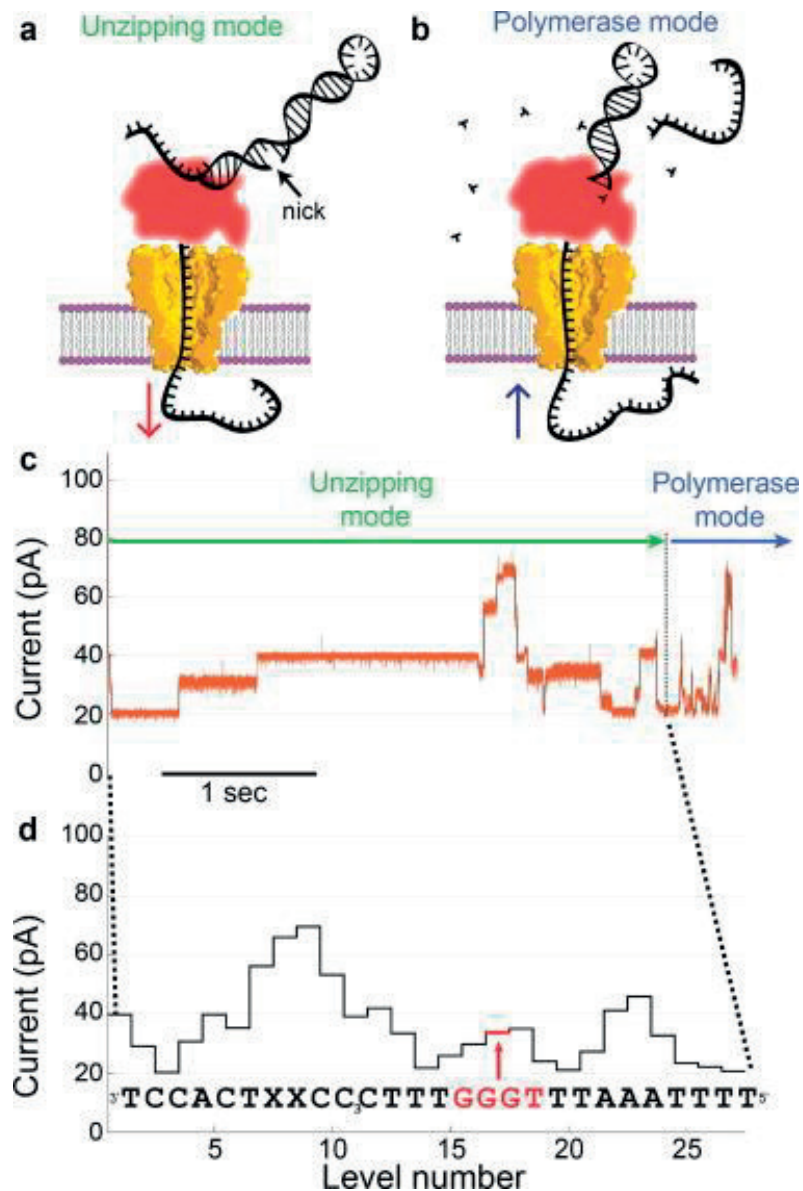


Figure 3.4. Enzyme-based approach to control translocation dynamics for protein nanopore sequencing. **(a).** MspA nanopore sequencing with DNA polymerase. **(b).** Enzyme-controlled DNA motion step leading to distinguished current trace according difference in sequence[47]. Figure reproduced with permission.

We think fast and cheap sequencing would benefit from the enzyme-free and passive approach. To this end, we aim to realize pure physical, solid-state sequencing which will also benefit from the semiconductor fabrication and integration technologies.

3.4. DNA translocation through MoS₂ nanopores

Flux of cations and anions (K^+ , Cl^-) in two directions under the influence of the electrical field through a nanopore, resulting in a constant ionic current, namely the baseline current. A DNA molecule inside the pore will induce the transient blockage in the current baseline, known as DNA translocation.

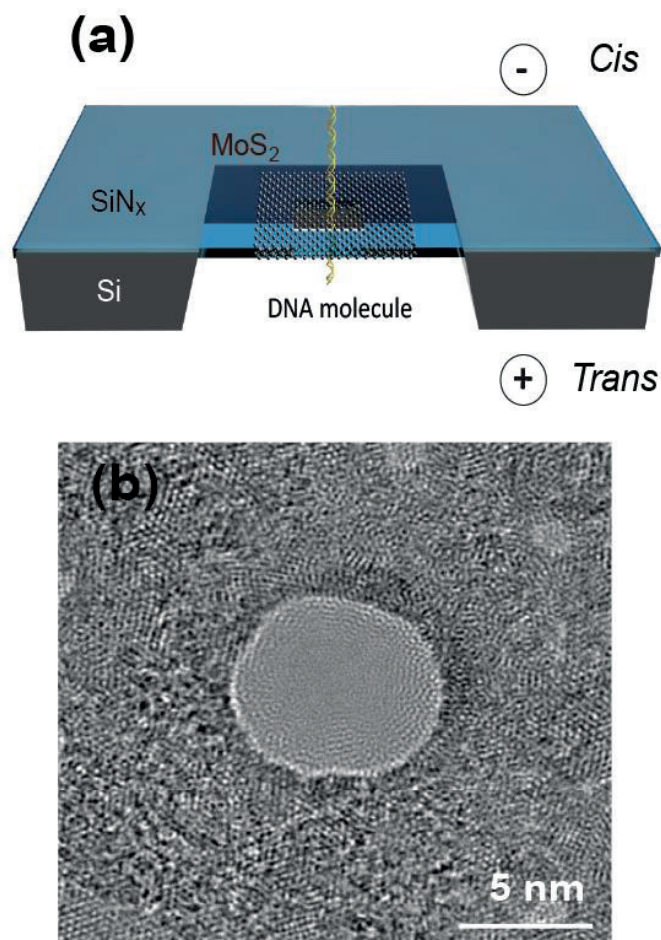


Figure 3.5. Schematics of DNA translocation through MoS₂ nanopores **(a)** and a TEM-drilled 8 nm MoS₂ nanopore **(b)**. DNA translocation will give rise to temporary blockades in ionic pore current manifested by a decrease in ionic current on the time-scale of approximately 100 μ s –10 ms, as shown in **Figure 3.6**. Reprinted with permission from[98]. Copyright (2015) American Chemical Society.

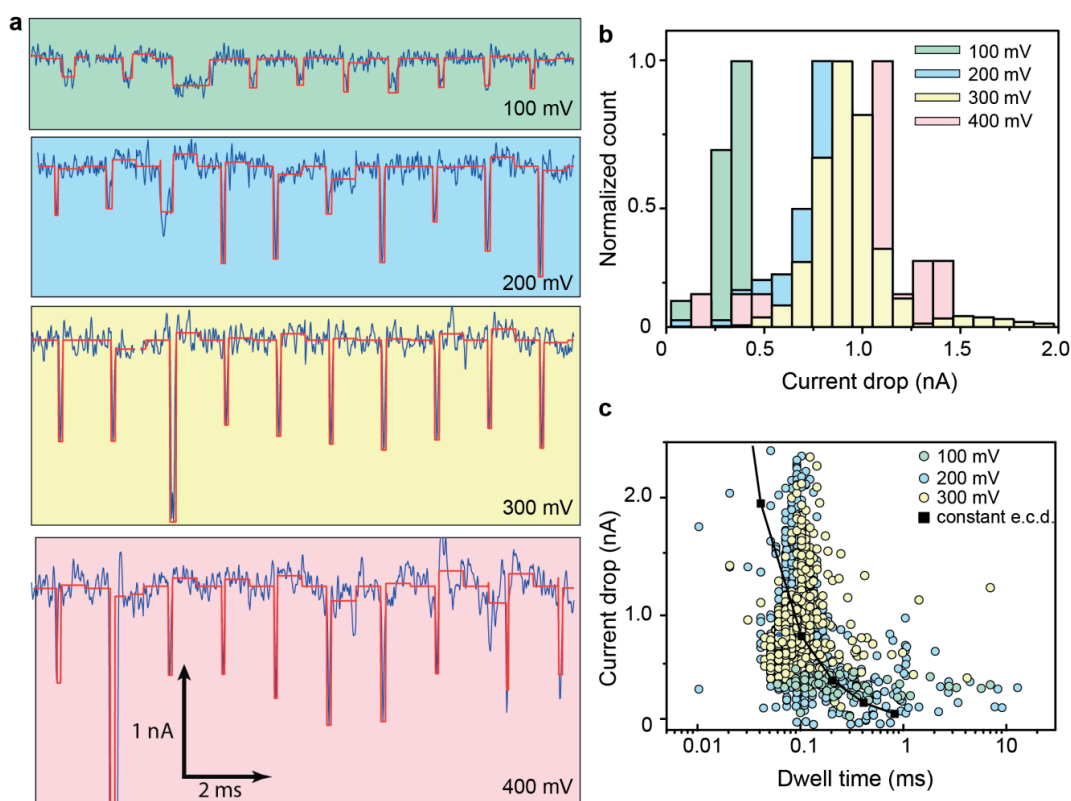


Figure 3.6. DNA translocation through MoS₂ nanopores. **(a)** Concatenated events of pNEB plasmid DNA translocating a 20 nm MoS₂ nanopore in 2 M KCl. Raw signal is in blue and fits are shown in red. Fits are performed using a custom “OpenNanopore” Matlab code[111]. **(b)** Normalized distribution of current amplitude at various voltages. **(c)** Scatter plots of 59, 1823, and 1642 events for 100, 200, and 300 mV, respectively. Events at 400 mV are shown in the next figure in comparison with a 5 nm nanopore in **Figure 3.7**. Each event is represented by its dwell time and current drop. An electron charge deficit (ECD) method is used to fit the area of individual events. Reprinted with permission from[98]. Copyright (2015) American Chemical Society.

We first translocated pNEB plasmid DNA through a 20 nm diameter MoS₂ nanopore to eliminate the multiple DNA conformation issues. Two parameters, the amplitude of blockage and dwell time are used to quantify individual translocation events. In our group, we developed a so-called cumulative sums (CUSUM) algorithm to detect events automatically[111] and extract abovementioned parameters for each event. Events are concatenated with short segments of the baseline signal preceding and following them. Due to the circular shape of the pNEB plasmid, all events have only

one level indicating a single conformation. The signal amplitude also increases linearly with the applied voltage as shown in **Figure 3.6 b**. Here, we used $(2.2/d)^2$ to calculate theoretical blockage, where $d = 20$ nm in this case. Blockage percentage is 1.5%, in accordance with the theoretical value of 1.2%. Scatter plots are used to describe the statistics of DNA translocation as shown in **Figure 3.6 c**. For voltages above 200 mV, fast translocation is observed with a most probable dwell time of ~ 100 μ s[130]. But for 100 mV, a much broader distribution (200 μ s full-width at half-maximum) is observed with a mean dwell time of ~ 300 μ s, which is consistent with published results in graphene nanopores using DNA molecules of similar length [35-37, 50]. More insight can be gained by using a constant electron charge deficit (ECD) method[131] to fit the scatter plot (**Figure 3.6 c**) for various voltages. As a result, a value of ~ 500 ke is obtained, which is at least five times of previously reported data for 3 kbp DNA[132]. This increase is mainly due to the increased blockage amplitude because of the greatly improved sensitivity of MoS₂ nanopores compared to conventional Si₃N₄ nanopores. Slaven et al. also reported from two-fold up to ten-fold enhancement in signal for DNA translocation in graphene nanopores [35, 50]. Therefore, we conclude that MoS₂ and graphene nanopores have comparable sensitivities. It is very important to have a good signal to noise ratio (SNR), preferably more than 6, for event detection. Here, we obtain SNR > 10 (100 pA RMS noise and \sim nA signal). The percentage of device failure (too high or too low conductance) in solution is surprisingly low ($< 30\%$). A very important feature of MoS₂ membranes when compared to graphene ones is that undesirable adsorption of DNA onto surface is eliminated here, while many additional surface treatments were needed in order to reduce the strong interaction between DNA and graphene [35-37, 50].

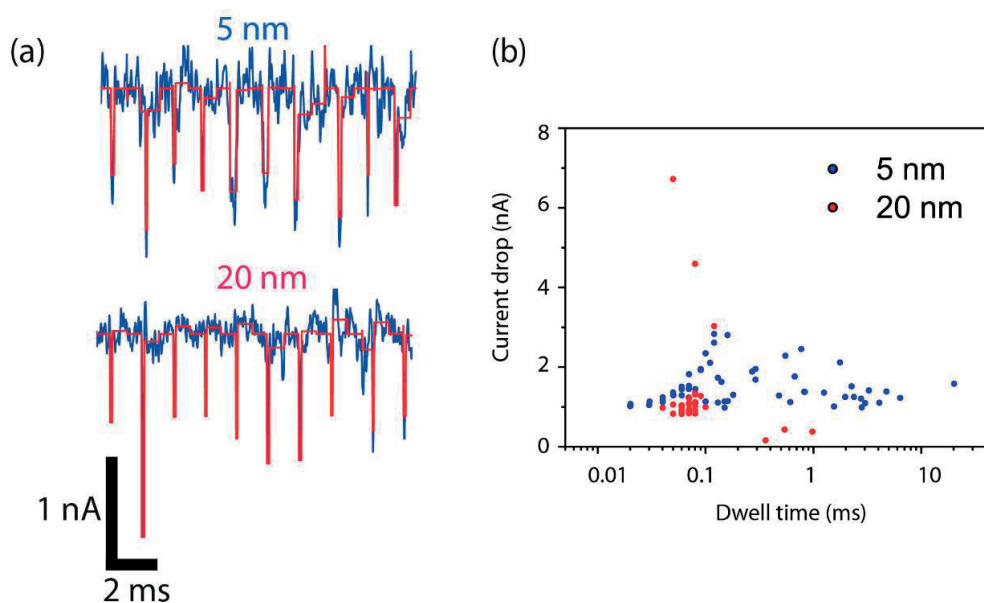


Figure 3.7. (a) Concatenated events of pNEB translocation in 5 nm and 20 nm MoS₂ nanopores. Recorded at 400 mV in 2 M KCl. (b) Scatter plot of events. Reprinted with permission from[98]. Copyright (2015) American Chemical Society.

In order to gain more understanding on the interaction between MoS₂ and DNA, we translocated pNEB DNA through a 5 nm diameter MoS₂ pore. Representative concatenated traces are shown in **Figure 3.7 a**, where the same experimental conditions were used except pore diameter which was 5 nm. From the scatter plot in **Figure 3.7 b**, both mean current amplitude and mean dwell time are larger for the 5 nm pore compared to the 20 nm pore, implying a local interaction between the edge of the MoS₂ pore and the DNA molecule. To extend this statement, this interaction happens only when DNA is sliding through the edge of pore with the effect of retarding DNA translocation. For larger pores (20 nm), translocations tend to be in a free manner.

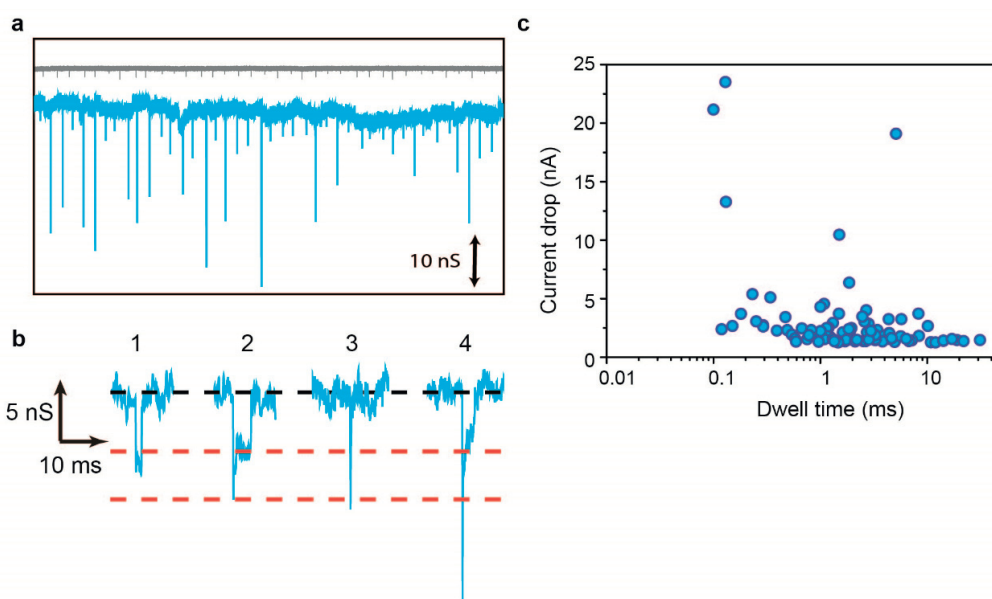


Figure 3.8. (a) A representative trace (in blue) of lambda DNA translocation through a 20 nm MoS₂ nanopore in 2 M KCl under a 200 mV bias voltage. The upper trace (in black) is an example of lambda DNA translocation through a SiN_x nanopore. (b) Selected individual events with quantized current drops implying multiple conformations of lambda-DNA within the nanopore, i. e., unfolded (1), partially folded (2), folded (3) and bumping event (4). (c) Scatter plot of 104 events. Each event is represented by its dwell time and current blockage. Events statistics are collected from two devices. Reprinted with permission from [98]. Copyright (2015) American Chemical Society.

As first seen using solid-state nanopores, DNA conformations can be revealed using the quantization of current blockage when DNA translocates through a nanopore [32]. Here, we used lambda DNA, which has a wealth of secondary structures and conformations, to test the performance of MoS₂ pore in distinguishing between them by ionic current measurements. **Figure 3.8 a** shows two typical current vs. time traces for DNA translocation through SiN_x and MoS₂ pores, where much bigger current dips are clearly visible for MoS₂ pores showing greater SNR. After careful inspection of the events, we selected four events to illustrate major conformations occurring during DNA translocation. Specifically, in **Figure 3.8 b**, the event 1 has a conductance drop of ~5 nS, which is attributed to the translocation in an unfolded or linear manner. It is worth noting that a five-fold enhancement in signal amplitude is observed compared

to the typical conductance drop of ~ 1 nS in Si₃N₄ platforms. For the event 2, DNA enters the pore in a folded manner manifested by a conductance drop of ~ 10 nS and then translocates in an unfolded manner with a conductance drop of ~ 5 nS. For the event 3, DNA is in a folded manner during the whole translocation manifested by a conductance drop of ~ 10 nS. Sometimes, we saw very deep current dips in the very beginning of an event, indicating a “bumping” of DNA onto the orifice of the pore in a coiled form (event 4 in **Figure 3.8 b**). After entering the pore, the DNA molecule is stretched under electric field and it results in a conductance drop of ~ 5 nS. The statistics of these events are presented using scatter plot in **Figure 3.8 c**. Moreover, a mean dwell time of ~ 1 ms can be obtained, which is larger than that of shorter pNEB and is expected for longer -DNA.

As for graphene nanopores, no significant slowing down can be achieved even with small-diameter pores (~ 2 nm). The velocity of DNA translocation is ~ 20 ns/bp, still beyond the present amplification bandwidth of 4 MHz for translocation experiments. Although the enhancement of signal amplitude is dramatic in MoS₂ pore, the lack of temporal resolution is the major obstacle that should be overcome for wider applications.

3.5. Room-temperature ionic liquids as DNA solvent

Room-temperature ionic liquids (ILs) are being explored as environmentally green solvents for organic synthesis and catalysis[133, 134]. In addition, with their tunable structures, tailored physicochemical properties, and wide electrochemical window, ILs are becoming a new class of functional materials for application in electrochemistry, synthetic chemistry, phase transfer catalysis, and polymerization. Tunable viscosity is a typical characteristic for tailored physicochemical properties of ILs. By designing different molecular structures, the viscosity can be modulated between 10-1000 cP. As alternatives to conventional organic solvents, ionic liquids improve the selectivity and yield in bioprocesses. ILs could also be exploited for the extraction of biomolecules including proteins and DNA[135]. Wang et al. showed the extraction of double-stranded DNA using the IL (BminPF₆)[136]. The extraction efficiency of DNA was increased when the length of an alkyl chain on the imidazolium cation was increased due to the hydrophobic interactions. The use of ILs

for the extraction of DNA avoids the use of the existing phenol/chloroform method and circumvents the denaturation of DNA. Further use of ILs in the extraction of proteins has been reported[137]. Moreover, IL is an ideal electrolyte for electrochemical and electrical applications benefiting from the wide electrochemical window. Therefore, a higher tunable bias can be applied for the electrophoretic process of DNA across nanopore. Various properties of ILs are shown in **Figure 3.9**.

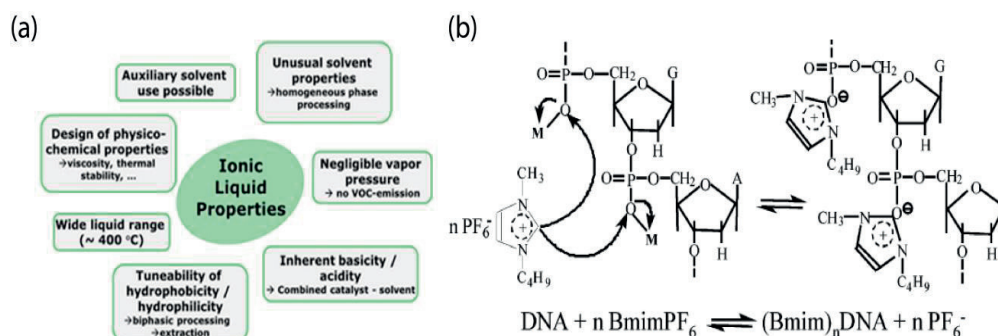


Figure 3.9. Ionic liquids properties and interactions with DNA. (a). Abundant properties of ionic liquids due to the programmable chemical structure[138]. (B). Electrostatic interaction between DNA and BMIM[136]. Reprinted with permission from[136]. Copyright (2007) American Chemical Society.

3.6. Slowing down DNA translocation with viscosity gradient

3.6.1. Viscosity gradient system based on RTILs in MoS₂ nanopores

We have used a combination of atomically thin MoS₂ nanopores and an ionic liquid/water viscosity gradient system that allows molecular translocation speeds to be decreased by two to three orders of magnitude. Our approach to slowing down translocation has been inspired by the remarkable physical and chemical properties of room-temperature ionic liquids (RTILs): non-aqueous electrolytes composed of a pair of organic cations and anions. RTILs offer a high degree of freedom in fine-tuning their structure, which allows their physical and chemical properties to be tailored for a given application[139]. We chose 1-butyl-3-methylimidazolium hexafluorophosphate (BmimPF₆), since it has a broad viscosity window of 10-400 cP[140], which can be tuned to optimize the temporal resolution. Tunability can be obtained either by varying the temperature (20-50 °C) or by mixing BmimPF₆ and BmimPF₄ in different

Chapter 3. Nucleotide structures probed by MoS₂ nanopores

ratios[141]. BmimPF₆ is also a friendly solvent for biomolecules and, most importantly, it exhibits a good ionic conductivity of 1.4 mS cm⁻¹ [140]. It has also been widely used as an electrolyte, with a wide electrochemical window[135]. Previous related attempts to slow DNA translocation speeds used glycerol, which has a low conductivity and limited the approach to a narrow viscosity window (1.2-5 cP)[123]. Consequently, only modest improvements in DNA translocation speed were achieved (3000 nt/ms)[123].

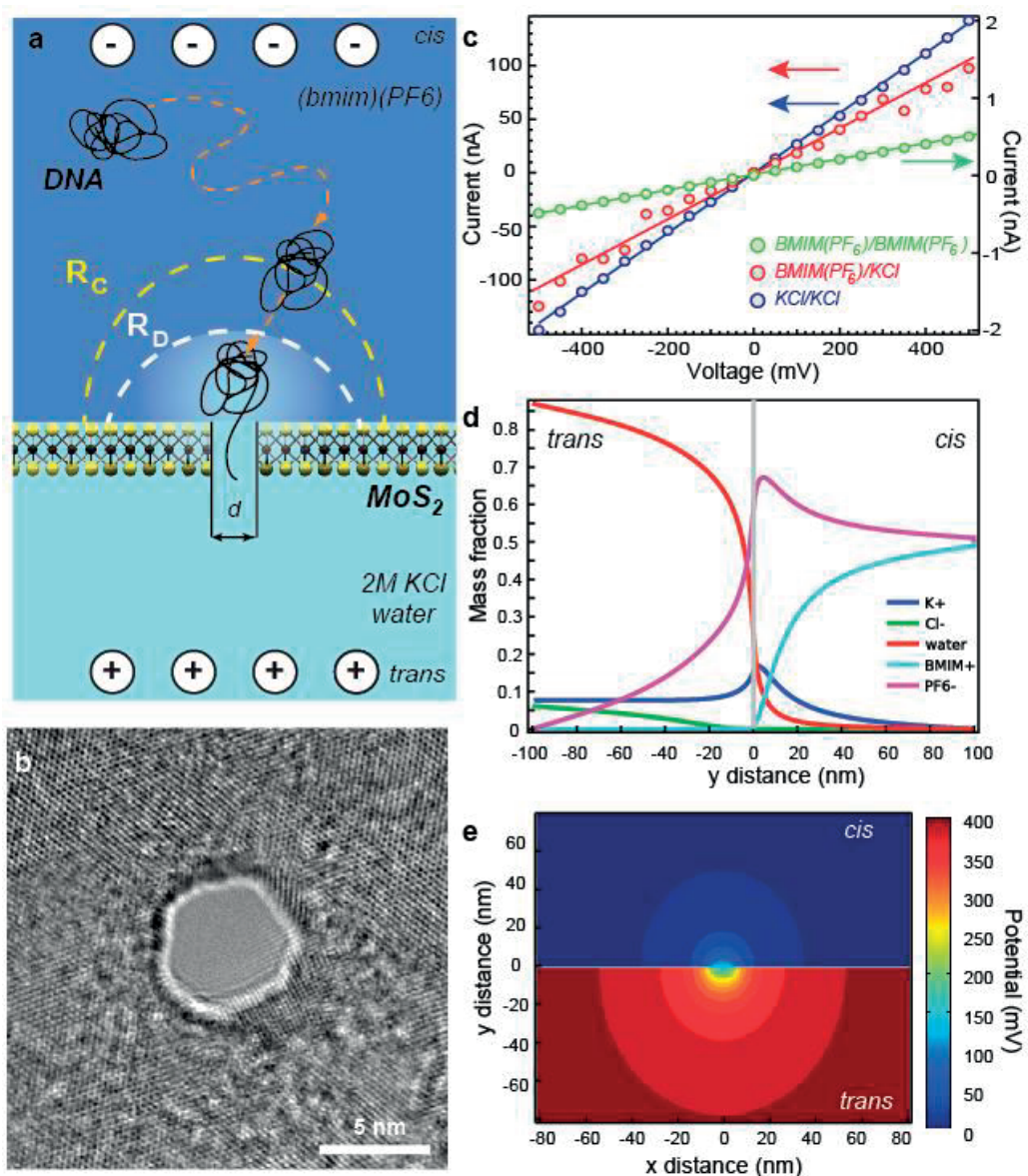


Figure 3.10. Schematic and characterization of the RTILs/ KCl viscosity gradient system in MoS₂ nanopores. (a) *Cis* chamber contains RTILs (BmimPF₆) while *trans*

chamber contains 2 M aqueous KCl solution. The two chambers are separated by a monolayer MoS₂ membrane with a nanopore. Schematic also displays dynamics of DNA translocation through a monolayer MoS₂ nanopore. Away from the pore, DNA motion is purely diffusive due to the negligible electric field, but once within the area of capture radius R_c , DNA will be accelerated towards the pore by the force due to electrophoretic and electroosmotic effects. A part of DNA will undergo conformational change and one end will dive into the pore. The non-translocated part of the DNA polymer -monomers will keep the coil conformation and experience a strong Stokes dragging force from the ionic liquids. Consequently, DNA translocation through the pore can be significantly slowed down. **(b)** Bright-field TEM image of a 5 nm solid-state pore fabricated in a monolayer MoS₂ membrane suspended over a 200 nm × 200 nm etched area formed in the center of a 20 μm large low-stress SiN_x membrane with a thickness of being 20 nm. **(c)** Ohmic current–voltage responses of a 17 ± 2 nm MoS₂ pore. IV characteristics are taken at room temperature in a 2 M aqueous KCl solution (blue circles), pure BmimPF₆ (green circles) and in BmimPF₆/2 M KCl gradient (red circles) **(d)** Mass fraction of water, anions (PF₆⁻ and Cl⁻), cations (Bmim⁺ and K⁺) as a function of distance from the nanopore (note that the calculation has been performed at -400 mV) **(e)** Electric potential map evaluated numerically for the viscosity gradient system shown in **(a)**. Figure reproduced from Nature publication[142].

With our viscosity gradient system, schematically shown on **Figure 3.10 a**, it was possible to employ pure BmimPF₆ without compromising the conductance of the MoS₂ nanopore. In pure RTILs, the conductance of even a large nanopore (with a diameter of 17 ± 2 nm) is relatively low (~1 nS), in agreement with previous report[143], when compared to KCl (a conduction of 280 nS is measured in 2 M KCl/2 M KCl) (**Figure 3.10 c**). Inspired by the use of concentration gradient systems in nanopores, we created a viscosity and concentration gradient system that offers a conductivity of 210 nS. The *cis* chamber in our system contains RTILs (BmimPF₆), while the *trans* chamber contains 2 M aqueous KCl solution. It is important to note that here we use two types of solvents with completely different physicochemical properties and that in the region inside and close to the pore we have in fact a non-homogeneous phase solution.

Chapter 3. Nucleotide structures probed by MoS₂ nanopores

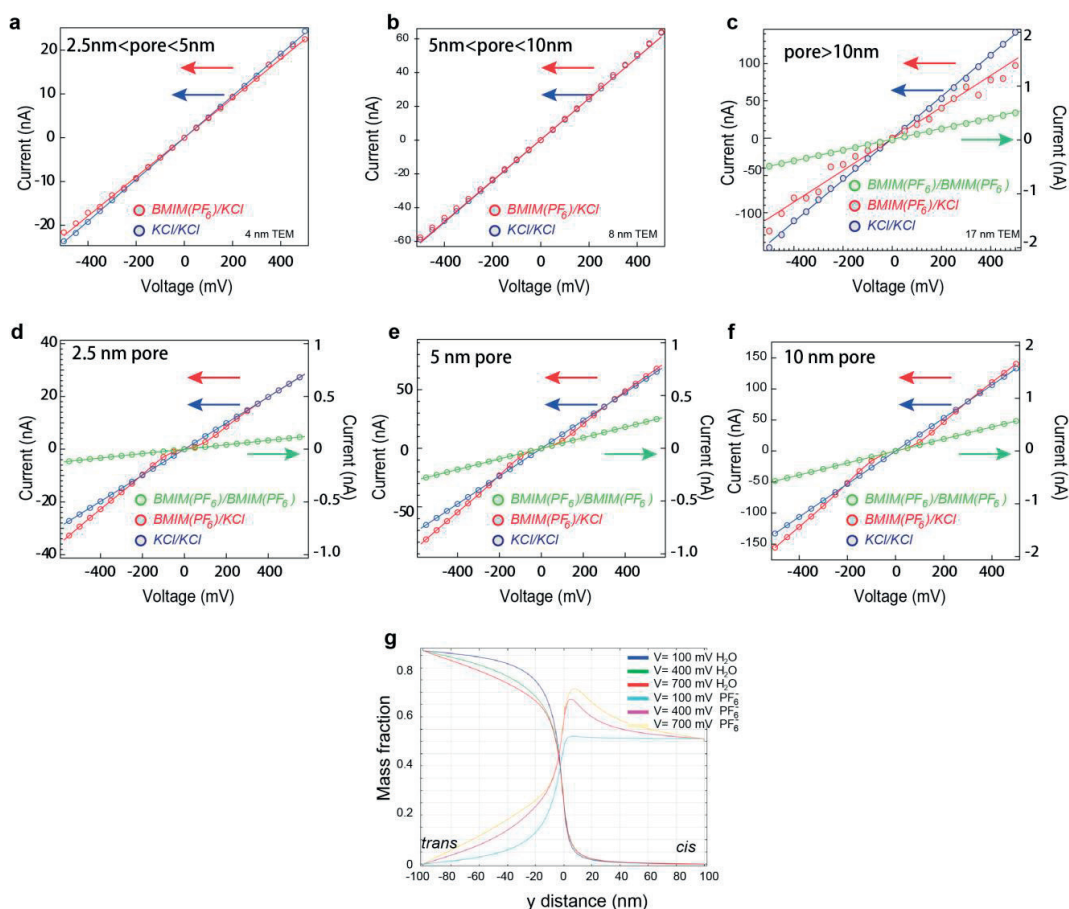


Figure 3.11. Current-voltage characteristics of MoS₂ nanopores and COMSOL simulations of the ionic transport through a MoS₂ nanopore. Measured current-voltage characteristics for viscosity gradient system (red), pure ionic liquid (green) and 2 M aqueous KCl solution (blue) (a) in a pore smaller than 5 nm (b), pore with a diameter between 5 nm and 10 nm (c) pore larger than 10 nm. Simulated current-voltage characteristics for a viscosity gradient system (red), pure ionic liquid (green) and 2 M aqueous KCl solution (blue) in 2.5 nm pore having a conductance in gradient conditions of ~ 48 nS (d), 5 nm pore having conductance in gradient conditions of ~ 120 nS (e), and 10 nm pore having conductance in gradient conditions of ~ 280 nS (f). (g) Mass fraction as a function of distance from the nanopore center (marked as 0) of water, anions (PF₆⁻ and Cl⁻), cations (Bmim⁺ and K⁺) at different applied voltages. Figure reproduced from Nature publication[142].

To gain insight into the ionic transport through the nanopores in the presence of an inhomogeneous phase solution, we performed finite element analysis by solving the

Poisson-Nernst-Planck (PNP) equation. **Figure 3.10 d** shows the mass fraction of water molecules, anions and cations as a function of distance from the nanopore at a transmembrane bias voltage of 400 mV. The sub-nanometer membrane thickness ensured that a relatively high number of water molecules diffused from the trans into the cis chamber. Similarly, anions and cations diffused into their respective chambers. Modelled conductances for 2.5 nm, 5 nm 10 nm pore, shown in **Figure 3.11 d-f**, are in good agreement with our measurements (**Figure 3.11 a-c**). Interestingly, the mass fraction of water molecules in the cis chamber shows a weak dependence on the transmembrane bias, while PF_6^- diffusion is strongly affected (**Figure 3.11 g**).

3.6.2. Slowing down DNA translocation with viscosity gradient system

Having successfully built and characterized our viscosity gradient system, we performed our first translocation experiment by adding 48.5 kbp λ -dsDNA to the *cis* chamber filled with BmimPF₆. In order to minimize the contribution from the nanopore-DNA interaction that can also significantly slow down DNA translocation[82], we decided to first use MoS₂ nanopores with relatively large diameters (~20 nm). **Figure 3.12 a** displays the typical current trace recorded during the translocation of the λ -DNA molecule in the viscosity gradient system in the presence of a transmembrane bias voltage of 400 mV. When compared to a typical current trace acquired in a 2 M aqueous KCl solution obtained using the same pore and transmembrane voltage, one can observe temporal improvement and no reduction in the amplitude of the current drop. Unlike other viscous systems for slowing down DNA translocation, signal amplitude has been preserved owing to the conductive nature of RTILs and high concentration of chloride ions inside the pore. The average translocation time is 130 ms for λ -DNA in the viscosity gradient system, and 1.4 ms in the 2 M KCl solution presenting two orders of magnitude's improvement.

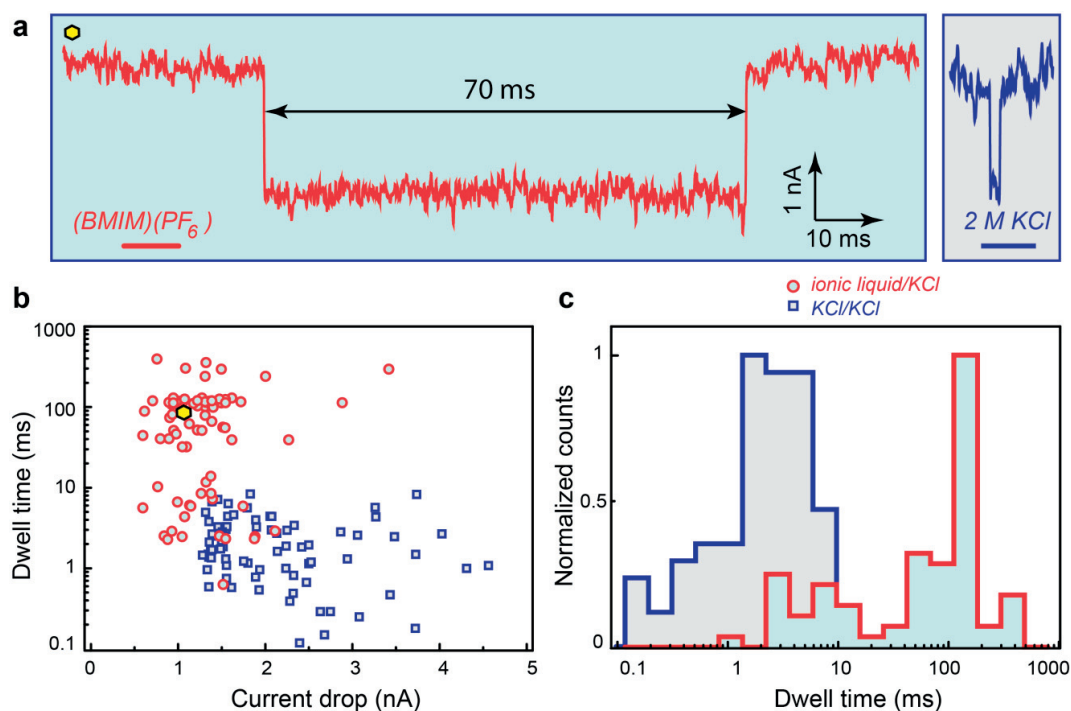


Figure 3.12. Slowing down DNA translocation. **(a)** An example of a 48.5 kbp λ -dsDNA translocation event in a viscosity gradient system. The corresponding current drop represents a single DNA molecule passing through the MoS₂ pore with a diameter of 20 nm. On the right, we show a typical translocation trace for 48.5 kbp λ -dsDNA obtained using the same nanopore in the absence of the viscosity gradient, resulting in translocation times that are two orders of magnitude shorter. (Displayed traces down-sampled to 10 kHz) **(b)** Scatter plots (blockade current versus dwell time) for dwell time versus current signal of λ -dsDNA translocation in water (blue squares), and in our viscosity gradient system (red circles) obtained using the same 20 nm diameter MoS₂ nanopore. Yellow hexagon indicates the position of the event shown in **(a)** in respect to other events displayed in **(b)** **(c)** Histograms of translocation times corresponding to the translocation of λ -dsDNA in water (blue) and the viscosity gradient system (red). Figure reproduced from Nature publication[142].

At this point, in the absence of the electro-osmotic flow (EOF) and charge reduction for a given pore, DNA molecule and bias voltage, we can introduce the retardation factor r on translocation time. We obtain a retardation factor higher than 100 that is predominantly due to the increase in the viscosity in our viscosity gradient system. However, scatter plots and DNA translocation histograms in **Figure 3.12 b** and

Figure 3.12 c reveal a large spread in dwell times that can be attributed to several factors associated with the viscosity gradient system. In reality, EOF, charge reduction as well as long-range hydrodynamic effects and the existence of gradients in the free-energy landscape have to be included in the future model and could result in a more complex dynamics of DNA translocation in the viscosity gradient system than assumed in our simplistic force balance model showing the viscosity relation. In addition, it is possible that we have overestimated the value of BmimPF₆ viscosity in the vicinity of the pore. More accurate calculation of the retardation factor should include the effects related to charge reduction and the presence of the EOF[144]. Due to the negative charges at the surface of MoS₂ membrane and within the pore, the direction of EOF is opposite to the direction of DNA translocations and could result in further slowing down. By comparing translocation traces before, during and after translocation events we see that they all have a similar noise level of 520-540 pA. We observe a slight increase of noise during the translocation that can be explained by the fact that DNA interacts strongly with BmimPF₆ via electrostatic interaction between the cationic Bmim⁺ groups and DNA phosphates (P-O bonds)[145]. Because of this electrostatic interaction and the hydrophobic association between Bmim⁺ and bases, DNA molecules can act as carriers for Bmim⁺ ions from the *cis* to the *trans* chamber.

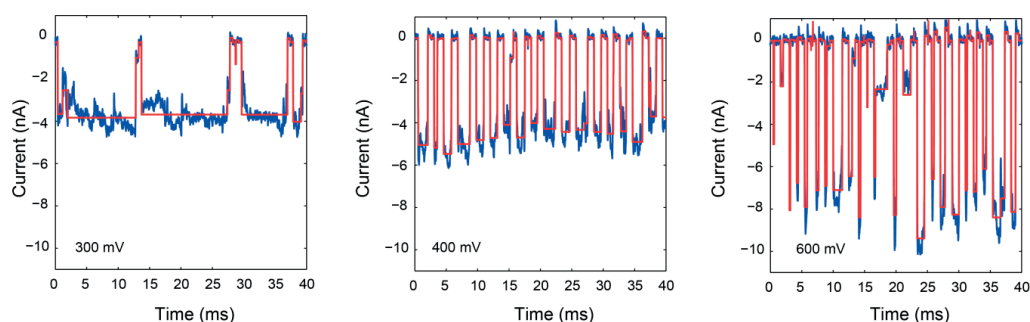


Figure 3.13. Example traces of pNEB translocation traces through a MoS₂ pore under ionic liquid/KCl condition with variable voltages (data used for **Figure 3.14**). The most probable dwell times, from a single-exponential fit, are 5.5 ± 0.2 ms, 2.2 ± 0.5 ms, and 0.5 ± 0.1 ms for 300 mV, 400 mV, and 600 mV, respectively. This also shows a linear relationship between the current signal and applied voltage except at 500 mV (due to baseline fluctuation). We also observed enhanced signal under viscosity gradient conditions. Figure reproduced from Nature publication[142].

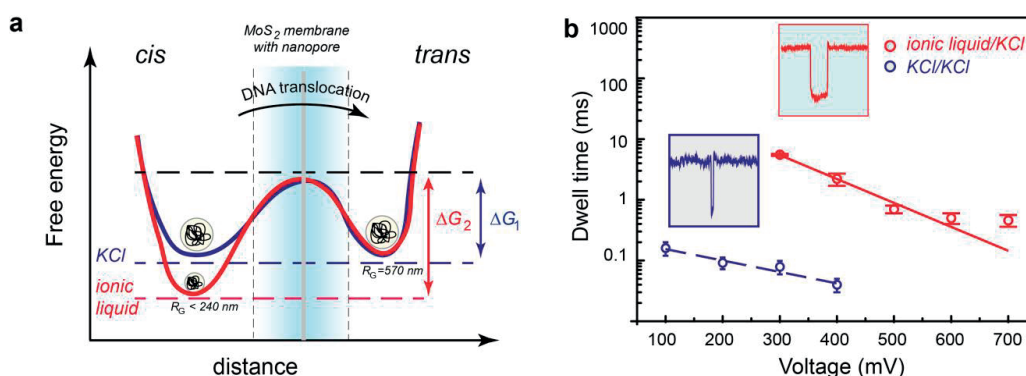


Figure 3.14. Single molecule DNA translocation through a nanopore probes the dynamics of Kramer's theory **(a)** Schematic representations of single-well free-energy surfaces, for two conditions. The schematics describes the intrinsic (i.e. zero voltage) free-energy surface with a well and a barrier to translocation. In the context of the voltage-driven translocation of individual DNA molecules in a nanopore, the well of the free-energy surface corresponds to the random-coil DNA configuration in a cis chamber with corresponding radius of gyration, while escape over the barrier involves translocation through the nanopore and subsequent adoption of the random-coil conformation. The free energy should include at least two parts, one from the phase transfer as described using L-J equation, another from the entropy part of the DNA coil. Both of these two energy parts give a similar phase as drawn, with the only significant difference being the distance and the free-energy level. **(b)** Dependence of the translocation dwell time on the applied voltage for pNEB DNA in ionic liquid/KCl solution (red) and in KCl/KCl (blue). For both conditions, we observe an exponential dependence that reveals that translocation is voltage-activated. Blue and red lines are exponential fits to the data. Figure reproduced from Nature publication[142].

In general, the single-molecule DNA translocation process can be viewed as a voltage-driven barrier crossing as shown in **Figure 3.14**. To further explain retardation mechanism, we explore the voltage dependence of pNEB 193 (2700 bp long DNA plasmid) translocation dwell times in the MoS₂ nanopore (**Figure 3.13**). The observed power law scaling is consistent with Kramer's theory (**Figure 3.14**). A free-energy barrier predominately arises from the RTILs and KCl/water interface and includes the change in conformational entropy of the translocating polymer. The threading process across nanopore in a high-voltage regime follows a force balance

model considering the balance of drag force and electric force. pNEB is almost 18 times shorter than lambda-DNA, however we still observe large retardation when comparing average dwell times recorded at 400 mV, under the condition of viscosity gradient 2 ± 0.5 ms, and 40 ± 10 μ s in the 2 M KCl aqueous solution.

3.7. Identification of single nucleotides

3.7.1. Differentiation of 30-mer DNA homopolymer

To exploit the full potential of our viscosity gradient system, we translocate short homopolymers, poly(dA)₃₀, poly(dT)₃₀, poly(dG)₃₀ and poly(dC)₃₀, through a 2.8 nm diameter pore in single-layer MoS₂. DNA-pore interactions can also increase the translocation time by one order of magnitude [118].

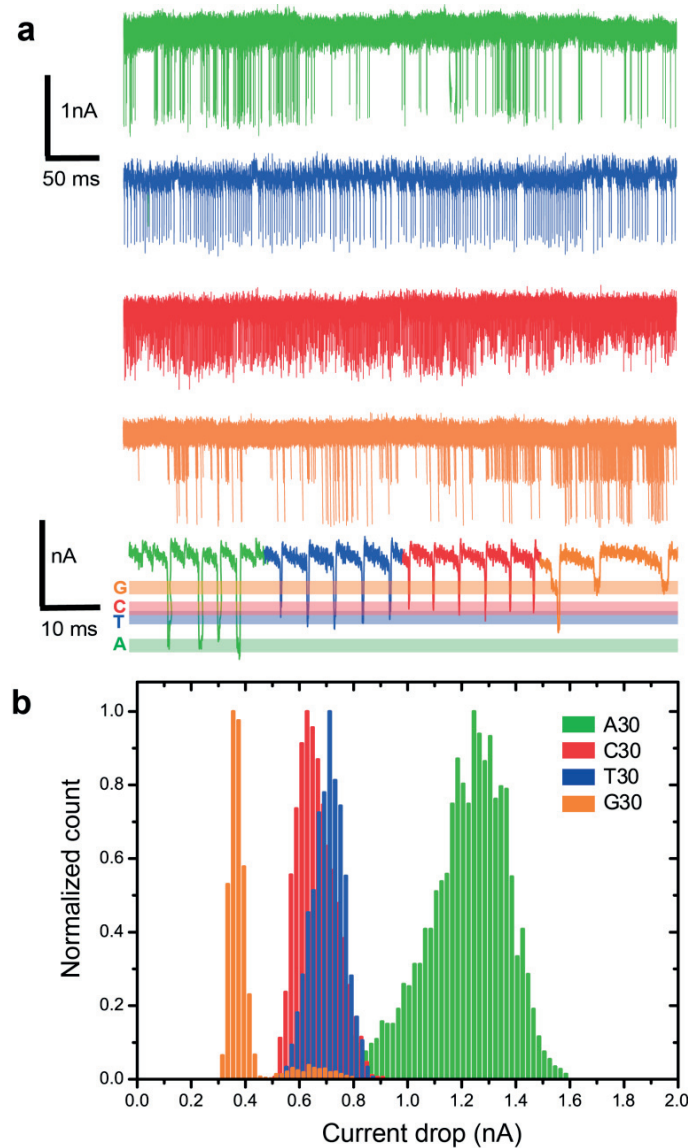


Figure 3.15. Differentiation of 30mer oligonucleotides in the MoS₂ nanopore. **(a)** 0.5 s and 0.1 s translocation signals for each homopolymer, poly A30 (green), poly C30 (red), poly T30 (blue) and poly G30 (orange). **(b)** Normalized histogram of current drops for each kind of the DNA homopolymer. The mean value for poly A30 is 1.25 ± 0.12 nA, for poly C30 is 0.64 ± 0.07 nA, for poly T30 is 0.71 ± 0.06 nA and for poly G30 is 0.36 ± 0.03 nA. Data acquired in pure RTIL *cis* chamber, 100 mM KCl, 25 mM Tris HCl, pH 7.5, *trans* chamber, at +200 mV. The concentration of short DNA homopolymers in RTILs is 0.02 $\mu\text{mol/ml}$. Figure reproduced from Nature publication[142].

The 2.8 nm pore in single-layer MoS₂ membrane suspended over smaller opening in the nitride, even without any special pretreatment[55], displays better noise properties with a current RMS of 59 pA at 0 mV and 89 pA at 200 mV, compared to the pores suspended over larger openings (> 300 nm). The noise reduction is achieved by restricting the opening for freestanding MoS₂ membrane to the hole having 100 nm diameter[50]. Self-organization of certain ionic liquids can be further exploited to reduce 1/f noise in single nanopores as shown by Tessarit et al.[146]. **Figure 3.15 a** shows translocation traces of short DNA homopolymers for periods of 0.5 s and 0.1 s respectively. Four peaks can be clearly distinguished in the histogram of current drops shown in **Figure 3.15 b**.

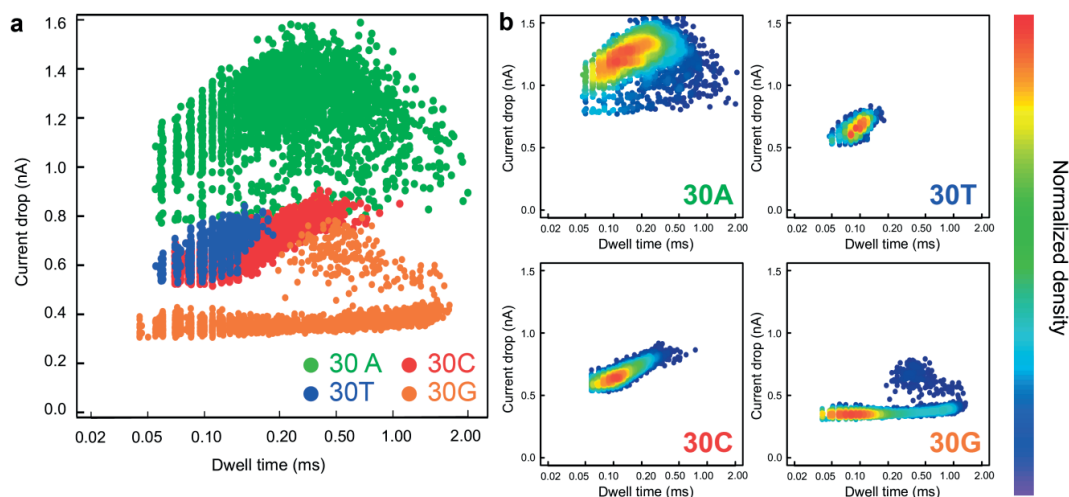


Figure 3.16. (a) Scatter plots of nucleotide translocation, showing distinguished current drops and dwell times for poly A30 (green), poly C30 (red), poly T30 (blue), and poly G30 (orange). Normalized histogram of current drops for each kind of the DNA homopolymer. The mean value for poly A30 is 1.25 nA, for poly C30 is 0.65 nA, for poly T30 is 0.7 nA and for poly G30 is 0.45 nA. (b) Density plots of 30mer oligonucleotides in a MoS₂ nanopore; for poly A30, the position of the hot spot is (0.15, 1.25), for poly T30, (0.1, 0.75), for poly C30, (0.12, 0.65) and for poly G30 (0.09, 0.45). The color-map on the right shows the normalized density distribution of events. Data acquired for an experimental condition of pure RTIL in the *cis* chamber and 100 mM KCl, 25 mM Tris HCl, pH 7.5 in the *trans* chamber. The bias is +200 mV. The concentration of short DNA homopolymers in RTILs is 0.02 μ mol/ml. Figure reproduced from Nature publication[142].

The density scatter plots shown in **Figure 3.16** are useful in revealing the range of the most probable dwell time for the four types of poly-nucleotides at the transmembrane bias voltage of 200 mV. The current traces and histogram of poly(dG)₃₀ homopolymer display two peaks. However, from the poly(dG)₃₀ density scatter plot one can easily identify which peak is more probable. Based on the amplitude and temporal signature of the second peak, we believe that it might originate from the G-quadruplex formation[147]. Venta et al. reported a much faster translocation (20 μs) of such homopolymers using a 1 M Hz amplifier in 1.5 nm pores with high applied voltage (1 V)[82]. However, high bandwidth amplifier introduced additional noise and high voltage might reduce the lifetime of the device. In the viscosity gradient system and 2.8 nm pore, we achieved 10-50 times slowing down compared to the results from Venta et al[82].

3.7.2. Identification of single nucleotides

Finally, using the same 2.8 nm diameter MoS₂ nanopore, we translocate single nucleotides, dAMP, dTMP, dGMP and dCMP. The exceptional durability of the MoS₂ nanopore has allowed us to perform 8 consecutive experiments with high throughput (more than 10000 events collected, enabling robust statistical analysis) (**Figure 3.16** and **Figure 3.18**) in the same pore. **Figure 3.17** shows translocation traces of four single nucleotides for periods of 0.5 s and 0.1 s respectively.

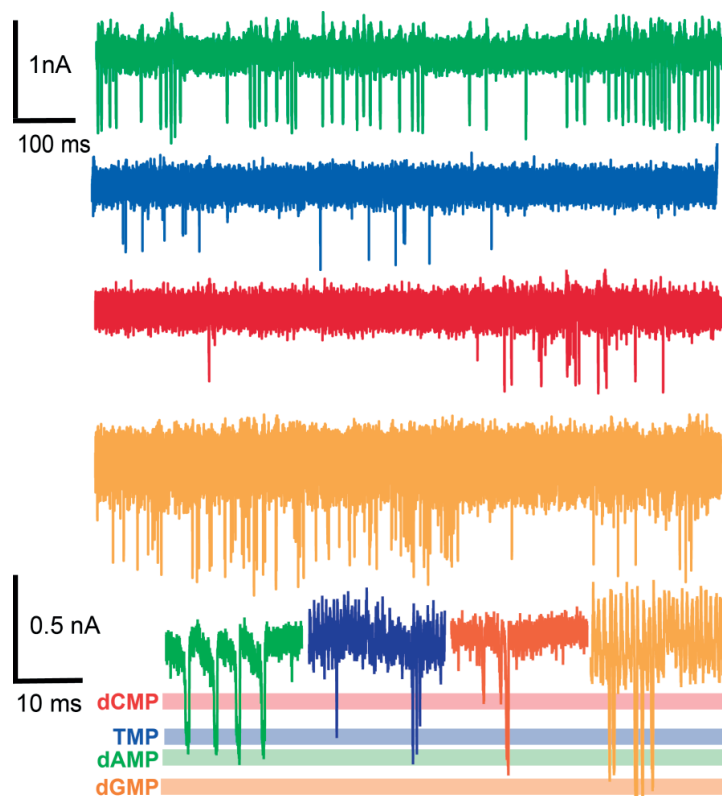


Figure 3.17. Differentiation of single DNA nucleotides in the 2.8 nm MoS₂ nanopore under ionic liquid/KCl gradient condition. 0.5 s and 0.1 s translocation signals for each nucleotide dAMP (green), dCMP (red), dTMP (blue), and dGMP (orange). Figure reproduced from Nature publication[142].

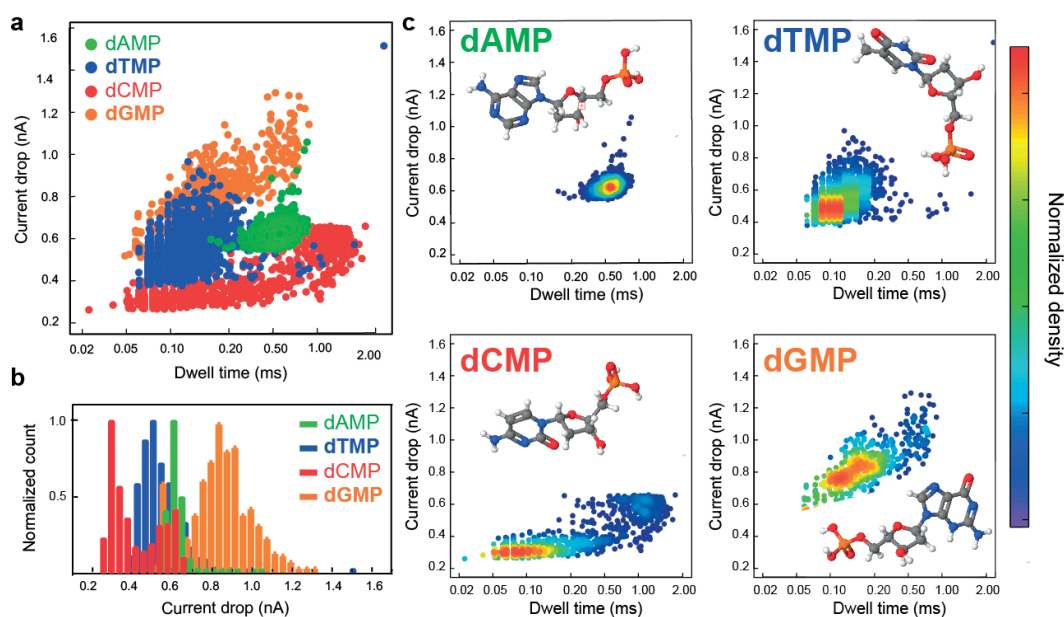


Figure 3.18. Identification of single nucleotides in a MoS₂ nanopore. **(a)** Scatter plots of nucleotide translocation events, showing distinguished current drops and dwell times for dAMP (green), dCMP (red), dTMP (blue), and dGMP (orange). **(b)** Normalized histogram of current drops for dAMP, dTMP, dCMP, dGMP. **(c)** Density plot of single nucleotides in MoS₂ nanopore; for dAMP, the position of the hot spot is (0.5, 0.62), for dTMP, (0.09, 0.49), for dCMP, (0.06, 0.31) and for dGMP (0.15, 0.83). The color-map at the right shows the normalized density distribution of events. Data acquired in pure RTIL *cis* chamber, 100 mM KCl, 25 mM Tris HCl, pH 7.5, *trans* chamber, at +200 mV. The nucleotide concentration in RTILs was 5 μg/ml. Insets show 3D models for the chemical structure of nucleotides. Figure reproduced from Nature publication[142].

Each experiment has been preceded with the flushing of the fluidics and with the short control experiment to confirm the absence of the analyte from the previous experiment. Not only does this show the extraordinary resilience of our nanopores, but, to our surprise, the dwell times of single nucleotides are comparable to those of 30mer homopolymers (**Figure 3.18**). At this scales, when comparing the dwell times of single nucleotides to homopolymers, one needs to account for the charge reduction difference that will result in the lower net force acting on the single nucleotide compared to the homopolymers. In the pores with diameters < 5 nm, observed translocation retardation is a cumulative effect that includes several components:

interaction of the translocating molecule with the pore wall, electrostatic interaction between Bmim⁺ cations and phosphate groups of DNA, the hydrophobic association between Bmim⁺ and DNA bases[148] and finally, the viscosity gradient. The contribution of the viscosity gradient to the retardation will increase with the increasing DNA length. Consequently, for single nucleotides this contribution is decreased, however due to the charge reduction, the lower net force acting on the single nucleotide might account for observed long translocation times of single nucleotides.

The use of single-layer MoS₂ as the membrane material and the viscosity gradient system in combination with the small nanopore have been crucial for the single nucleotide discrimination as shown in **Figure 3.18**. Here, the obtained translocation speed is in the range from 1-50 nt/ms. In accordance with the physical dimensions for four nucleotides, we observe for dGMP, centered at 0.8 nA and a smallest current drop for the smallest single nucleotide dCMP, centered at 0.3 nA. These observations are in good agreement with the results obtained on single nucleotide discrimination using protein pores[47, 84, 117]. Although the current drop for dAMP is slightly larger than dTMP (0.65 nA compared to 0.45 nA), we believe that this inconsistency might be due to the stronger Bmim⁺ affinity towards dAMP compared to dTMP[149]. It has been established that RTILs could selectively bind to DNA[145], while RTILs based on metal chelate anions could be designed to have specific bonding to the bases[150]. In our system, this could be further exploited to amplify the small differences in bases. Using only ionic current drops of 500-3000 events for four nucleotides, we performed a Welch's t-test and found p-values to be all less than 0.0001. Moreover, this simple statistical analysis revealed a minimum event number to be 6-9 for nucleotide identification with a confidence of 99%. With the addition of the other parameters such as dwell time it might be possible to identify single nucleotides with one read while the presence of a direct band gap in MoS₂ should allow for straightforward multiplexing in a detection scheme based on the transverse current.

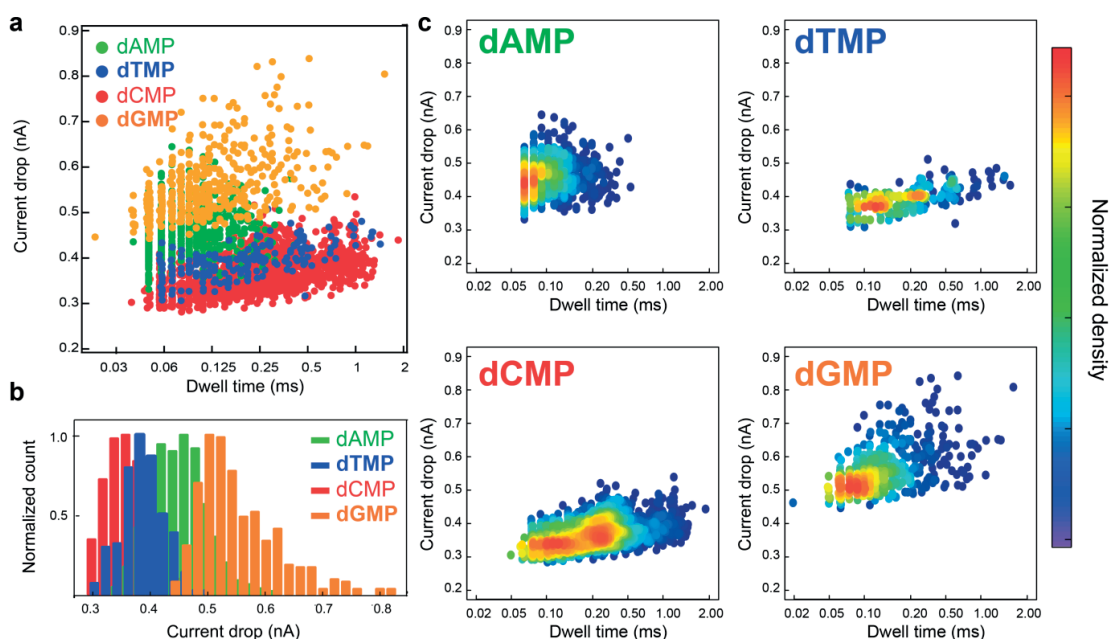


Figure 3.19. Identification of single nucleotides in a 3.3 nm MoS₂ nanopore. **(a)** Scatter plots of nucleotide translocation events, showing distinguished current drops and dwell times for dAMP (green), dCMP (red), dTMP (blue), and dGMP (orange). **(b)** Normalized histogram of current drops for dAMP, dTMP, dCMP, dGMP. **(c)** Density plot of single nucleotides in the MoS₂ nanopore; for dAMP, the position of the hot spot is (0.07, 0.46), for dTMP, (0.10, 0.40), for dCMP, (0.11, 0.36) and for dGMP (0.08, 0.56). The color-map at the right shows the normalized density distribution of events. It is clear that in the slightly larger pore nucleotide translocation events are faster and have smaller current amplitude drops. However, the trend of current drops for different types of nucleotides remains the same as shown in **Figure 3.18**. (dGMP>dAMP>dTMP>dCMP). Data acquired for an experimental condition of pure RTIL in the *cis* chamber and 100 mM KCl, 25 mM Tris HCl, pH 7.5 in the *trans* chamber. The bias is +200 mV. The nucleotide concentration in RTILs was 5 μ g/ml. Figure reproduced from Nature publication[142].

We have also reproduced the discrimination of single nucleotides in a slightly bigger pore with a diameter of 3.3 nm under the same conditions of the viscosity gradient system (**Figure 3.19**) and with a similar number of events (>10000).

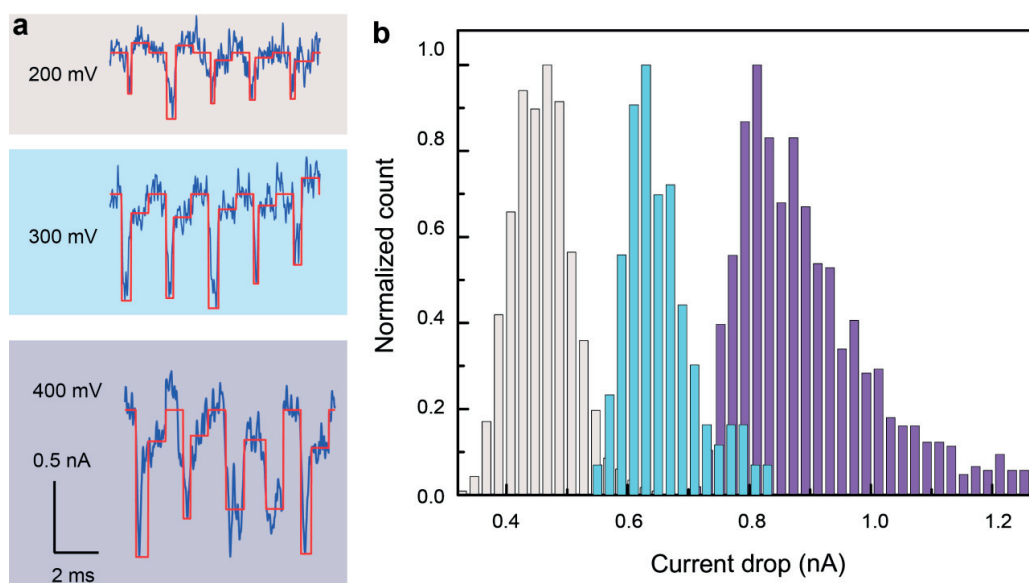


Figure 3.20. Recorded current blockade under different voltages. Example traces (a) and histograms (b) of dAMP translocation through a 3.3 nm MoS₂ pore in the presence of a viscosity gradient (ionic liquids/KCl), for different voltages (200 mV, 300mV and 400mV). The mean values for current drops are 0.46 nA, 0.65 nA, 0.91 nA, for 200 mV, 300mV, 400mV, respectively. Figure reproduced from Nature publication[142].

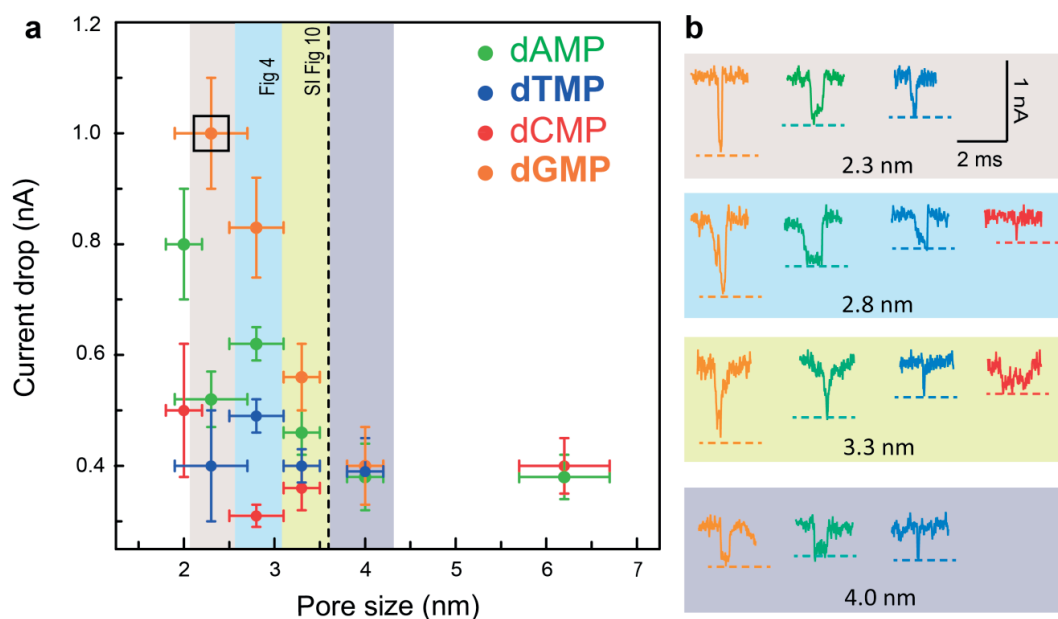


Figure 3.21. Pore size dependent differentiation/identification of four nucleotides based on ionic current drops. **(a)** Correlation between mean current drops of four nucleotides and pore sizes. Solid circles represent the experimentally determined mean current drops (standard deviation) for dAMP (green), dCMP (red), dTMP (blue), and dGMP (orange), respectively. Errors of pore sizes originate from the asymmetry of electron beam drilled pores. The black dashed line (around 3.6 nm) represents the maximum pore size that still allows differentiating between nucleotides. Nucleotides can be statistically identified within pores smaller than the critical size that is between 3.6 and 4 nm. Black rectangle indicates the data set with highest SNR (~16). **(b)** Typical events related to four nucleotides (labeled in color) translocating through MoS₂ nanopores with different diameters. The levels indicate the mean values for the current drops. Figure reproduced from Nature publication[142].

When translocating single nucleotides (such as dAMP) and increasing the potential (from 200 mV to 400 mV), we have observed increases in the current drop amplitudes as shown on **Figure 3.20**, further confirming that observed events are indeed from single nucleotide translocation. However, applying a higher potential caused an increase in the low frequency noise. The data presented on **Figure 3.17** and **Figure 3.20** are therefore collected at 200 mV. As expected, in the 3.3 nm pore, the translocation events (>10000) were faster and produced smaller current amplitude drops compared to the 2.8 nm pore and other smaller pores (**Figure 3.21**). However,

the trend of current drops for different types of nucleotides remained the same, as shown in **Figure 3.18**. (dGMP>dAMP>dTMP>dCMP). Similarly as we did for the 2.8 nm pore, by performing the Welch's t-test, we found that 14 events are needed for nucleotide identification with 99% confidence. **Figure 3.21** shows correlation between mean current drops related to four nucleotides and pore sizes. The dashed line placed between 3.5 nm and 4 nm indicates the maximum pore size that still allows nucleotide differentiation. In addition, translocating nucleotides in pores as small as 2 ± 0.2 nm can dramatically increase SNR up to 16.

3.8. DNA sequencing with MoS₂ nanopores

To conclude, we have demonstrated that single-nucleotide identification can be achieved in MoS₂ nanopores by using a viscosity gradient to regulate the translocation speed. The viscosity gradient system cannot only be used in standard ionic sensing experiments but it can be potentially combined with other schemes of nanopore sensing such as transverse current signal detection. The ultrahigh viscosity of ionic liquids results in reduced capture rates. Therefore, an optimal experimental configuration would capitalize on high-end electronics[82] and the viscosity gradient system presented here with a suitable capture rate.

3.8.1. Signal to noise ratio

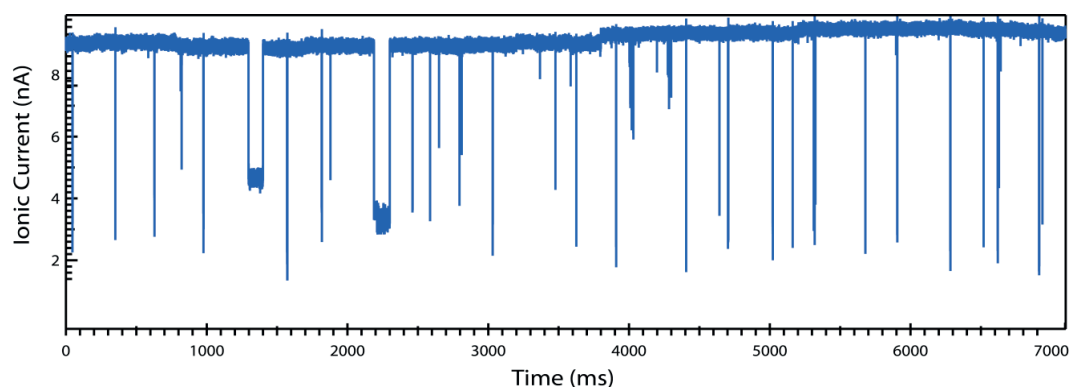


Figure 3.22. Improved signal to noise ratio (> 100). Translocation of 30mer single strand DNA through a 1.5 nm ECR-made MoS₂ nanopore. Condition: BminPF₆/1 M KCl @400 mV. Sampling and display frequency is 100 kHz and low passed by 10 kHz with Axopatch. This signal to noise ratio is obtained with noise pre-treated

Chapter 3. Nucleotide structures probed by MoS2 nanopores

device and noise reduction could further improve it to 1000 at this condition and allows measurement at higher bandwidth.

We have reached SNR up to 100 with some devices (current drop 4 nA and noise 40 pA RMS) at the bandwidth of 100 kHz. SNR can be still improved by noise reduction (polymer layer coating can reduce noise to 6 pA and the future glass substrate fabrication could potentially push the baseline noise to sub-10 pA).

The signal to noise ratio is of great importance to sequencing speed and accuracy. To this end, solid-state nanopores have greater potential over than biological nanopores. Due to the high field in 2D nanopores, the current signal is in nA level, which is 2-order magnitude higher than biological nanopore. This would result in a much higher bandwidth that allows fast DNA sequencing while keeping the required SNR according to accuracy needs.

3.8.2. Preliminary nanopore sequencing results for short DNA heteropolymers

AAAAAGGGGGAAAAAGGGGGAAAAAGGGGG

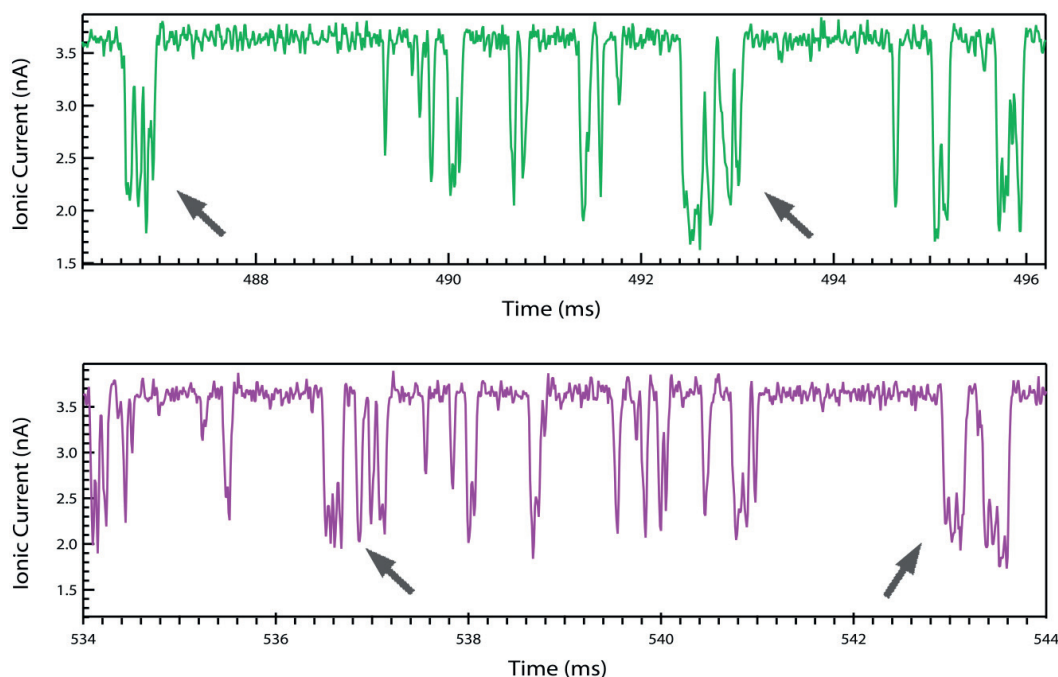


Figure 3.23. Sequence-specific current trace of 30mer (AAAAAGGGGGAAAAAGGGGGAAAAAGGGGG) at 200 mV. In order to show the uncertainty in the

experiment, continuous trace is displayed and one could find some events with multiple levels, which might correspond to designed DNA sequence.

Reproducibility and data extraction are the major problems. We obtained some signals but they are more randomly distributed into noisy raw data.

3.8.3. Identifying better choice of ionic liquids for DNA translocations

We tried hydrophilic ionic liquids to improve the capture rates but the translocation is also faster in this case. In addition, cation or anion of ionic liquid can also bind to nucleotide and by designing its chemical structures; we might be able to amplify the signal difference (Tags).

3.8.4. Statistics: Ping-pong setup that allows remeasuring the same DNA

We had several problems for ping-pong experiments[151]: a. Voltage trigger in LabVIEW for event recognition and b. Detection of recaptured event is drawn in the long duration of capacitance charging.

3.8.5. Temperature regulation of DNA translocation dynamics

Temperature control is being integrated to the current flow cell with tunable temperature range from 275K to 298K.

3.8.6. Solid-state sequencing: the 4.5th generation DNA sequencing.

Although the delivery of strand sequencing with solid-state nanopores may still take some time, single nucleotide identification has set the stage for future strand sequencing with solid-state nanopores. We believe that combining ionic liquids and monolayer MoS₂ nanopores, together with the readout of transverse current, either using the tunneling[58, 62] or FET modality[60, 61], would reach all the necessary requirements for DNA strand-sequencing such as the optimal time resolution and signal resolution in a platform that allows multiplexing, thus reducing the costs and enhancing the signal statistics[38-40].

Chapter 4. Mesoscopic physics: ionic Coulomb blockade in nanopores

4.1. Introduction

Electrical transport through single molecules has attracted considerable attention[152] due to the potential of using individual molecules as electronic components[153]. The first generation of single-molecule electrical measurements was realized by probing transport in single quantum dots, carbon nanotubes, C₆₀ molecules and DNA molecules using microfabricated structures, mechanically formed molecular junctions and scanning probe microscopies[154]. Such ultra-small platforms offer an ideal toolbox for probing electrons one at a time through the individual molecules, enabling direct observation of single-electron phenomena, such as Coulomb blockade, or the Kondo effect[155] that have substantially contributed to our understanding of fundamental quantum physics and might lead to the realization of diverse quantum devices.

Analogous mesoscopic phenomena have also been predicted for ionic transport through narrow channels when it approaches the dimensions of the hydration layers formed around each ion[156, 157]. At very low densities one should then observe single-particle step-like conductance due to the breaking of hydration layers as a function of channel radius[156, 157], while at larger densities ion-ion interactions should lead to the equivalent of Coulomb blockade when the channel has the appropriate capacitance[156, 158]. However, due to the requirement of controlled sub-nm channels, these phenomena have not been observed so far for ionic transport in nanofluidic systems[159]. Instead, ionic transport through nanochannels/nanopores typically exhibits ohmic behaviour. Voltage activated non-linear ion transport was also observed in various systems, such as hydrophobic wetting and ion dehydration[160, 161].

This chapter will describe the conventional ion transport, mesoscopic electronic transport theory and the experimental observation of ionic Coulomb blockade in ion transport through nanopores, as its counterpart in quantum dots.

4.2. Conventional ion transport through nanopores

Ion transport through membrane ion channel plays essential function in fundamental biological process, for example the transfer of signals through neurones. Conventional ion transport in nanopore can be described by Poisson–Nernst–Planck equations[162].

The PNP set of equations extends Fick’s law for the case where the diffusing particles/ions are displaced with respect to the fluid by the electrostatic force. In particular, all ion fluxes are modeled by the Nernst-Planck equation,

$$\mathbf{J}_i = -D_i \nabla c_i - \frac{Fz_i}{RT} D_i c_i \nabla \Phi \quad (4-1)$$

where \mathbf{J}_i and D_i are, respectively, the ion flux vector and diffusion coefficient of species i in the solution, T is the absolute temperature, Φ is the local potential, z_i is ionic charge and F Faraday’s constant. The relationship between the net electric charge of polyelectrolyte and local average electrostatic potential is described by the Poisson’s equation,

$$\nabla^2 \Phi(r) = -\frac{\rho(r)}{\varepsilon} \quad (4-2)$$

In the absence of ion concentration gradient, the current-voltage relation is captured by the *Ohm’s* law $J = \sigma E$, where J is the current density at a given location in a resistive material, E is the electric field at that location, and σ is the conductivity. This would result in a uniform conductance in all voltage range, as shown in **Figure 4.1**.

When working with high ion concentrations (molarity > 1 M), the surface charge contribution to conductance could be negligible due to charge screening. Application of a fixed voltage generates the flux of K^+ and Cl^- ions that result in the net current that can also be roughly described by the Hall equation[105].

$$G = \sigma \left[\frac{4L}{\pi d^2} + \frac{1}{d} \right]^{-1} \quad (4-3)$$

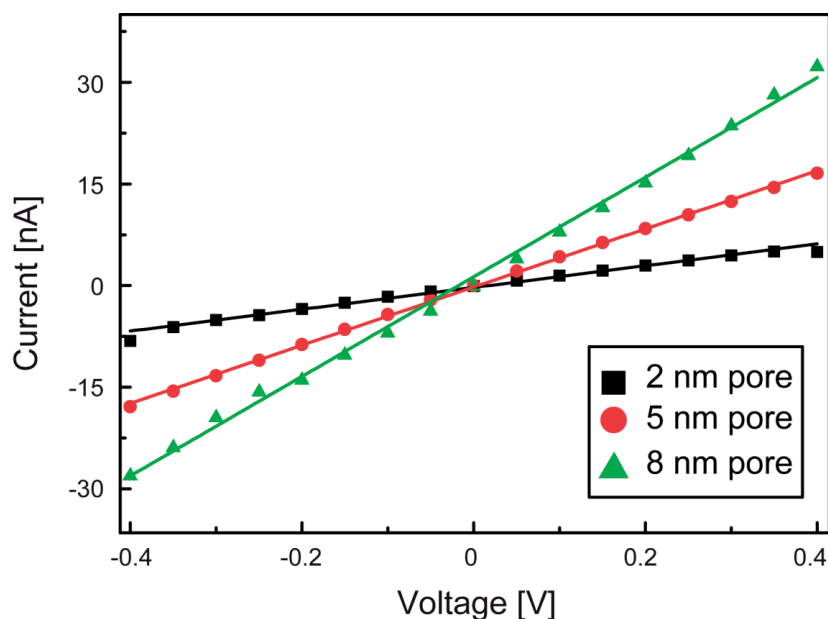


Figure 4.1. Examples of current-voltage I-V characteristics taken in 2 nm, 5 nm, and 8 nm MoS₂ nanopores using 1 M KCl, at pH 7. Ionic transport through a MoS₂ nanopore larger than 1 nm displays Ohmic behavior with linear I - V characteristics. Figure reproduced from Nature publication[163].

In the following **chapter 5**, we also discussed conductance when considering the surface charging contribution at low ion concentrations.

4.3. Coulomb blockade theory and observation in quantum dots

Electronic transport in nanoscale usually does not obey *Ohm's* law. In the nanoscale, the following effects dominate: the size which is smaller than the mean free path, the large contact barrier and the large charge addition energy and quantized excitation spectrum. Various mesoscopic effects have also been experimentally observed in metal nanostructures, carbon nanostructures, quantum dots and single molecules. This section will focus on Coulomb blockade: the suppressed conductance at low applied voltage due to charging effect induced by low capacitance of the system. Coulomb blockade was first introduced by Gorter in 1951[164], known as Coulomb blockade of single electron charging[165].

For the theoretical description, we followed the model used by Kouwenhoven et al.[166] and more detailed derivation can also be found in the review by Beenakker[165]. **Figure 4.2** shows a schematic of a single quantum dot device with capacitively coupled electrodes: source, drain and the gate. Electron transport is allowed between the source, drain electrode and the dot. An electrostatic energy change in the dot can be caused by the potential change in the electrode. The tunneling barrier between the dot and drain source electrode defines the number of electrons N on the dot. Let us assume that the interaction between one electron on the dots and other electrons either on the dot or electrode can be parameterized by the total capacitance C . If we first assume that the total capacitance is not depending on the charge state of the dot, the total electrostatic energy for N electrons on the dot can be then written as $(Ne)^2 / 2C$. The energy of the orbital of the dot that the i -th electron would occupy if there were no electron-electron interactions known as chemical potential can be described by E_i , then the total energy of the N -electron dot system can be obtained as,

$$U(N) = \sum_{i=1}^N E_i + (Ne)^2 / 2C \quad (4-4)$$

Adding one electron to the system will lead to,

$$U(N+1) = \sum_{i=1}^{N+1} E_i + [(N+1)e]^2 / 2C \quad (4-5)$$

The electrochemical potential of the N -electron system is then,

$$\mu_N \equiv U(N) - U(N-1) = E_N + (2N-1)e^2 / 2C \quad (4-6)$$

The number of electrons is changed by one; the resulting change in electrochemical potential is,

$$\mu_{N+1} - \mu_N = \Delta E + e^2 / C \quad (4-7)$$

Where $\Delta E = E_{N+1} - E_N$.

This additional charging energy includes two contributions: the quantized excitation spectrum ΔE and the charging energy e^2 / C due to Coulomb repulsion between electrons.

This non-zero addition energy can lead to a blockade for tunneling of electrons on and off the dot where N electrons are localized on the dot. Therefore, the electron transport is blocked when $\mu_N < \mu_d$, $\mu_s < \mu_{N+1}$ where μ_s and μ_d are the electrochemical potentials of drain source electrode (the applied bias $V_{sd} = (\mu_s - \mu_d) / e$), which is known as the Coulomb blockade.

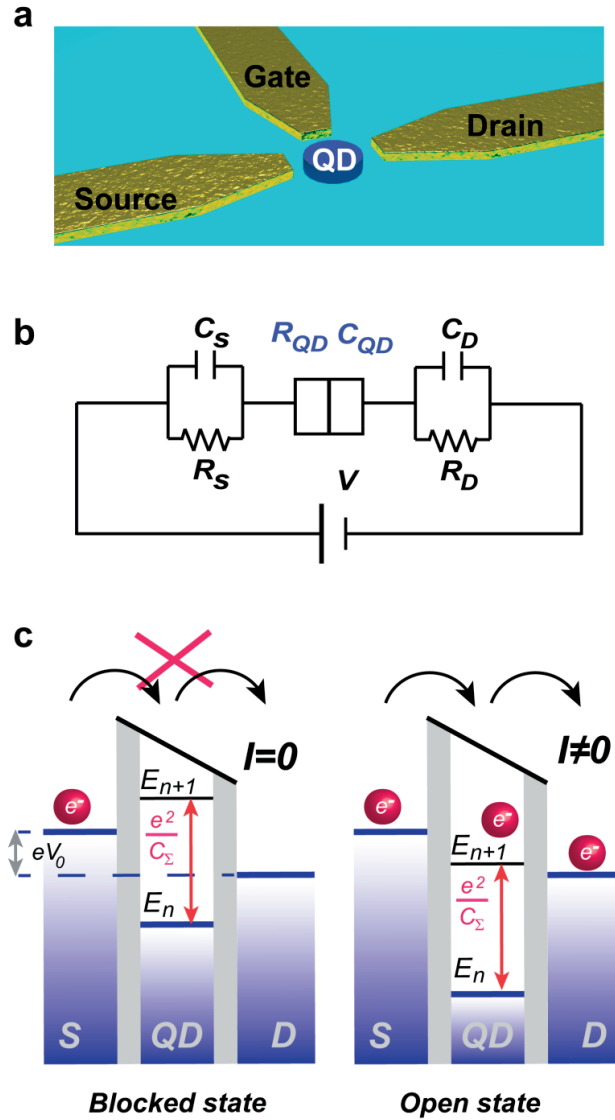


Figure 4.2. Proposed energy-level diagram of the single quantum dot. **a).** Illustration of the solid-state quantum dot device with a source, drain and gate electrode. **b).** Corresponding equivalent circuit for a system shown in (a). **c).** Energy level diagram for a quantum dot system. Figure reproduced from Nature publication[163].

Chapter 4. Mesoscopic physics: ionic Coulomb blockade in nanopores

Coulomb blockade can be removed by changing the gate voltage, to align μ_{N+1} between μ_s and $\mu_d > \mu_{N+1}$, as,

$$\mu_N = E_N + (2N - 1)e^2 / 2C - e \frac{C_g}{C} V_g \quad (4-8)$$

Where C_g is the capacitance between the dot and gate and V_g is the gate voltage.

One electron can tunnel from the drain on the dot when $\mu_d > \mu_{N+1}$ and an electron can also tunnel off from the dot to source if $\mu_{N+1} > \mu_s$ (**Figure 4.3**). By sweeping the gate voltage, the conductance can oscillate between blockade and non-blockade, as shown in **Figure 4.3**. The number of electrons on the dot is fixed by the gate voltage. The oscillation distance on gate voltage can then be written as,

$$\Delta V_g = \frac{C}{eC_g} (\Delta E + e^2 / C) \quad (4-9)$$

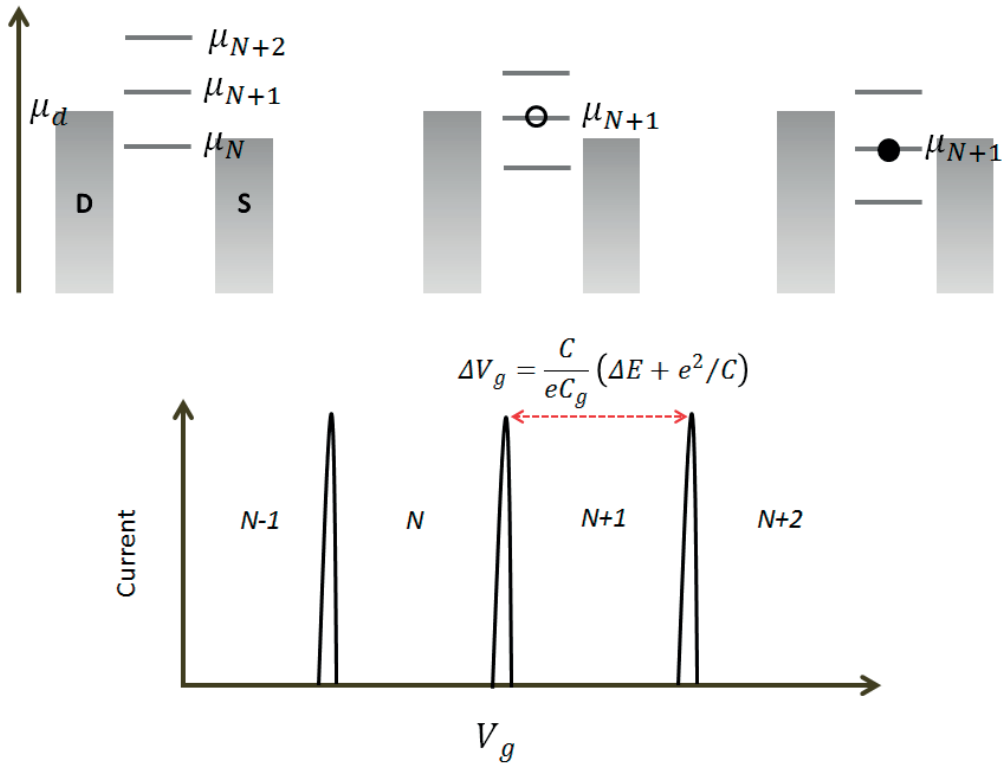


Figure 4.3. The energy diagrams of a quantum dot with multiple levels and the Coulomb oscillations.

To observe Coulomb blockade, first, the additional energy should be much larger than thermal energy $k_B T$ or else the electron will be able to pass via thermal excitation. A second requirement is that the barriers should be sufficiently opaque such that the electrons are located either in the source, in the drain, or on the dot. The typical time to charge or discharge the dot is given as $\Delta t = R_t C$, where R_t is the tunneling resistance. Heisenberg uncertainty relation sets $(e^2 / C)\Delta t > h$, and therefore the tunneling resistance $R_t \gg h / e^2$.

To summarize, the two conditions to observe Coulomb blockade due to charge discreteness are given by,

$$e^2 / C \gg k_B T \quad (4-10)$$

$$R_t \gg h / e^2 \quad (4-11)$$

Coulomb blockade was first observed by Fulton in metallic nanostructures[167] and so far it has also been found in quantum dots, carbon nanotubes and single molecules[154].

4.4. Observation of ionic Coulomb blockade

Such abovementioned behaviour from electron-transport properties is routinely observed in systems with dimensions approaching the nanoscale[168]. However, analogous mesoscopic behaviour resulting from ionic transport has so far not been observed, most probably because of bottlenecks in the controlled fabrication of sub-nanometre nanopores for use in nanofluidics. Here, we report measurements of ionic transport through a single sub-nanometre pore junction, and the observation of ionic Coulomb blockade: the ionic counterpart of the electronic Coulomb blockade observed for quantum dots. Our findings demonstrate that nanoscopic, atomically thin pores allow for the exploration of phenomena in ionic transport, and suggest that

Chapter 4. Mesoscopic physics: ionic Coulomb blockade in nanopores

nanopores may also further our understanding of transport through biological ion channels.

Here, we show for the first time the experimental observation of single-ion transport through the ionic junction of a sub-nm MoS₂ pore. We observe that the current-voltage characteristics of ionic transport display nonlinear behaviour that exhibits a voltage gap at low applied bias. We suggest a single-ion transport mechanism based on single-ion charging where the combination of Coulomb blockade and dehydration determinates the ion transport through the sub-nm pore. Our observation is in a good agreement with predictions obtained for both solid-state pores[156] and a biological ion channel that has similar geometry as the sub-nm solid-state nanopore reported here[158] and it is reminiscent of the same phenomenon observed in electronic transport through quantum dots.

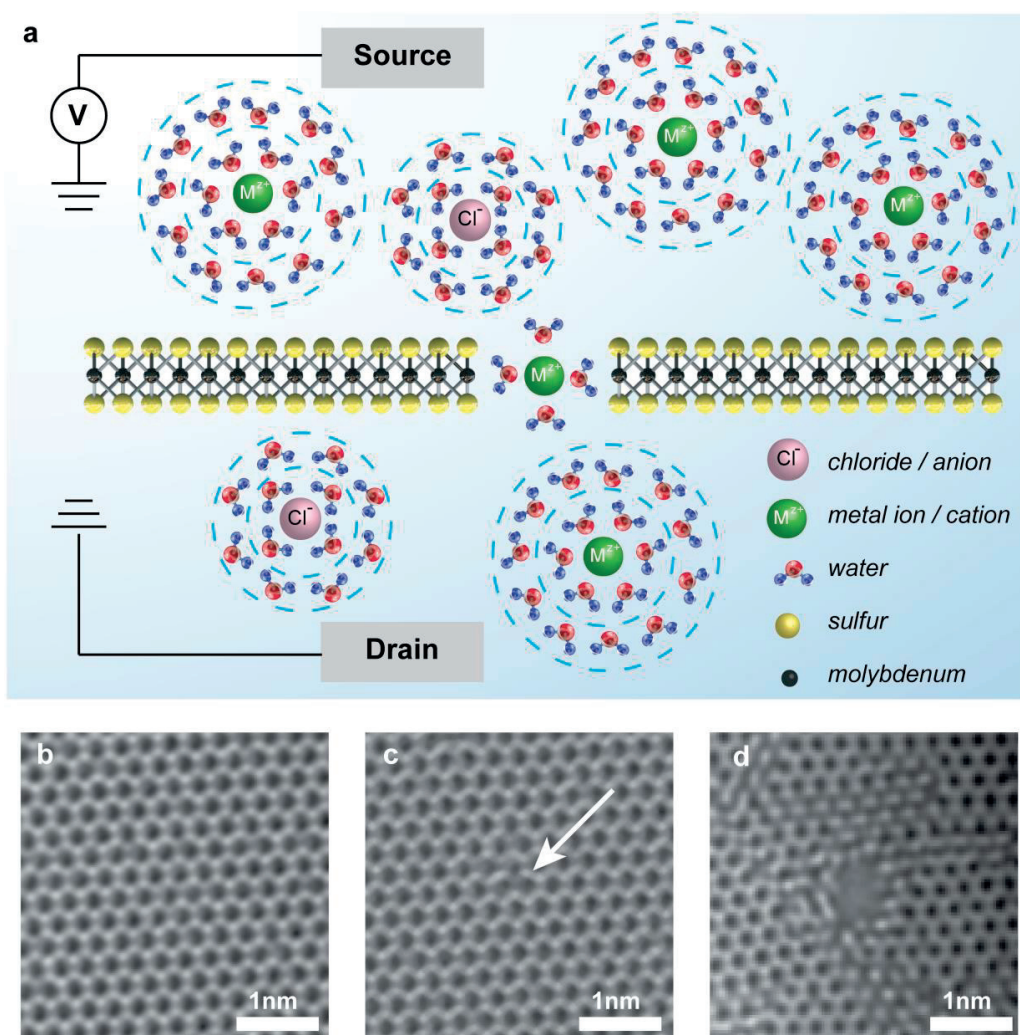


Figure 4.4. **a).** Schematics of single ion transport through a sub-nm MoS₂ nanopore. **b).** Aberration-corrected TEM image of a single-layer MoS₂ membrane without a pore. **c).** Aberration-corrected TEM image of a single-atom vacancy (marked by arrow) in a single-layer MoS₂ membrane. **d).** Aberration-corrected TEM image of 0.6 nm diameter MoS₂ nanopore. Figure reproduced from Nature publication[163].

The experiments are conducted in a typical configuration where the two chambers with ionic solutions are separated by a single nanopore in a single-layer molybdenum disulphide (MoS₂) membrane[98] and biased by a pair of Ag/AgCl electrodes, as described in **Figure 4.4 a**. The sub-nm nanopores used in this study are produced in a single-layer MoS₂ membrane by either our recently reported atomic-scale nanopore fabrication technique using controlled electrochemical reaction or by electron

Chapter 4. Mesoscopic physics: ionic Coulomb blockade in nanopores

irradiation within a Cs-corrected transmission electron microscope, as described elsewhere[97, 98]. These techniques result in the opening of pores with diameters down to 0.3 nm. From the plethora of 2-dimensional materials we have chosen 0.65 nm thick single-layer MoS₂[98], due to the fact that it allows better control during nanopore fabrication[97, 98] and nanopores that exhibit better water transport when compared to graphene[169]. **Figure 4.4 b** shows an image of pristine single-layer MoS₂, a sulphur vacancy that acts as an initial site for nanopores formation during electrochemical reaction (**Figure 4.4 c**) and a 0.6 nm diameter nanopore (**Figure 4.4 d**). For measurements in this work, we have mostly used pores fabricated using controlled electrochemical reaction[97]. Electrical characteristics of the pore are then determined by acquiring their current-voltage (I - V) response in aqueous solution of salts.

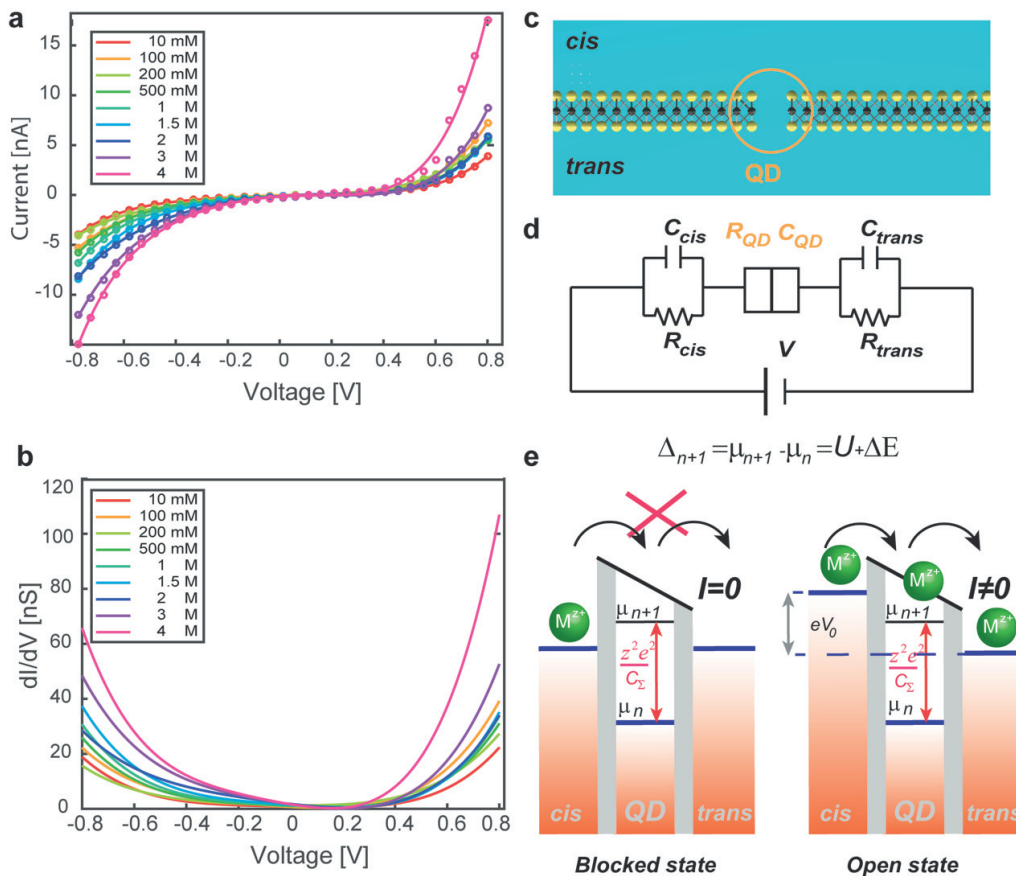


Figure 4.5. Current–voltage characteristics (I - V) of a 0.6 nm MoS₂ nanopore in a potassium chloride aqueous solution (KCl). **a**). I - V curves acquired under different ion concentrations. **b**). differential conductance (dI / dV) of a 0.6 nm MoS₂ in KCl

solutions of different molarities. Proposed energy-level diagram of the single ion channel system and the analogy to electron transport through a quantum dot. **c).** Illustration of single ion junction in the form of a small-diameter nanopores in a 2D material MoS₂. **d).** Corresponding equivalent circuit for a system shown in **(c)**. **e).** Equivalent energy level diagram for ionic Coulomb blockade due to single-ion charging in nanopores. With the presented sub-nm pore configuration, this charging energy is much larger than thermal energy ($k_B T$) or else the ion will be able to pass via thermal excitation. Ionic conduction is suppressed (Blocked state, left) when applied bias (eV) is below the charging energy. A build-up in voltage above the charging energy allows conduction (Open state, right) with a strong dependence on ion valence number z . Figure reproduced from Nature publication[163].

All I - V measurements are performed at room temperature. **Figure 4.5 a** shows typical I - V characteristics of a 0.6 nm pore in potassium chloride (KCl) aqueous solutions with various ionic strength (10 mM - 4 M). The curves exhibit a striking non-linear behaviour with an apparent gap of ~ 400 mV. At small voltages, the current is suppressed. When the bias voltage exceeds the threshold value, the current starts to increase more strongly. Corresponding differential conductance (dI/dV) plots are shown at **Figure 4.5 b**. Zero conductance is found in the gap region as well as a conductance which increases with applied bias. This phenomenon differs largely from conventional ion transport through nanopores with larger sizes[170], which can be described using classical Poisson–Nernst–Planck equations[171]. Representative I - V curves from larger MoS₂ pores ($d > 1$ nm) are shown in **Figure 4.1**, displaying linear, ohmic responses. The response of another 0.6 nm MoS₂ nanopore to different ion types is shown in **Figure 4.6**. All tested metal ion types (K^+ , Na^+ , Li^+ , Ca^{2+} , Mg^{2+}) exhibit nonlinearity in their I - V characteristics (**Figure 4.6 a**), with different gap sizes for different ions and a strong dependence on the valence (referring to differential conductance shown in **Figure 4.6 b**). Compared to other ions, the I - V characteristic of divalent ions Mg^{2+} and Ca^{2+} shows more suppressed current in positive voltages in contrast to monovalent ions K^+ , Na^+ , Li^+ . The hydrophilic nature of MoS₂ pores due to the Mo-rich pore surface and the pore wetting procedure we use that involves soaking nanopores in the ethanol/water mixture, eliminates the possibility that nonlinearity originates from hydrophobic effects[160, 172].

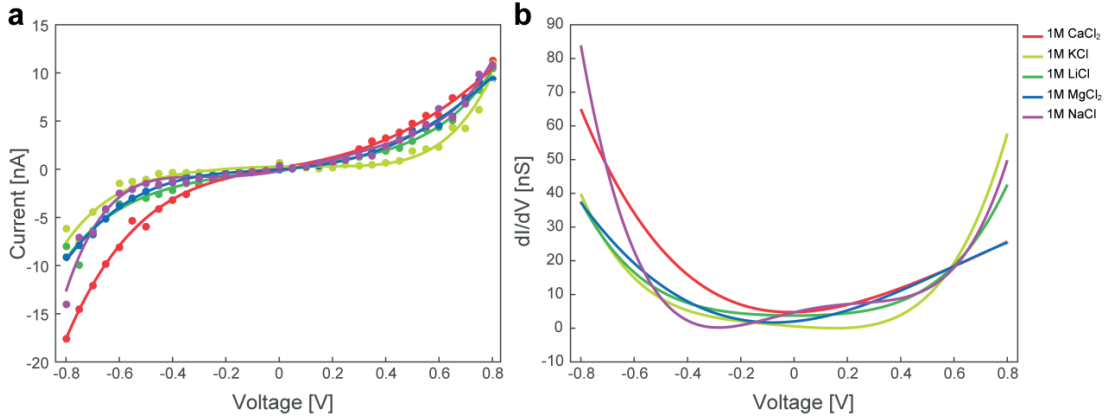


Figure 4.6. Valence-dependent ion transport. **a).** Current-voltage I - V characteristics of a 0.6 nm MoS₂ pore taken in different salt solutions (K⁺, Na⁺, Li⁺, Ca²⁺, Mg²⁺). **b).** Corresponding differential conductance dI/dV plots. Mg²⁺ and Ca²⁺ have more suppressed current in positive voltages. Figure reproduced from Nature publication[163].

To understand the nature of ionic transport measurements, first, we used an analogy to electric transport through a quantum dot/single molecule system[154]. Here, the small capacitance of a system weakly coupled to electrodes through tunnel junctions gives rise to Coulomb blockade[165, 167]. In the schematics on **Figure 4.5 c, d**, and energy diagrams on **Figure 4.5 e** we attempt to define the "electronic structure" of the single-ion channel device and employ the Coulomb blockade theory for ionic transport. In addition to a resistance, a nanopore junction also has a capacitance. A charging energy then needs to be overcome when the capacitance of the system is small enough so that many-body ion-ion interaction effects dominate. Therefore, the suppressed conductance in the subthreshold regime is a consequence of the finite energy required to add a charge carrier (ion) to the pore. Referring to Coulomb blockade model[166] this addition energy (Δ_{N+1}) is given by (analogy to equation 4-7),

$$\Delta_{N+1} = \mu_{N+1} - \mu_N = U + \Delta E \quad (4-12)$$

where μ_N is the electrochemical potential; U is the Coulomb interaction energy between two ions in the pore and ΔE is the electronic excitation energy.

Ionic Coulomb interaction can be estimated using electrostatic self-energy[173] considering one dimensional Coulomb gas model of ions[174]. Following ionic

Coulomb blockade model developed by Kaufman et al[158], the Coulomb gap can be obtained as a function of pore geometry and ion valence[158, 174],

$$U = \frac{z^2 e^2}{2C} = \frac{1}{4\pi\epsilon_0} \frac{z^2 e^2 L}{2\epsilon_w r^2} \quad (4-13)$$

Where e is the elementary charge; ϵ_0 is vacuum dielectric constant and ϵ_w is the water dielectric constant; C is the geometry-dependent self-capacitance[174] of the pore given by $4\epsilon_w\epsilon_0\pi r^2 / L$; z is the ion valence number; r is the radius of the pore and L is its length. This model highlights two important contributions that lead to ionic Coulomb blockade: a) Geometry-dependent self-capacitance similar to electronic Coulomb blockade. b) Ion valence which is unique in ionic transport. Given the verified thickness of MoS₂ nanopores and 0.6 nm pore diameter, a Coulomb energy of about $3 k_B T$ for 0.65 nm theoretical single-layer thickness and $5 k_B T$ for 1.6 nm hydration thickness[98] can be estimated for monovalent ions. For divalent ions, these values dramatically rise to $12 k_B T$ and $20 k_B T$. A detailed estimation of Coulomb gap for various pore diameters is given in **Figure 4.8**. The pore capacitance can also be extracted from the current-molarity relation[156]. A non-monotonic current molarity relation is observed, as a direct result of the capacitance effect of the pore[156]. By fitting to the classical ionic Coulomb blockade model[156] using our device geometry and experimental results presented in **Figure 4.5**, we obtain a pore capacitance of about 0.2 aF for the 0.6 nm pore, which is very close to our estimate, as shown in **Figure 4.7**. This non-monotonic behavior is also predicted where self-energy barrier vs concentration also shows a characteristic sharp dip in the vicinity of a certain negative monovalent dopants concentration explained as a transition between different states[175].

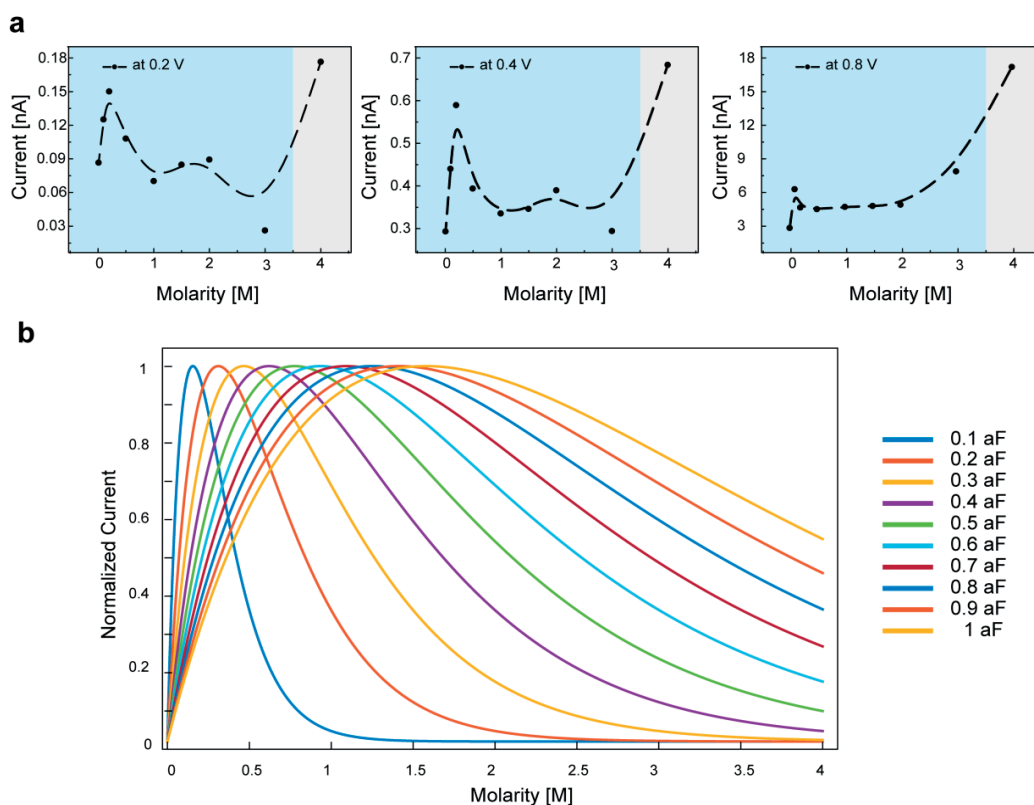


Figure 4.7. a). Current-molarity relation at 200 mV, 400 mV, 800 mV, respectively. Data taken from **Figure 4.5**. Gray region in the graphs indicates the ionic precipitation limit of KCl of about 3.5 M that can explain the large current obtained in 4 M KCl. On the other hand, a peak around 500 mM is found for all cases, which is another signature of ionic Coulomb blockade and can be fitted to plots in **b)**. Theoretically predicted current-molarity relation at different pore capacitance. The equation is taken from the simulation work[156], plotted with our device parameters, (pore diameter is set to 0.6 nm and we assumed simple cylindrical geometry of 3 atom thick pore, $L=0.65$ nm). The peak position highly depends on the pore capacitance. Peak position of 0.2 M corresponds to pore capacitance of 0.2 aF which is very close to the value estimated using the model presented in **Figure 4.5 c**. Figure reproduced from Nature publication[163].

The second effect that directly contributes to the observed energy gap is the dehydration of ions in nanopores smaller than 0.8 nm. This contribution becomes significantly large and a stepwise free energy barrier originating from successive breaking of third, second and first hydration shell is introduced when reducing the pore size from 0.8 nm to zero[157]. Therefore the dehydration effect should also be

incorporated to the energy gap. To this end, we again used an analogy to combined gap in single molecule system and in ionic case; the "energy level spacing" is treated using the hydration energy. The estimated contribution from ionic Coulomb blockade effect and dehydration effect is now shown in **Figure 4.8**. Coulomb energy is found to be major contribution in pore size range (0.6 to 1 nm). In **Figure 4.8**, we hypothesize a transition of role from dehydration (< 0.5 nm) to ion Coulomb blockade (in the range we work, 0.6 to 1 nm). The single-particle dehydration effect is thus easily incorporated in the standard model of Coulomb blockade.

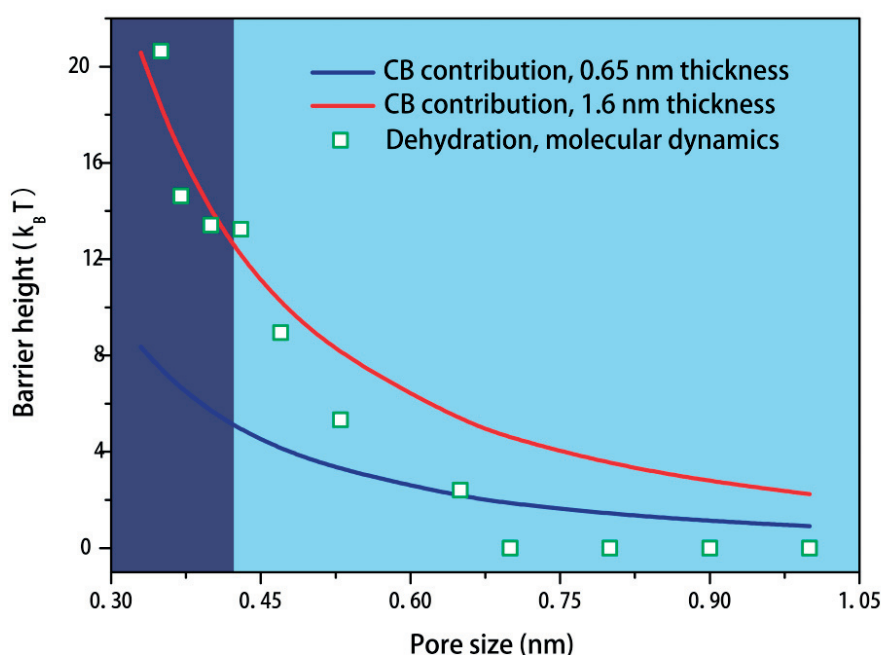


Figure 4.8. The barrier heights for Coulomb blockade and dehydration. Coulomb energy is estimated using the equation 4-13 and dehydration data is taken from the molecular dynamics simulations[157, 176]. On the left side of the boundary diameter (0.4 nm), dehydration becomes relevant due to the breaking of strong second hydration shell. After the dash line (third hydration shell), contribution from dehydration is negligible. Figure reproduced from Nature publication[163].

This charging energy is much larger than the thermal energy at room temperature ($k_B T$, 298 K) allowing the direct observation of Coulomb blockade in ionic transport at room temperature. An applied bias (eV) can adjust the chemical potential of the

electrode to add or remove a single charge carrier from the pore. When this energy rises above the Coulomb gap, the ion flux is able to pass through the pore. Measured values are in good agreement with the results from calculations outlined above. A small deviation can be expected and is due to the overestimation of the pore size and the additional capacitance between the pore and electrode. The valence dependence where divalent ions show slightly higher gap in the positive voltage direction than monovalent ions is a direct consequence of stronger Coulomb interaction between divalent ions, as shown in **Figure 4.6**. This suppression is much lower than the straightforward estimation and we believe that it is due to a combined result of gap from both divalent cations ($\text{Mg}^{2+}/\text{Ca}^{2+}$) and monovalent anions (Cl^-). Observed I - V rectification might originate from the dipolar nature of $\text{MgCl}_2/\text{CaCl}_2$ due to the difference of transport barrier for divalent cations and monovalent anions. In addition, a similar phenomenon where the self-energy barrier of CaCl_2 exhibits the same barrier as Na^+ is also theoretically predicted, and explained by the fractionalization of divalent cations ($\text{Mg}^{2+}/\text{Ca}^{2+}$) on two unit-charge mobile solitons[175].

To observe Coulomb oscillations in most traditional electrical devices[166], one would need to incorporate a voltage gate. Nevertheless, integration of the voltage gate to the atomically thick pore requires passivation with the thick layer of dielectric in order to reduce current crosstalk[61]. In turn, this requirement would compromise the atomic dimensions of our present nanofluidic device. Alternatively, in nanofluidic devices gating can be realized by using pH to modulate the surface charge of the system[177]. Surface chemistry of the MoS_2 nanopore determines the negatively charged surface and increase of pH will lead to addition of negative charges. The ionic transport can then be modulated by the surface charge. **Figure 4.9 a** (left) shows the pH (2.5 to 11) dependence of conduction in our system. A nonmonotonic dependence of pore conductance on pH is observed and the conduction peak is found around pH 3.5 and pH 6 which corresponds to a certain integral number of excess charges in the pore determined by the surface chemistry. However, the various possibilities of pore chemistry at the single-atom level[169] can lead to variations of conduction peaks from pore to pore. Kaufman et al.[158] also modelled pore charge induced Coulomb blockade oscillations via approximating self-energy, $U_n = Q_n^2 / 2C$ of excess charge (where Q_n represents the excess charge at the pore for the n ions as

function of Q_f , $Q_n = z \cdot e \cdot n + Q_f$) and applying *Fermi–Dirac* occupancy statistics. Blockade region is found around neutralized excess charge and barrier-less conduction appears at the crossover point where $U_n = U_{n+1}$, which corresponds to the conductance oscillations we observed at certain pH values.

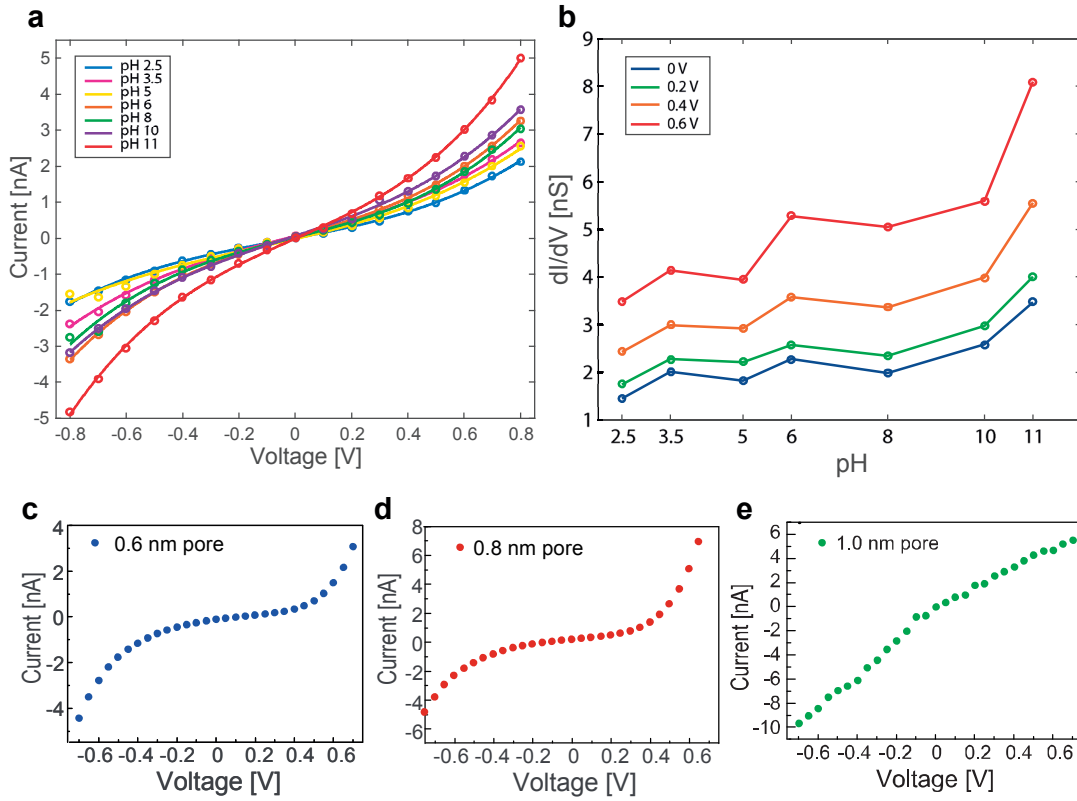


Figure 4.9. **a).** pH gated ionic transport through a 0.8 nm MoS₂ nanopore. $I-V$ curves are taken in various pH conditions of 1 M KCl (pH 2.5 to 11). **b).** dI/dV curves are taken in various pH conditions of 1 M KCl (pH 2.5 to 11). The differential conductance displays a non-monotonic behaviour to pH (surface charge). Linear-nonlinear transition by changing the pore size, 0.6 nm **c).** 0.8 nm **d).** 1 nm **e).** The gap size decreases with the pore size and disappears when the pore size reaches 1 nm. Figure reproduced from Nature publication[163].

The Coulomb gap of the single ion channel can be further engineered by adjusting the pore size. In the absence of the pore, the defect-free membrane is almost insulating and the leakage current is very low (pA range). The smallest nanopore from a single vacancy with either two sulphur or one molybdenum atom missing would produce a large gap, providing this structure is thermodynamically stable in liquid[178]. Single

vacancies can also be generated using our controlled electrochemical pore fabricating method. It is however difficult to measure the gap of a single vacancy ($d < 3\text{\AA}$) in practice because a bias voltage higher than 0.8 V can result in the electrochemical dissolution of MoS₂. We find only a handful of freestanding, defect-free MoS₂ membranes suspended over small windows ($< 50\text{ nm}$) that can operate up to 5 V. **Figure 4.10** gives an example of an I - V measurement performed on a 0.3 nm pore. A larger gap of $\sim 1.2\text{ V}$, is observed and the voltage is swept in both directions. Cyclic I - V is taken to prevent the enlargement of the existing or formation of a new pore in the presence of a high bias. We suspect the dehydration of strong second hydration shell also performs an important role here.

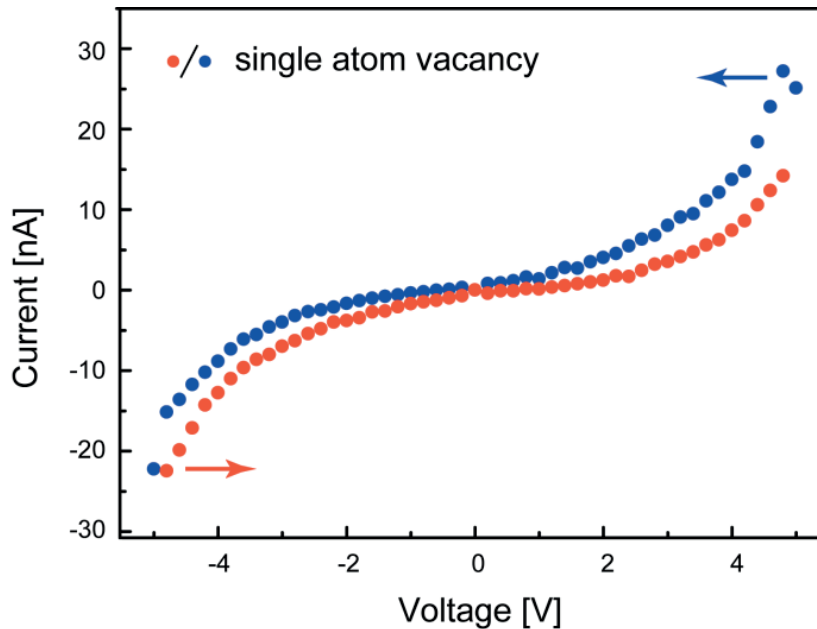


Figure 4.10. Current-voltage I - V measurements of an estimated 0.3 nm MoS₂ pore taken in 1 M KCl. A second scanning of I - V is taken to ensure the pore is not significantly enlarged by the application of high voltages. Figure reproduced from Nature publication[163].

The measured gap size decreases with increase of the pore size and the charging energy can be obtained directly from the gap. As shown in **Figure 4.9 c, d, e**, a linear transition point is found near 1 nm, indicating the disappearance of the transport barrier with the I - V characteristic becoming linear after this point. The strong correlation between the nonlinearity of current-voltage characteristics and the pore

dimension additionally confirms that ionic Coulomb blockade is at the origin of the observed effect. With larger pores, the weak Coulomb interaction could in principle be measured at low temperatures and even Coulomb stairs might be observed at low voltages. However, the operation at low temperatures is limited by the liquid environment itself. Single step transition from an insulating regime dominated by Coulomb blockade to a semiconducting regime, has been observed previously in metallic quantum dots[179, 180].

The prediction of ion transport through a symmetric biological ion channel has shown Coulomb blockade with a very similar geometry, pore size of 0.6 nm and 1.6 nm thickness[158]. The good agreement between above prediction and experimental results further strengthen our claims. Finally, although Coulomb blockade (a many-body effect)[156] is concomitant with the single-particle dehydration effect[157], the following evidence supports the contribution from Coulomb blockade: (a) Low capacitance of the experimental configuration. (b) Valence-dependence. (c) Peaks in current molarity relation. (d) Conductance oscillations from pH induced surface charge modulation.

Here we summarize the following evidence in support of ionic Coulomb blockade model.

a). Low capacitance charging model

Geometry of MoS₂ nanopores (L=1.6 nm, d=0.6 nm) presented in this work is almost identical to the biological channel modeled by Kaufman et al.[158] and the geometry-dependent self-capacitance of the channels is derived using a straightforward estimation for plate capacitor resulting in the small capacitance.

b). Valence-dependence

The Coulomb energy gap is not only a function of geometry but as well the valence and should results in the suppressed current for divalent ions, as measured in **Figure 4.6**.

c). Current molarity relation

The capacitance of the system can be extracted using current-molarity relation as suggested by the Krems et al.[156]. Although Krems et al. modeled a V shape

nanopore, it is also noted in their work that the prediction should work for cylindrical small pores[156]. In fact, we obtained comparable values for capacitance using both approaches, when we applied straight-forward geometry based capacitance calculation we obtain capacitance of 1.2 aF, while capacitance obtained by fitting the current versus molarity data as proposed by Krems et al. yields 0.2 aF for experimental peak at 200 mM and 1 aF at 2 M. Such a tiny capacitance unambiguously leads to the direct observation of ionic Coulomb blockade at room temperature (**Figure 4.7**). The second conductance “peak” around 2 M can be potentially due to different charge states (transitions from N+1 to N+2 charge states in the pore) but it may also refer to other possibilities since it occurs too close to the precipitation limit.

d). Conductance oscillations from surface charges

We used the pH to modulate the surface charges of the pore (MoS₂ is negatively charged and an increase of pH will add more negative charges to the pore) and a Coulomb oscillation has been found at certain voltages by the maximum conductance at the given pH values (**Figure 4.9**). The observed non-monotonic behavior is in good agreement with predictions by Kaufman et al[158].

4.5. Mesoscopic understandings to biological ion channels

The observation of unique ionic transport in sub-nm pores is, to our knowledge, the first instance of quantum-like mesoscopic effect dominating ionic transport. The measured nonlinear current-voltage dependence for individual sub-nm pores is a consequence of single-ion charging behaviour as described by ionic Coulomb blockade model. Other possibilities that may also introduce a transport barrier, like dehydration effect, could also be further incorporated to the standard model. Our findings can be applied to nanopores with similar geometries. Our measurements provide direct experimental evidence that effects observed here should also play a role in the functioning of biological ion channels, such as voltage-gated ion channels as suggested in the theoretical model proposed by Kaufman et al. To the best of our knowledge, many ion channel behaviour can be understood in term of Coulomb blockade, such as voltage gating, selectivity, mutation. The typical gating events in

ion channels, is very similar to the shot noise in electronics. This could be further incorporated to the mesoscopic figure of ion transport.

Future experiments investigating various gating effects and better theoretical modelling are needed to elucidate the results reported here. The blockade region also adds a new dimension to practical applications, such as water desalination. From a perspective point of view, I suggest the importance and consistence of ionic Coulomb blockade in understanding the following fundamental process of ion transport through ion channels:

- **Voltage gated ion channel can be understood as overcoming Coulomb gap**
- **The fast permeation can be explained in terms of barrier-less conduction at Coulomb oscillation point**
- **Conductance change due to mutation can refer to charge induced Coulomb blockade oscillation**
- **Coulomb blockade interpretation to light gated ion channel**
- **Calcium as inhibitors for proton transport and anomalous mole fraction effect (AMFE)**

Of course, the physics of ion channel is still very complex and it is a result of multi contributions. I am also waiting for more evidence for pushing ion transport to mesoscopic scale. We believe that atomically thin and small (< 1 nm) pores offer a new platform to explore new physics in both research areas of nanoscale fluidics and biology.

Chapter 5. Nanofluidics: ultimate osmotic power generation with 2D membranes

5.1. Introduction

Various approaches have been proposed towards energy issues we are facing. Among them, renewable energy that involves natural processes such as solar, wind, ocean, hydropower, biomass, geothermal resources, and biofuels and hydrogen, is expected to be the main energy supply in the future. Iceland and Norway have already started to generate all their electricity using renewable energy. The key limiting factors are the efficiency and power density of renewable energy harvesting and corresponding high cost. Solar cells have been one of the most attractive candidates but solar panel's theoretical limit of power density is set by the maximum solar radiation power 1.4 W/m^2 [181]. An emerging field is using water based processes for energy harvesting and due to high salt difference between sea and river water. A much higher theoretical limit of power density can be expected.

Flux of water and ions within a narrow pore/channel of a thin-membrane can be employed to generate electricity. Electrokinetic phenomena known as streaming potential occurs when an electrolyte is driven through narrow pores either by a pressure gradient, or an osmotic potential from a salt concentration gradient. Osmotic power generation from water as an energy source has been proposed by Pattle[182] and Loeb[183]. The most critical component of this power generation technology is the membrane. The efficacy of the process is linked to the membrane material but also to the dimensions of the holes in the membrane. As an emerging field, the use of new materials and new physical mechanisms was shown to outperform by orders of magnitude the present state-of-the-art using standard membranes and Pressure-Retarded Osmosis(PRO) /Reverse Electro Dialysis(RED).

The concentration gradient based processes relies on the ion selective properties of the membrane. An ion selective membrane is employed to separate the two liquids with concentration difference. When the concentrated solution of ions diffuses through the pores into the less concentrated one, due to the ion selective nature of the negatively

Chapter 5. Nanofluidics: ultimate osmotic power generation with 2D membranes

charged pores cations will diffuse more rapidly than anions (in term of transference number). This will result in an electrical double layer of positive and negative charges at the junction of the two solutions. As a result, a difference of potential is formed, namely diffusion potential. Energy harvesting from this process is known as reverse electro dialysis[184], as shown in **Figure 5.1**.

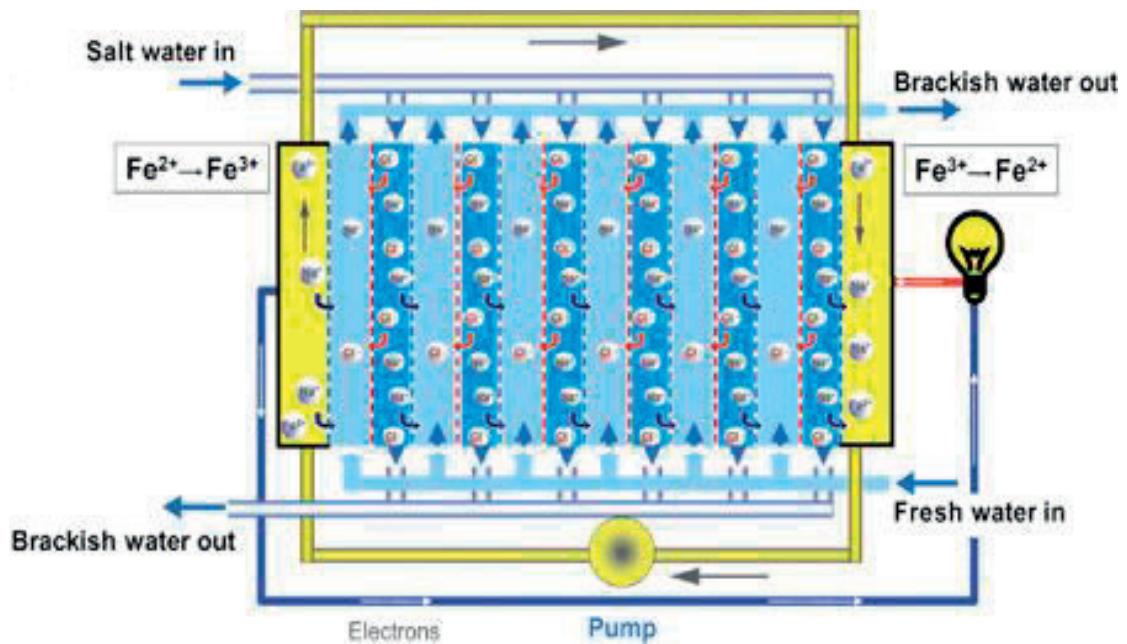


Figure 5.1. Reverse Electro Dialysis (RED): generating blue energy with membranes. RED utilizes the electro potential arising when ion-selective permeable membranes separate electrolyte solutions of different concentrations. Two types of membranes (cation selective and anion selective) are used in this system which can separate positive and negative ions and then generate electricity. Power generation by mixing seawater and river water in this advanced way has no fuel costs and no emissions except brackish water. This technology is under commercialization by Redstack in Netherland[185].

However, the problem of RED's economic feasibility lies on the cost of the membrane which is also directly linked to its efficiency and power density. Therefore, making and identifying new membranes become the central challenge. To this end, both organic and inorganic membranes have been developing for many years. From a fundamental point of view, measuring the performance of the membrane could largely

benefit from identifying each parameter using a single pore system which avoids averaging over many pores with distributed parameters.

5.2. Electric conductance and surface charge of MoS₂ nanopores

To gain a better insight into the surface properties of the MoS₂ nanopores, we first characterized the ionic transport properties of MoS₂ nanopores under various ionic concentration and pH conditions, which can provide information on the surface charge of the MoS₂ nanopore. **Figure 5.2 a** shows I-V characteristics of MoS₂ nanopores with various diameters. Large pore conductance originates from the ultrathin membrane. The conductance also depends on salt concentration (**Figure 5.2 b**) and shows saturation at low salt concentrations which is a signature of the presence of surface charge on the nanopore[177].

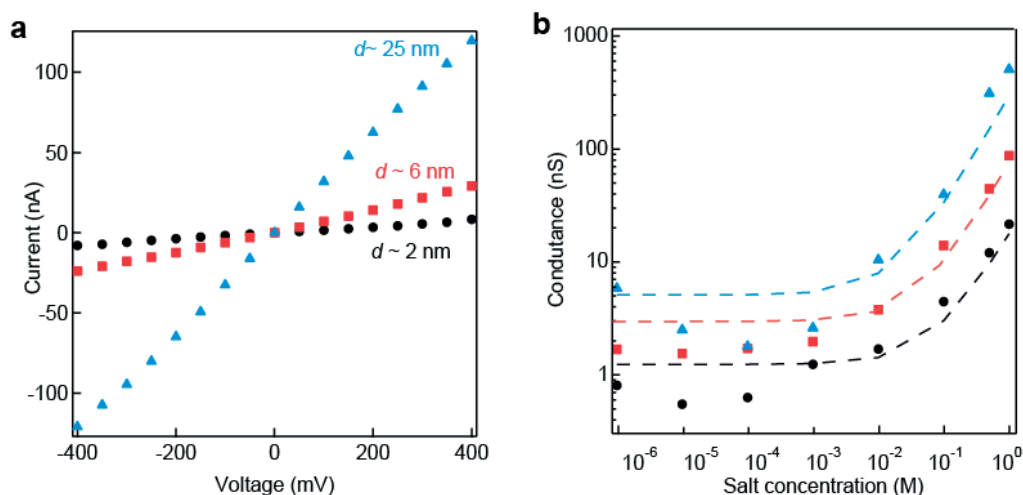


Figure 5.2. a. Electrical conductance and chemical reactivity of the MoS₂ nanopore. Current-voltage response of MoS₂ nanopores with different pore sizes (2.6 nm, 7 nm and 25 nm) in 1 M KCl. **b.** Conductance as a function of salt concentration of a 25 nm MoS₂ nanopore at pH 6. extracted the surface charge value by fitting to conductance model proposed by Lee et al is found to be -0.024 C m^{-2} , -0.053 C m^{-2} , -0.088 C m^{-2} for 2 nm, 6 nm, and 25 nm pore, respectively.

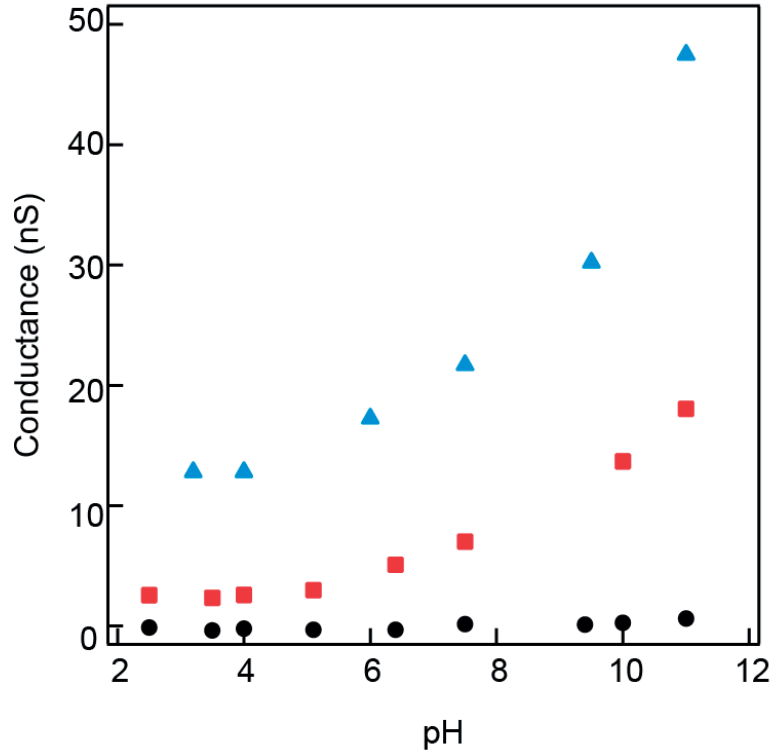


Figure 5.3. Conductance as a function of pH for 10 mM KCl for a 2 nm, 6 nm, and 25 nm pore. Pore thickness, 0.7 nm.

The predicted pore conductance (G) taking into account surface charge (Σ) contribution is given by[186],

$$G = \kappa_b \left[\frac{4L}{\pi d^2} \times \frac{1}{1 + 4 \frac{l_{Du}}{d}} + \frac{2}{\alpha d + \beta l_{Du}} \right]^{-1} \quad (5-1)$$

where κ_b is the bulk conductivity; L is the pore length, d is the pore diameter; l_{Du} is the *Dukhin length* which can be approximated by $\frac{|\Sigma|/e}{2c_s}$; e is the elementary charge and c_s is the salt concentration; α is a geometrical prefactor that depends on the model used ($\alpha=2$)[186]; β can also be approximated to be 2 to obtain the best fitting agreement[186]. As shown from the fitting results in **Figure 5.2 b**, a surface charge value of -0.024 C m^{-2} , -0.053 C m^{-2} , -0.088 C m^{-2} is found for three size pores of 2 nm, 6 nm and 25 nm at pH 5, respectively. This result is comparable to the recently

reported charge of graphene nanopores (-0.039 C m^{-2})[187] and nanotubes (-0.025 C m^{-2} to -0.125 C m^{-2})[79] at pH 5. The surface charge density can be further modulated by adjusting pH to change the pore surface chemistry. **Figure 5.3** shows the pH dependence of the pore conductance in 10 mM KCl. The conductance increases with the increase of pH, suggesting the accumulation of more negative surface charges in MoS₂ nanopore. The simulated conductance, shown in **Figure 5.4**, is linearly proportional to surface charge value obtained from equation 5-1, thus pH changes could significantly improve the surface charge up to the range of 0.3 to 0.8 C m⁻². The chemical reactivity of MoS₂ to pH is also supported by previously reported zeta potential measurements on MoS₂[188]. However, similar to other nanofluidic systems[79, 187], we also note that the surface charge density varies from pore to pore, which means that different pores can have disparate values of pK_a (reaction constant) due to various combinations of Mo and S atoms[169] at the edge of the pore, as illuminated by molecular dynamics simulations performed in the context of water desalination[189].

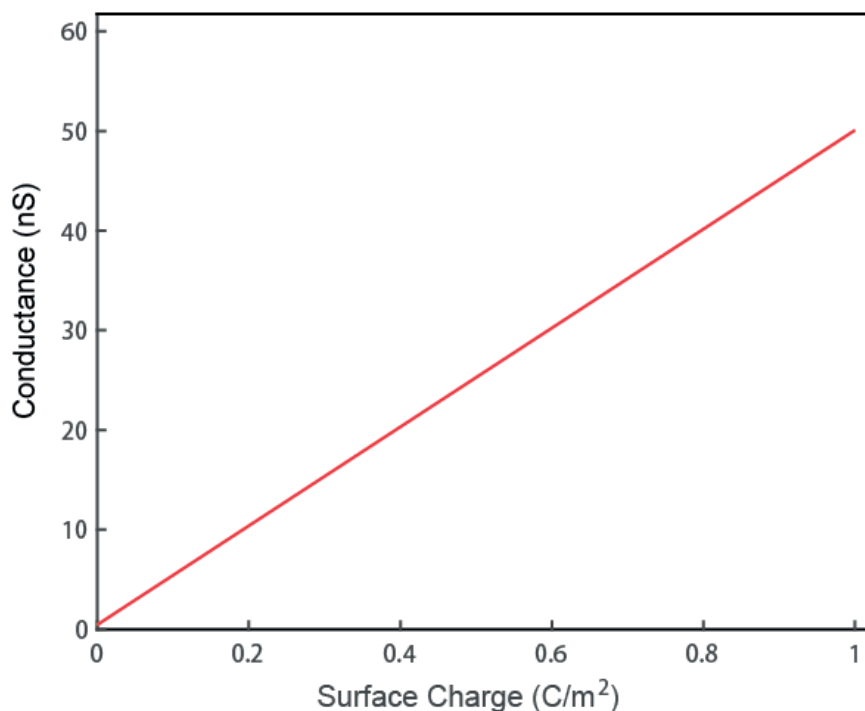


Figure 5.4. Simulated conductance of a 6 nm nanopore as a function of pore surface charge. The ionic concentration is 10 mM. Pore thickness, 0.7 nm.

Chapter 5. Nanofluidics: ultimate osmotic power generation with 2D membranes

In conclusion, this section demonstrates the surface charge properties of MoS₂ nanopore and sets the stage of cation ion selectivity.

5.3. Osmotic power conversion measured in MoS₂ nanopores

The key task for RED is to search for new membranes and many efforts have been made using microfabricated nanofluidic devices. Ionic transport measurements through boron nitride nanotubes suggested a giant osmotically induced electric currents generated by salt gradients[79]. The power density from RED process directly relates to the membrane thickness. Since water transport through a membrane scales inversely with the membrane thickness, membranes from two dimensional materials are expected to be the most attractive due to their atomic scale thickness. However, due to challenges in making non-leaky freestanding two-dimensional membranes, this ideal membrane has not realized so far. This section reports the conversion of osmotic energy into electric power using nanopores made in a single-layer MoS₂ membrane.

Compared to graphene, MoS₂ nanopores have already demonstrated better water transport behavior[98, 169] due to enriched hydrophilic surface sites (molybdenum) after TEM irradiation[190] or electrochemical oxidation[97]. In addition, recent molecular dynamics simulations have suggested the potential of using MoS₂ nanopores for water desalination[189]. With such an atomic-thick nanopore in a salt gradient system, we are able to experimentally generate up to nanowatts of power from a single pore and by exploiting parallelization, the estimated power density can reach up to 10^6 W m^{-2} , 2 to 3 orders of magnitudes higher than previously reported results with nanotubes[79] and 6 orders of magnitudes greater than in systems based on other known membranes[191].

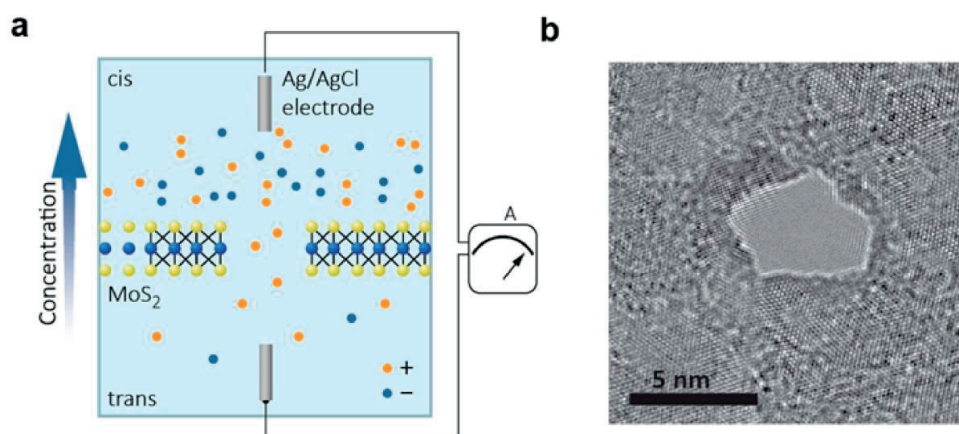


Figure 5.5. Operation schematic of osmotic energy harvesting with MoS₂ nanopores. **a.** (left) Solutions with different concentrations are separated by a 0.65 nm thick MoS₂ nanopore membrane. An ion flux driven by chemical potential (voltage, concentration, liquid-liquid junction, pH) through the pore is screened by the negatively charged pore, forming a diffusion current composed of mostly positively charged ions. **b.** Example of a TEM-drilled 5 nm MoS₂ nanopore.

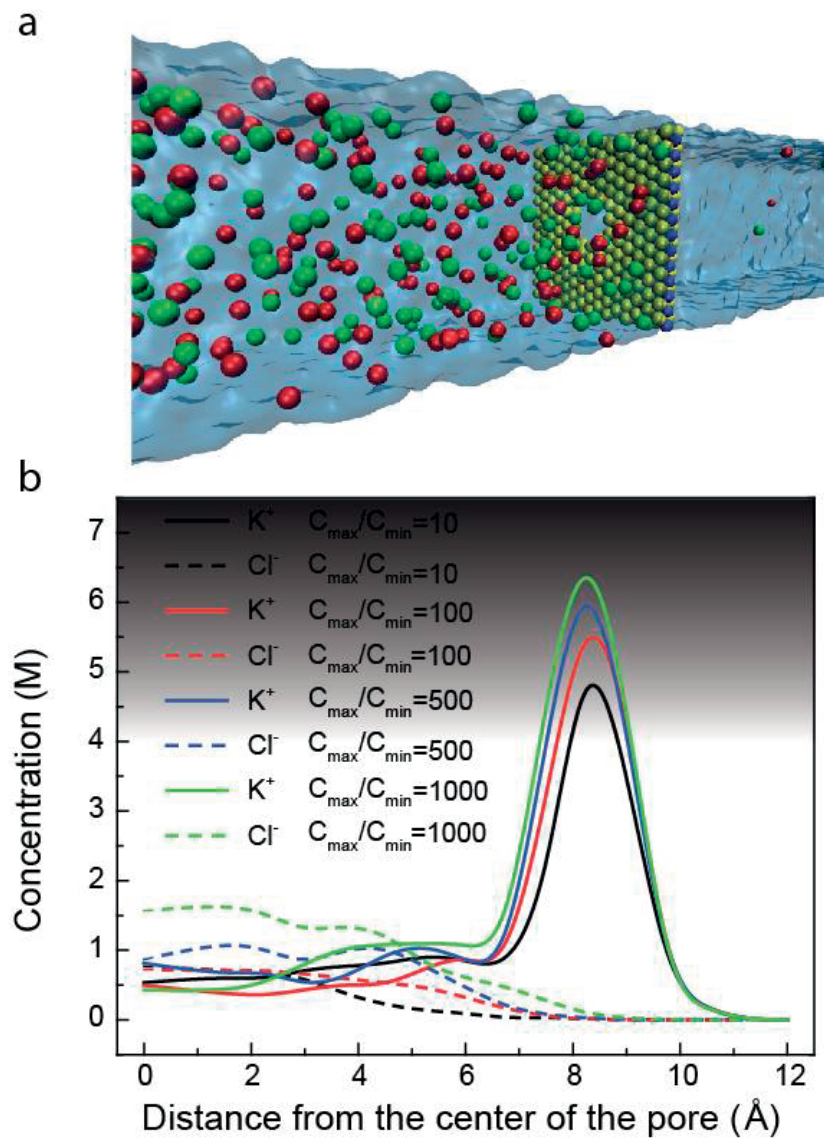


Figure 5.6. a). Schematic of a typical simulation box use in molecular dynamics simulations. **b).** MD simulated potassium and chloride concentrations as a function of the radial distance from the center of the pore for single and multi-layer membranes. The region near the charged wall of the pore is representative of the ionic double layer.

The potential is generated by separating two reservoirs containing potassium chloride (KCl) solutions with different concentrations with a freestanding MoS₂ membrane into which a single nanopore has been introduced[98]. A chemical potential gradient arises at the interface of these two liquids at a nanopore in a 0.65 nm thick single-layer MoS₂ membrane and drives ions spontaneously across the nanopore, forming an

Chapter 5. Nanofluidics: ultimate osmotic power generation with 2D membranes

osmotic ion flux towards equilibrium state, as shown in **Figure 5.5 a**. The presence of surface charges on the pore screens the passing ions by their charge polarity and thus results in a net measurable osmotic current, known as reverse electro dialysis[191]. This cation selectivity can be better understood by analyzing the concentration of each ion type (potassium and chloride) as a function of the radial distance from the center of the pore, as shown in the molecular dynamics results **Figure 5.6**. MoS₂ nanopores were fabricated either by TEM[98] (**Figure 5.5 b**) or by the recently demonstrated electrochemical reaction (ECR) technique[97]. With a typical nanopore diameter in the 2-25 nm range, a stable osmotic current can be expected due to the long time required for the system to reach its equilibrium state. The osmotic current and voltage across the pore were measured by using a pair of Ag/AgCl electrodes to characterize the current-voltage response of the nanopore.

We introduced the chemical potential gradient system by using different KCl concentrations, namely, the concentration gradient system[79]. The concentration gradient ratio is defined as C_{cis}/C_{trans} , where C_{cis} is KCl concentration in the *cis* chamber and C_{trans} in the *trans* chamber, ranging from 1 mM to 1 M. The highly negatively charged surface selectively passes the ions by their polarity (in this case potassium ions), resulting in a net positive current. By measuring the I-V response of the pore in the concentration gradient system, **Figure 5.7**, we can measure the short-circuit current (I_{sc}) corresponding to zero external bias while the osmotic potential can be obtained from the open-circuit voltage (V_{oc}). The pure osmotic potential and current can be then obtained by subtracting the contribution from electrode-solution interface at different concentrations which follows the Nernst equation[79, 184], as shown in **Figure 5.8** and **Table 5-1**.

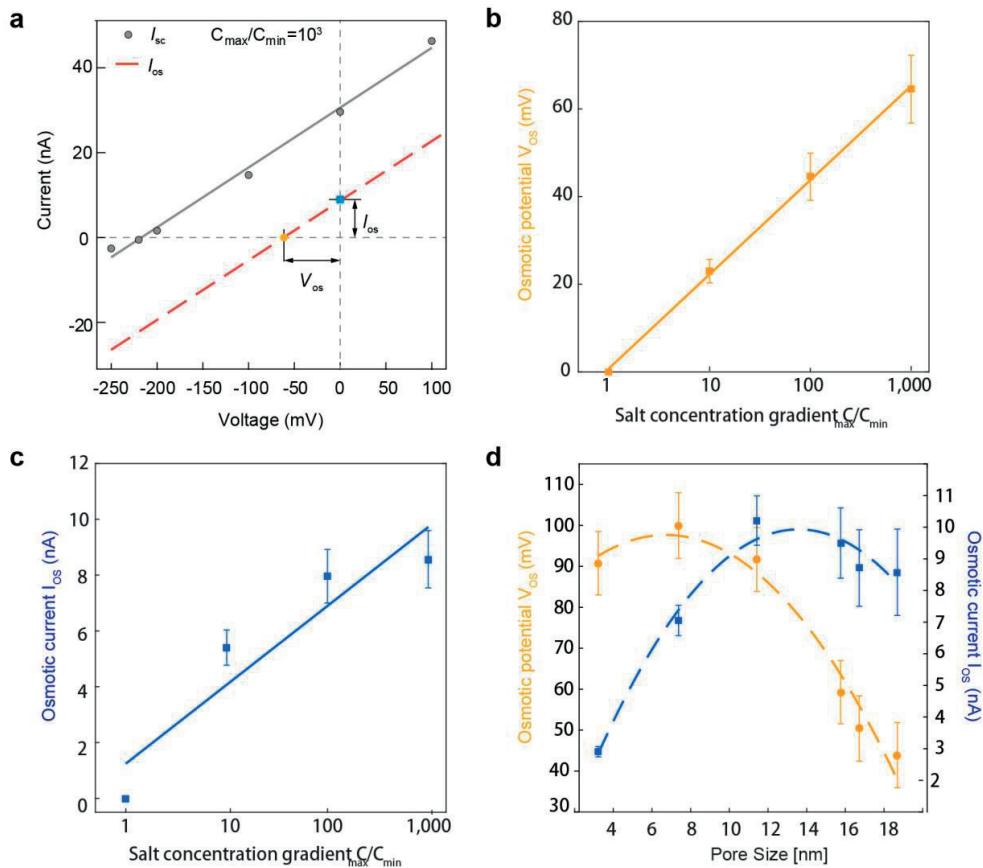


Figure 5.7. Osmotic power generation. **a.** Current voltage characteristics for a 15 nm large nanopore in the salt gradient condition. Concentration in the *cis* chamber $C_{cis} = 1$ M KCl, and concentration in the *trans* chamber $C_{trans} = 1$ mM KCl. Contribution from the redox reaction on the electrodes is subtracted. I_{sc} and V_{oc} are short circuit current and open circuit voltage. Red dashed line represents osmotic current. **b.** Generated osmotic open circuit voltage, as a function of salt gradient. C_{max} is set to be 1 M KCl and C_{min} is tunable from 1 μ M to 1 M KCl. Solid line fits the linear part to the proposed equation 5-2. **c.** Osmotic short circuit current versus salt gradient. The decrease of current to higher salt gradient is due to the increased bulk resistance at low salt concentration. **d.** Osmotic potential and current as a function of pore size. Dashed lines (guide to eye) show the trend as the pore size is changed.

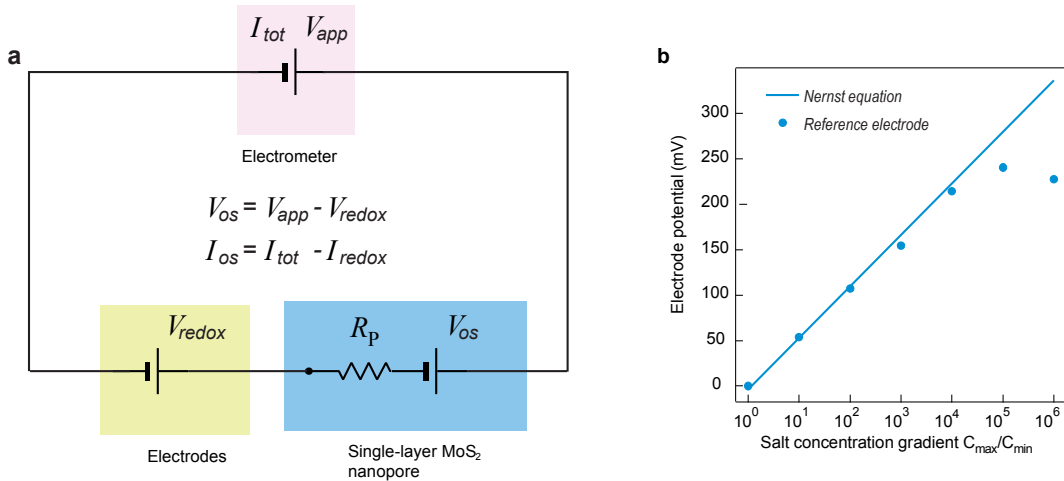


Figure 5.8. **a**, Schematic diagram that details the contributions to the overall measured current. Osmotic contribution is obtained by subtracting electrode potential contribution. **b**. Electrode contribution: Values obtained from *Nernst equation* (line) and measured electrode redox potential difference by reference electrode (dots).

Log C_{max}/C_{min}	$I_{measured}$, nA	$V_{measured}$, mV	E_{redox} , mV	V_{os} , mV	I_{os} , nA
0	Set to 0				
1	18.2	78.2	53.7	24.5	5.7
2	27.2	150.2	107.2	43.0	7.8
3	30.6	216.8	154.1	62.7	8.8
4	20.7	276.0	214.2	61.8	4.6
5	14.5	322.2	240.2	82.0	3.7
6	10.9	311.7	227.0	84.7	3.0

Table 5-1. Data extracted from measurements by subtracting the electrode contribution

The osmotic potential (up to 90 mV) is proportional to the concentration gradient ratio (**Figure 5.7 a**). The osmotic current shares a similar trend with V_{os} until a concentration gradient ratio of 10^3 is reached, where the highest current is obtained, **Figure 5.7 c**. The measured osmotic energy conversion is also pH dependent, as shown in **Figure 5.9**. Increase of pH leads to higher generated voltage and current, suggesting the importance of surface charge on ion-selective process.

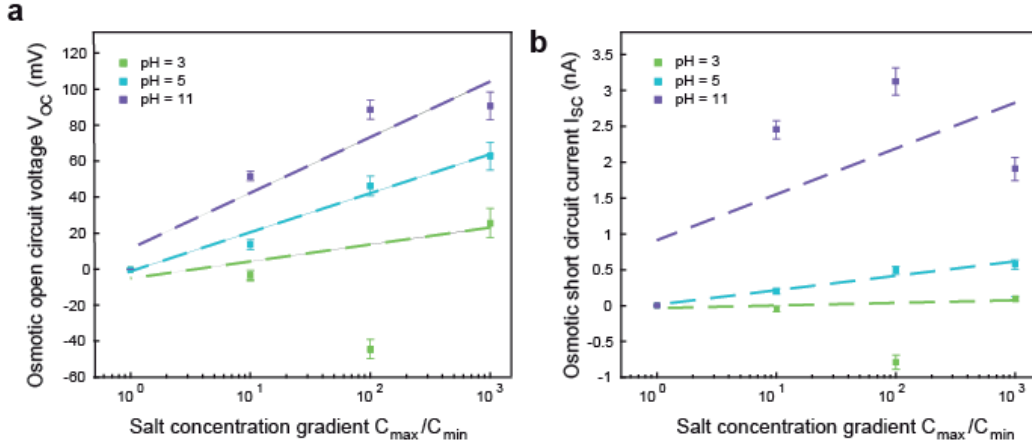


Figure 5.9. Power generation for a 4 nm pore under different pH conditions (3, 5, 11) and under different concentration gradient conditions. We noticed the power generation at pH 3 is very low and may fluctuate to negative which indicates the pore charge is relatively low and a possibility for the point at negative voltage is the fluctuation to positive pore surface charges.

The extracted potential is the diffusion potential and arises from the differences in the diffusive fluxes of positive and negative ions, due to the ion-selective property of the pore where cations diffuse more rapidly than anions (**Figure 5.6**). The diffusion potential, V_{diff} can be described as[184],

$$V_{diff} = S(\Sigma)_{is} \frac{RT}{F} \ln \left[\frac{a_{KCl}^{cis}}{a_{KCl}^{trans}} \right] \quad (5-2)$$

where $S(\Sigma)_{is}$ is the ion selectivity[192] for the MoS₂ nanopore (equal 1 for the ideal cation selective case and 0 for the non-selective case), defined as $S(\Sigma)_{is} = t_+ - t_-$, where t_+ and t_- are the transference numbers for positively and negatively charged ions respectively. F , R , T are the Faraday constant, the universal gas constant, and the temperature while a_{KCl}^{cis} and a_{KCl}^{trans} are activities of potassium ions in *cis* and *trans* solutions. By fitting the experimental data presented in **Figure 5.7** to equation 5-2, the ion selectivity coefficient $S(\Sigma)_{is}$ is found to be 0.4, suggesting efficient cation selectivity. This is because the size of our nanopores lies in the range where the electrical double layer overlap can occur inside the pore[193] since the Debye length $\lambda_B = 10$ nm for 1 mM KCl. As shown in **Table 5-2**, the ion selectivity depends on the Debye length and with the combination of 10 mM/1 mM in a 5 nm pore, the ion

Chapter 5. Nanofluidics: ultimate osmotic power generation with 2D membranes

selectivity approaches nearly 1, presenting the conditions for the ideal cation selectivity[192].

C_{\min}/C_{\max}	V_{measured} , mV	E_{redox} , mV	V_{os} , mV	Ion selectivity
1mM/10mM	100.6	46.9	53.7	0.92
10mM/100mM	104.4	53.5	50.9	0.86
10mM/1M	153.3	107.2	46.1	0.78
1mM/100mM	183.0	100.4	82.6	0.7
100mM/1M	67.3	53.7	13.6	0.23

Table 5-2. Ion selectivity at different salt gradient conditions. the ion selectivity also depends on the Debye length when the concentration gradient ratio is fixed and with the combination of 10 mM/1 mM in a 5 nm pore, the ion selectivity approaches nearly 1, indicating the ideal cation selectivity.

To further test the cation-selective behavior of the pore, we also investigated the relation between power generation and the pore size at fixed concentration gradient. As shown in **Figure 5.7 c** and **Figure 5.10**, small pores display better voltage behavior, indicating the better performance on ion selectivity.

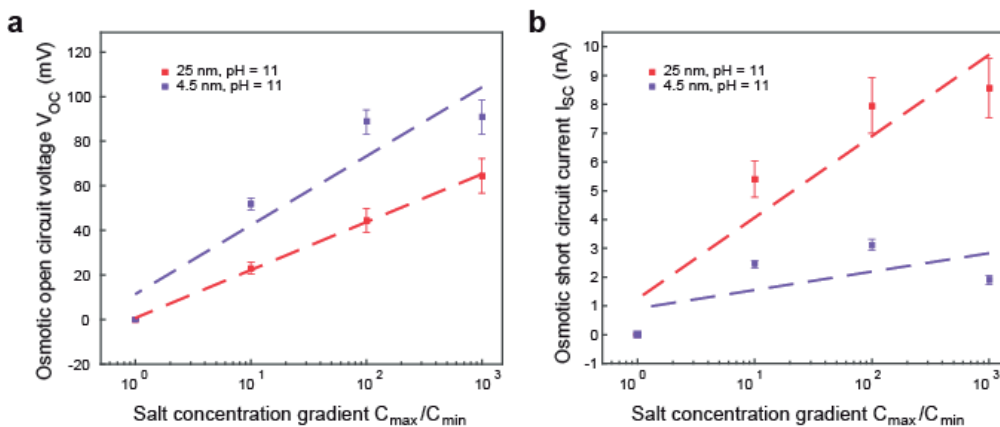


Figure 5.10. Power generation for two pores (4 nm and 15 nm) at pH 11 and under different concentration gradient conditions.

The ion selectivity $S(\Sigma)_{is}$ decreases from 0.62 to 0.23 as the pore size increases. It has been proven that the net diffusion current only stems from the charge separation and concentration distribution within the electrical double layer[194] and therefore, the total current can be expected to increase more rapidly within the double layer

Chapter 5. Nanofluidics: ultimate osmotic power generation with 2D membranes

overlap range compared to larger pore sizes (**Figure 5.7 d**). The slight decrease might be attributed to reduced local concentration gradient in larger pore and also to probable overestimation of the redox potential subtraction.

Fabrication of the large scale porous membranes with porosity (25% to 95%) using electrochemical etching technique has been already demonstrated[195]. Assuming a single-layer MoS₂ membrane with homogeneous pore size of 10 nm and porosity of 30% results in a pore density of $4 \times 10^{15}/\text{m}^2$. By exploiting parallelization with such nanoporous membranes, the estimated power density would reach $10^6 \text{ W}/\text{m}^2$ with KCl salt gradient. These values exceed by 2 to 3 orders of magnitudes results obtained with boron nitride nanotubes[79] and are million times higher than reverse electro dialysis with classical exchange membranes[191], as detailed in **Table 5-3**.

Reverse electro dialysis cells	Power density(W/m^2)	Membrane thickness
Weinstrin and Leitz, 1976[196]	0.17	1 mm
Audinos, 1983[197]	0.40	3 mm
Turek and Bandura, 2007[198]	0.46	0.19 mm
Suda et al, 2007[199]	0.26	1 mm
Veerman et al, 2009[200]	0.95	0.2 mm
Kim et al, 2010[184]	7.7	0.14 mm
Siria et al, 2013[79]	4000	1 μm
This work	10^6	0.65 nm
Multilayer MoS₂ (Simulations)	30000	7.2 nm

Table 5-3. Membrane thickness vs power generation. Direct comparison of osmotic power generation using various membranes clearly shows the thickness scaling.

5.4. Computational nanofluidics model

The current can be calculated using either a continuum based Poisson-Nernst-Planck (PNP) model or molecular dynamics simulations. The measured dependence of the diffusion voltage and osmotic current as a function of the concentration ratios (**Figure 5.7 b, c**) is well captured by both computational models (**molecular dynamics prediction in Figure 5.12** and **continuum analysis in Figure 5.13**). In addition to depletion of concentration gradient, the non-monotonic response to pore size (**Figure**

5.7 d) is also predicted by continuum based PNP model (**Figure 5.17**), as a result of decrease of ion selectivity. The theoretical model highlights two important contributions playing key roles for achieving efficient power generation from a single-layer MoS₂ nanopore: pore thickness, corresponding to the atomic scale thickness of the MoS₂ membrane and the possibility to modulate the surface charge. Particularly in high pH range, the cation-selectivity of MoS₂ pores increases as the pH is increased due to accumulation of negative charges. In order to gain further insight to the thickness scaling, we first verified the pore conductance relation proposed in equation (5-1) using molecular dynamics (**Figure 5.14**). Interestingly, the ion mobility is also found to scale inversely with membrane thickness (**Figure 5.15**) and may conform to previous observations[201]. We then performed molecular dynamics simulation of multilayer membranes of MoS₂ to investigate the power generated by those membranes. We observe a strong decay of the generated power as the number of layers is increased (**Figure 5.16**), indicating the ultimate osmotic power generation in 2-dimensional membranes.

5.4.1. Computational simulations: Molecular dynamics and continuum models

Molecular Dynamics simulations (MD) were performed using the LAMMPS package[202]. A MoS₂ membrane was placed between two KCl solutions as shown in **Figure 5.11**. A fixed graphene wall was placed at the end of each solution reservoir. A nanopore was drilled in MoS₂ by removing the desired atoms. The accessible pore diameter, considered in most of the simulations, is 2.2 nm with a surface charge density of 2.93 e nm^{-2} . The system dimensions are $6 \text{ nm} \times 6 \text{ nm} \times 36 \text{ nm}$ in x, y and z, respectively. The SPC/E water model was used and the SHAKE algorithm was applied to maintain the rigidity of each water molecule. The Lennard Jones (LJ) parameters are tabulated in **Table 5-4**. The LJ cutoff distance was 12 Å. The long range interactions were computed by the Particle Particle Particle Mesh (PPPM)[203]. Periodic boundary conditions were applied in the x and y directions. The system is non-periodic in the z direction. For each simulation, first the energy of the system was minimized for 10,000 steps. Next, the system was equilibrated in NPT ensemble for 2 ns at a pressure of 1 atm and a temperature of 300 K to reach the equilibrium density of water. Graphene and MoS₂ atoms were held fixed in space during the simulations. Then, NVT simulations were performed where the temperature was maintained at 300 K by using the Nosè-Hoover thermostat with a time constant of 0.1 ps[204, 205].

Chapter 5. Nanofluidics: ultimate osmotic power generation with 2D membranes

Trajectories of atoms were collected every picosecond to obtain the results. For accurate mobility calculations, however, the trajectories were stored every ten femtoseconds.

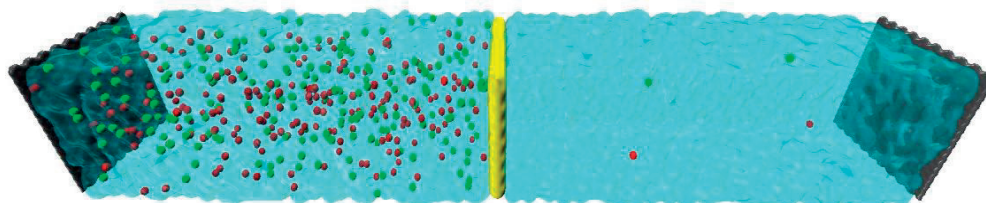


Figure 5.11. Schematic of a typical simulation box consisting of a MoS₂ sheet (in yellow), water (transparent blue), ions (in red and green) and two graphene walls (in gray)

Interaction	σ [Å]	ϵ [kcal mol ⁻¹]	Charge [e]
C-C[206]	3.3900	0.0692	0.0000
Mo-Mo[207]	4.2000	0.0135	0.6000
S-S ^[207]	3.1300	0.4612	-0.3000
O-O[206]	3.1656	0.1554	-0.8476
H-H[206]	0.0000	0.0000	0.4238
Mo-O	3.9960	0.0581	-----
Mo-S	3.4150	0.2824	-----
K-K[208]	2.8400	0.4300	1.0000
Cl-Cl[208]	4.8305	0.0128	-1.0000
C-O[209]	3.4360	0.0850	-----
C-H[209]	2.6900	0.0383	-----
Rest	Obtained by Lorentz-Berthelot rule.		

Table 5-4. The Lennard-Jones parameters and charges.

We also use continuum based 2D Poisson-Nernst-Planck model to explain the non-monotonic characteristics of the osmotic short-circuit current (I_{sc}) with increase in the salinity gradient ratio across the *Cis* and *Trans* reservoirs. In this model, we neglect the contribution of H^+ and OH^- ions in the current calculation as its concentration is much lower compared to the bulk concentration of the ionic species. Hence, the water dissociation effects are not considered in the numerical model.

Chapter 5. Nanofluidics: ultimate osmotic power generation with 2D membranes

Further, we assume that the ions are immobile inside the Steric layer and do not contribute to the ionic current. We also do not model the Faradaic reactions occurring near the electrode. Finally, we also assume that the convective component of current originating from the fluid flow is negligible and does not contribute to the non-monotonic osmotic current observed in the experiments. We validate this assumption by performing detailed all atom molecular dynamics simulations and predict the contribution of electroosmotic velocity in comparison to the drift velocity of the ions. Under these assumptions, the total flux of each ionic species (Γ_i) is contributed by a diffusive component resulting from the concentration gradient and an electrophoretic component arising due to the potential gradient as given by,

$$\Gamma_i = -D_i \nabla c_i - \Omega_i z_i F c_i \nabla \phi \quad (5-3)$$

where F is Faraday's constant, z_i is the valence, D_i is the diffusion coefficient, Ω_i is the ionic mobility, c_i is the concentration of the i^{th} species and ϕ is the electrical potential. Note that the ionic mobility is related to the diffusion coefficient by Einstein's relation[210], $\Omega_i = \frac{D_i}{RT}$, where R is the ideal gas constant and T is the thermodynamic temperature. The mass transport of each ionic species is,

$$\frac{dc_i}{dt} = -\nabla \cdot \Gamma_i \quad (5-4)$$

The individual ionic current (I_i) across the reservoir and the pore is calculated by integrating their respective fluxes over the cross-sectional area, i.e.,

$$I_i = \int z_i F \Gamma_i dS \quad (5-5)$$

The total ionic current at any axial location is calculated as, $I = \sum_{i=1}^m z_i F \Gamma_i dS$, where S is the cross-sectional area corresponding to the axial location and m is the number of ionic species. In order to determine the electric potential along the system, we solve the Poisson equation,

$$\nabla \cdot (\epsilon_r \nabla \phi) = -\frac{\rho_e}{\epsilon_o} \quad (5-6)$$

where ϵ_o is the permittivity of free space, ϵ_r is the relative permittivity of the medium and ρ_e is the net space charge density of the ions defined as,

Chapter 5. Nanofluidics: ultimate osmotic power generation with 2D membranes

$$\rho_e = F \sum_{i=1}^m z_i F c_i \quad (5-7)$$

We provide the necessary boundary conditions for the closure of the problem. The normal flux of each ion is assumed to be zero on all the walls so that there is no leakage of current. To conserve charge on the walls of the pore, the electrostatic boundary condition is given by,

$$\mathbf{n} \cdot \nabla \phi = \frac{\sigma}{\epsilon_0 \epsilon_r} \quad (5-8)$$

where \mathbf{n} denotes the unit normal vector (pointing outwards) to the wall surface and σ is the surface charge density of the walls. The bulk concentration of the *Cis* reservoir is maintained at C_{max} and the bulk concentration on the *Trans* reservoir is maintained at C_{min} . As we are interested to understand the osmotic short-circuit current, I_{sc} , we do not apply any voltage difference across the reservoirs. Thus, the boundary conditions at the ends of the *Cis* and *Trans* are specified as:

$$c_i = C_{max}, \phi = 0 \quad (5-9)$$

$$c_i = C_{min}, \phi = 0 \quad (5-10)$$

The coupled PNP equations are numerically solved using the finite volume method in OpenFOAM[211] (OpenField Operation and Manipulation). The details regarding the solver implementation is discussed in our earlier works[212-214]. The simulated domain consists of a MoS₂ nanopore of length $L_n = 0.6 \text{ nm}$ and diameter d_n varying from 2.2 nm to 25 nm . The simulated length of the reservoir is $L_{Cis} = L_{Trans} = 100 \text{ nm}$ and the diameter of the reservoir is 50 nm . Potassium chloride buffer solution is used in the simulation. The bulk concentration of the *Cis* reservoir was fixed at 1 M and the concentration in the *Trans* reservoir was systematically varied from 1 mM to 1 M . The simulation temperature is $T = 300 \text{ K}$. The bulk diffusivities of K^+ and Cl^- are $1.96 \times 10^{-9} \text{ m}^2/\text{s}$ and $2.03 \times 10^{-9} \text{ m}^2/\text{s}$. The dielectric constant of the aqueous solution is assumed to be, $\epsilon_r = 80$. We also assume zero surface charge density on the walls of the reservoir, as the reservoir is far away from the nanopore to have an influence on the transport. Unless otherwise stated, the charge on the walls of the MoS₂ nanopore is assumed to be $\sigma_n = -0.4694 \text{ C/m}^2$, consistent with the surface charge calculated from our MD simulations.

5.4.2. Results and discussion

Chapter 5. Nanofluidics: ultimate osmotic power generation with 2D membranes

Using MD, we applied different ionic concentration ratios across a single-layer MoS₂ membrane. The KCl concentration in the *cis* reservoir is always kept at 1 M while changing the concentration in the *trans* reservoir (0.1, 0.01, 0.002 and 0.001 M) to achieve different salinity ratios of 10, 100, 500 and 1000. The current is plotted for different applied electric fields as shown in **Figure 5.12 a**. As discussed in the manuscript, the possible explanation for the experimentally observed non-monotonic short-circuit current is due to the competition between the diffusion process (dominant exchange process) and the migration of ions owing to the induced Donnan potential induced near the interfaces of the nanopore. The potential is induced owing to the cation selectivity of the pore. The potassium selectivity coefficient is defined as

$\frac{J_{K^+} - J_{Cl^-}}{J_{K^+} + J_{Cl^-}}$ where J_{K^+} and J_{Cl^-} are the flux of potassium and chloride ions,

respectively. The flux of each ion type depends on its concentration and velocity inside the pore. Now, using MD simulations, we confirmed the cation selectivity of the negatively charged pore by analyzing the concentration of each ion type (potassium and chloride) as a function of the radial distance from the center of the pore (**Figure 5.12 b**). As expected, the potassium ions (counter-ions) are attracted to the charged surface of the pore, while the chloride ions (co-ions) are repelled from the surface. This results in an electrical double layer with a higher concentration of the counter-ions. The selectivity of the pore as well as the individual ionic flux is tabulated for different ratios in **Table 5-5**. The selectivity of the pore decreases with increase in the saline concentration ratio due to an increase in the co-ion concentration inside the pore as shown in **Figure 5.12 b**.

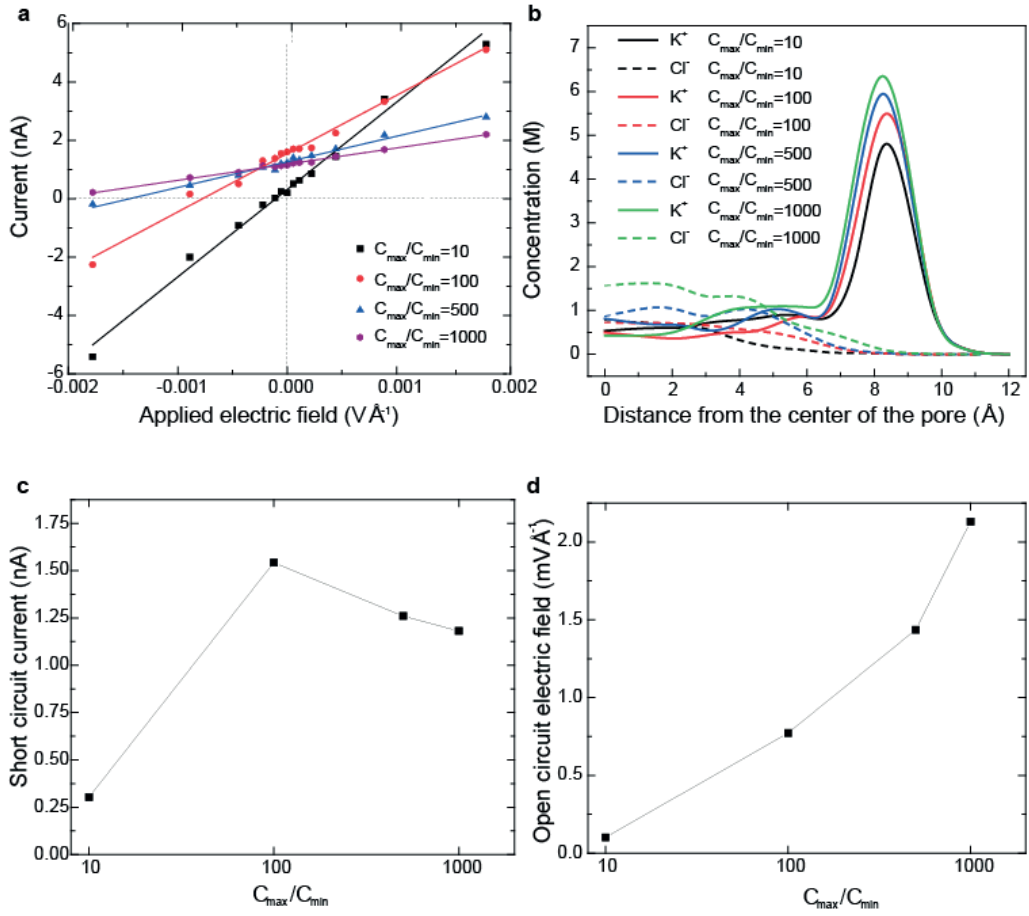


Figure 5.12. **a.** Current as a function of the applied electric field for a single-layer MoS₂ for different concentration ratios. **b.** Potassium and chloride concentrations as a function of the radial distance from the center of the pore for different concentration ratios. **c.** Short circuit current as a function of the concentration ratio. **d.** Open circuit electric field as a function of the concentration ratio.

Concentration ratio	J_{K^+} [# / ns]	J_{Cl^-} [# / ns]	Potassium selectivity coefficient
10	2.34	0.34	0.7462
100	15.34	2.67	0.7034
500	12.67	2.34	0.6882
1000	10.34	2.00	0.6758

Table 5-5. The individual contribution of ions to the current and the potassium selectivity coefficient of the pore.

Chapter 5. Nanofluidics: ultimate osmotic power generation with 2D membranes

We also investigated the effect of osmotic flow of water on the currents by computing the area-averaged velocity (\hat{v}_{water}) of water inside the pore. \hat{v}_{water} ranges from 0.05 to 0.1 m s⁻¹ which is 1 to 2 orders of magnitude smaller than the averaged velocity of ions (total averaged velocity of ions - \hat{v}_{water}) inside the pore resulting in an insignificant contribution to current due the osmotic flow of water.

The short-circuit current and open-circuit electric field are plotted for different ratios in **Figure 5.12 c** and **Figure 5.12 d**, respectively. The non-monotonic short circuit current and monotonic increase in open circuit electric field with concentration ratio are qualitatively consistent to the experimental observations (**Figure 5.7**). To understand the mechanism behind the non-monotonic current characteristics, a continuum based analysis is carried out. **Figure 5.13 a** shows the variation of short-circuit current with different salinity gradient ratios. A non-monotonic variation in the short-circuit current is also captured from the continuum model. However, the continuum based PNP equations only qualitatively predicts the MD observations. This is because, in continuum calculations, we have assumed a constant mobility for each ion in the entire system while in MD the mobility increases (for a single-layer MoS₂) inside the pore resulting in a higher drift velocity of ions and, in turn, a higher migration and diffusive ionic current for MD.

To explain the mechanism, we calculate each component of flux inside the nanopore and understand the dominant exchange process. We have neglected the convective current contribution due to the fluid flow as the velocity of water is 1 to 2 orders of magnitude smaller than the velocity of ions from our MD calculations. Inside the nanopore, owing to the salinity concentration ratio of the reservoirs and the cation-selectivity of the pore, we observe dominant contribution of diffusive flux of potassium ions (counter-ions) in comparison to the diffusive flux of chloride ions. Furthermore, due to the nanopore cation-selectivity and predominant diffusion of potassium ions, we observe a build up of positive potential (Donnan potential) near the interface of nanopore and low concentration reservoir. Also, a negative potential is build up at the interface of nanopore and high concentration reservoir, as the chloride ions are blocked from entering into the pore. The net potential difference across the nanopore interface results in an induced electric field directed from low concentration interface region to high concentration interface region. This results in a migration of potassium ions (counter-ions) from low concentration nanopore interface to high

Chapter 5. Nanofluidics: ultimate osmotic power generation with 2D membranes

concentration nanopore interface and the chlorine ions (co-ions) in the opposite direction. We observe that the dominant exchange process inside the nanopore is always diffusion, however the contribution of migrational potassium flux (countering the diffusive flux of potassium ions) increases at high salinity concentration ratios. It is due to the competition of these two countering fluxes of potassium ions, we observe a non-monotonic short-circuit current in MoS₂ nanopores.

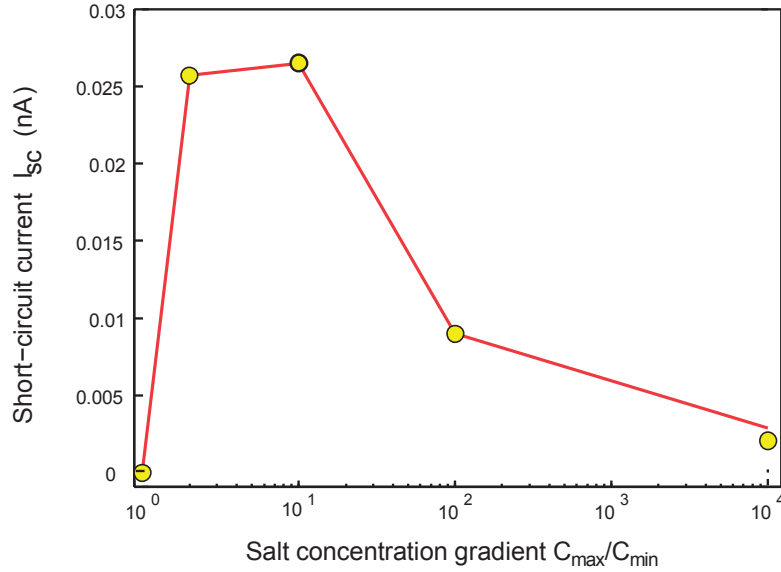


Figure 5.13. Variation of short-circuit current, I_{sc} . The diameter of the nanopore is $d_n = 2.2 \text{ nm}$.

We also considered the effect of membrane thickness on the power generation in our MD simulations. Different membranes of MoS₂ (single-layer, two-layer, three-layer, four-layer, six-layer and twelve-layer MoS₂) were created to first characterize the thickness effect on the conductance of the nanopores. For all the membranes, a symmetric concentration of 1 M KCl is applied. Also, we fixed the length of the reservoir, ($L_{reservoir} = 4 \text{ nm}$). With different layers of MoS₂, the overall length of the system (L) changes ($L = 2L_{reservoir} + L_{pore}$), so to have a consistent bias (ΔV) across all the systems we adjust the applied electric field (E) using $E = \frac{\Delta V}{L}$. Note, in molecular dynamics, the applied electric field is uniform in the entire system while in experiments, the electric field is mostly felt at the membrane. The I-V curves for all the membranes are plotted in **Figure 5.14 a**. From theory, conductance scales inversely with the thickness of the membrane; therefore, the conductance is plotted as

a function of the reciprocal thickness (t^{-1}) in **Figure 5.14 b**. The variation of conductance with inverse thickness is not linear as predicted by the classical theory. In addition to the thickness, ionic mobility also influences the conductance. **Figure 5.14 c** shows how the average mobility (averaged over the cross-section) of each ion inside the pore changes with the increase in the number of MoS₂ layers. There is a very sharp reduction in the mobility of potassium ions inside the pore of a multilayer MoS₂ compared to that of the single-layer membrane.

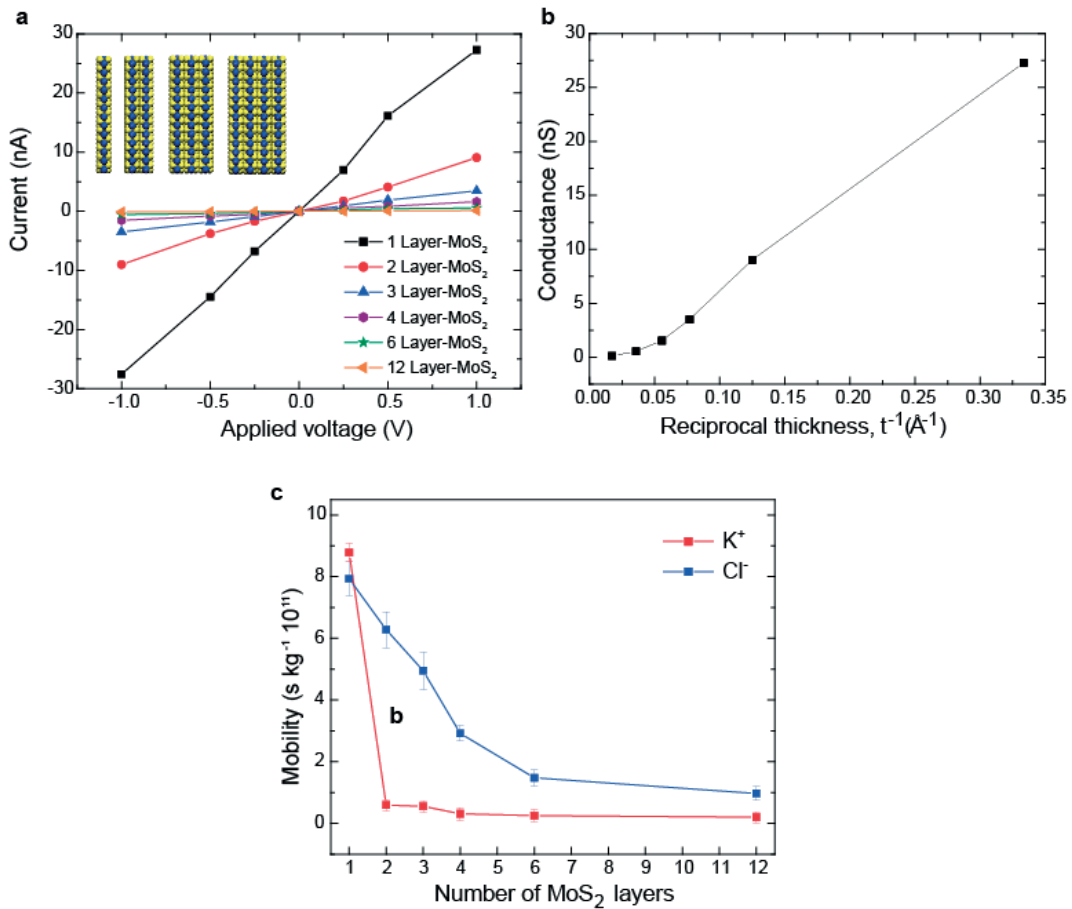


Figure 5.14. **a.** I-V curves for six membranes with different number of MoS₂ layers across a symmetric 1 M KCl solution. **b.** Conductance of the nanopore as a function of the reciprocal thickness of the membrane (t^{-1}). **c.** Average mobility of each ion for different layers of MoS₂ membranes.

The abrupt reduction of mobility is due to the fact that the counter-ions (potassium) are strongly absorbed to the charged surface of the multilayer pores. **Figure 5.15 a** shows the concentration of ions inside the pores for all the membranes. The

Chapter 5. Nanofluidics: ultimate osmotic power generation with 2D membranes

concentration of potassium ions increases significantly in the double layer (λ) near the wall. Based on the classical theory, the double layer ($\lambda = \sqrt{\frac{\epsilon_0 \epsilon_r RT}{2F^2 z^2 c_0}}$) for a symmetric monovalent electrolyte ($z_K = z_{Cl} = z = 1$) is calculated to be 0.308 nm assuming $c_0 \sim 1M$ concentration observed at the center of the pore. Because of the absorption, the mobility of ions decreases sharply within the λ layer. This reduction is also evident by looking at the residence time of potassium ions inside the λ layer (**Table 5-6**). The residence time increases for multilayer membranes compared to that of the single-layer membrane. In **Figure 5.15 b**, the mobility of ions is plotted as a function of the number of layers of MoS_2 . Within λ the mobility decreases sharply from a single layer to two layer and three layer MoS_2 . Beyond that the mobility remains constant at a much lower value compared to that of the single-layer MoS_2 . Outside λ , the mobility decrease is not as sharp, but the mobility in a single-layer is higher compared to multilayer MoS_2 .

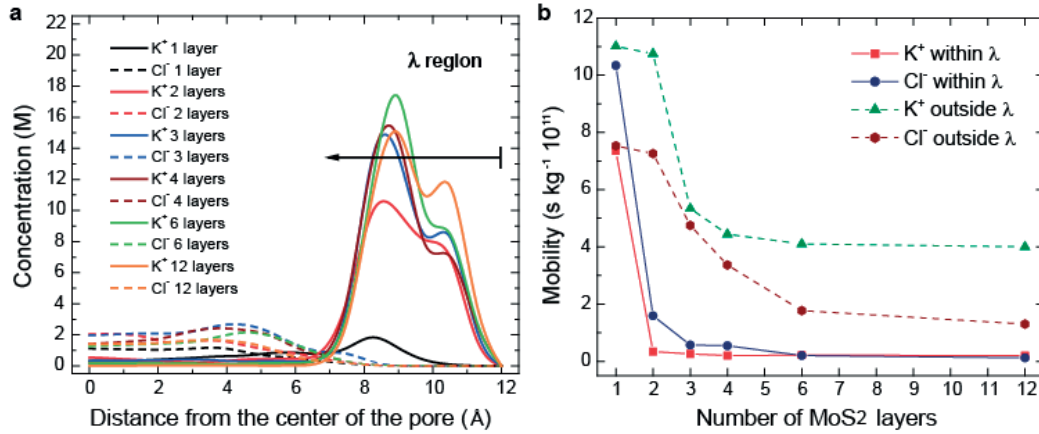


Figure 5.15. a. Potassium and chloride concentrations as a function of the radial distance from the center of the pore for single and multi-layer membranes. The λ region near the charged wall of the pore is representative of the ionic double layer. **b.** Mobility of each ion type within and outside the λ region for different layers of membranes.

Number of MoS_2 layers	Residence time of K^+ within λ [ns]
1	0.08
2	1.52
3	3.46

4	5.53
6	7.26
12	15>

Table 5-6. The residence time of potassium ions inside the λ layer at 1 V.

The effect of having multilayer membranes of MoS₂ on the power generated by these membranes was also studied by performing MD simulations. A concentration gradient of 1000 ($C_{max} = 1M$ and $C_{min} = 1mM$) is used across the multilayer membranes to obtain the open-circuit voltage as the maximum power is proportional to both the conductance and the square of open-circuit voltage. **Figure 5.16 a** shows the open-circuit electric field (E_{oc}) as a function of the number of layers in MoS₂. Once the open-circuit voltage ($V_{oc}=E_{oc}\cdot L$) and the conductance dependence on thickness are known, the power generated is estimated for multilayer MoS₂ membranes as a ratio of P_{max}^n to P_{max}^1 (n denotes number of layers) in **Figure 5.16 b**. A multilayer MoS₂ reduces the osmotic power substantially. For instance, the power for a twelve-layer MoS₂ is predicted to be only about 3% of that of the single-layer membrane.

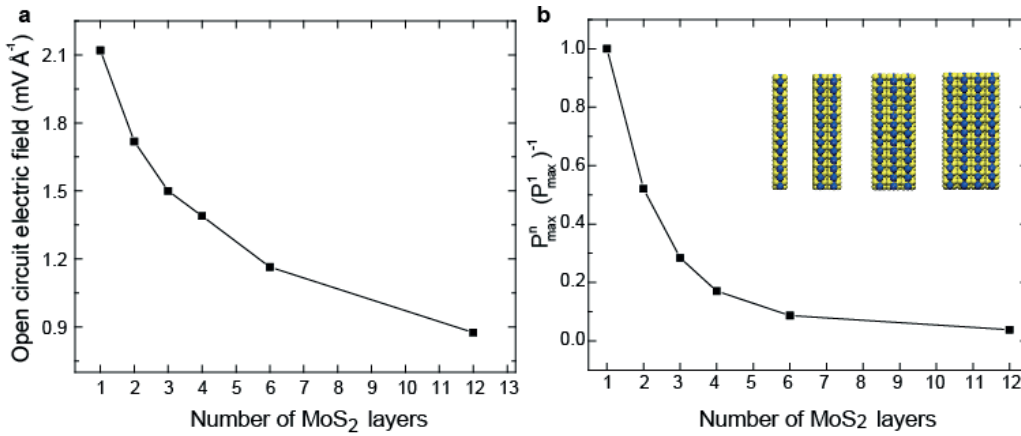


Figure 5.16. a. The open circuit electric field across the membrane for different number of MoS₂ layers. **b.** The ratio of the maximum power from multilayer membranes to the maximum power generated by a single-layer MoS₂.

Using our continuum model, we also investigate the effect of pore size on the short-circuit current. **Figure 5.17** shows the variation of short-circuit current with pore diameter. We observe a non-monotonic variation in the short-circuit current consistent with the experimental predictions. To understand this result, consider the extreme

Chapter 5. Nanofluidics: ultimate osmotic power generation with 2D membranes

limits of the pore diameter, i.e., $D_{pore} \rightarrow 0$ and $D_{pore} \rightarrow D_{reservoir}$ (no membrane). In the lower limit, ($D_{pore} \rightarrow 0$), we block the ions passing through the interface and hence, there is negligible diffusion of ions as the membrane diameter is zero and the induced electric field at the nanopore interface is small. This results in a no short-circuit current. In the upper limit ($D_{pore} \rightarrow D_{reservoir}$), the selectivity of the pore is lost and hence, the concentration of the ions inside the pore is almost equal to the bulk concentration and the system will equilibrate quickly, resulting in almost an equal and opposite diffusive flux of potassium and chloride ions. Further, the induced electric field at the nanopore interface is small owing to loss of ion selectivity. This results in a weak migrational flux of both the ions. Hence, the resulting short-circuit current is small. For other diameters between these extreme limits, we observe higher diffusive flux of potassium ions compared to chloride ions (owing to pore selectivity) and a small contribution of migrational flux (opposite to diffusive flux) for potassium ions. Hence, we observe a higher current at all diameters in between the extreme limits. Henceforth, we observe a non-monotonic characteristic in the short-circuit current. Our calculations reveal that continuum based numerical model provides a sufficient proof to explain the mechanism behind the current characteristics observed in the experiments.

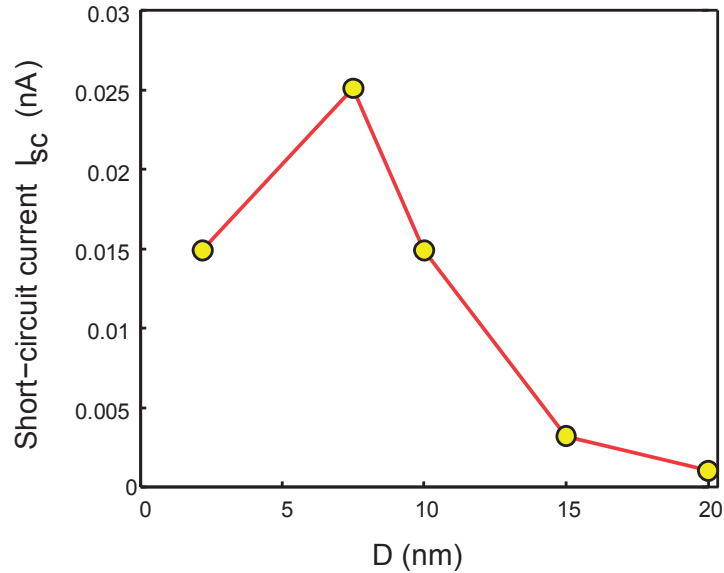


Figure 5.17. Variation of short-circuit current, I_{sc} as a function of the nanopore diameter. The salinity concentration ratio is fixed at 3. The surface charge of the nanopore is $\sigma_n = -0.04694 \text{ C/m}^2$

5.5. Demonstration of a self-powered nanosystem

Considerable energy could be generated by exploiting parallelization with multiple small pores or even a continuous porous structure with a large area of single-layer MoS₂ membrane[215], which can be scaled up for mass-production using the recently reported ECR pore fabrication technique[97] or oxygen plasma-based defect creation[216]. On the other hand, the use of individual nanopores as a micro/nano source has also been expected since a long time[184]. Here, we demonstrate that an individual osmotic generator can also serve as a nano power source for a self-powered nanosystem due to its high efficiency and power density. The power output from individual nanopores is sufficient to drive a nanoelectronic device. Such self-powered nanosystems are of critical importance for independent operation of nanodevices in electronics and biotechnology[217, 218]. For the nanoelectronic device, we choose the recently demonstrated high-performance single-layer MoS₂ transistor due to its excellent operation in low power range[81]. Optical micrograph of transistor itself is shown on **Figure 5.18 a**. Furthermore, we characterize the single-layer MoS₂ transistor in the configuration schematically shown in **Figure 5.18 b**, where we use two nanopores to apply voltages to the drain and gate terminals of our device. The result of transistor characteristics is shown on **Figure 5.18 c**. Varying the top gate voltage of our device in the relatively narrow window of ± 0.78 V, we could modulate the channel conductivity by a factor of 50 to 80. Furthermore, we fix the gate voltage and vary the drain-gate voltage V_s , as shown on **Figure 5.18 c (inset)** and obtain an almost linear I_s-V_s curve demonstrating efficient injection of electrons into the transistor channel.

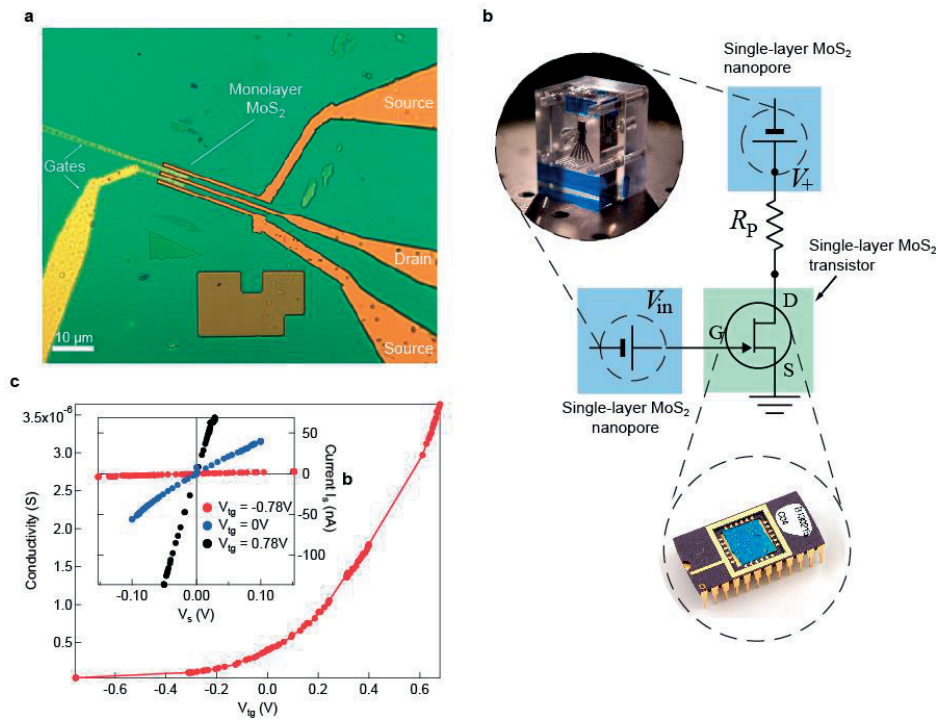


Figure 5.18. Demonstration of a self-powered nanosystem. **a.** Optical image of the fabricated MoS₂ transistor with a designed gate, drain and source electrodes. **b.** Circuit diagram of the self-powered nanosystem where the drain-source supply for MoS₂ transistor is provided by an MoS₂ nanopore while a second nanopore device operates as the gate voltage source **c.** Powering all terminals of the transistor with nanopore generators.

Our measurements show reasonably good correlation with values obtained using standard voltage sources on the same device. For electrical measurements we have used Agilent 5270B SMU, SR-570 low noise current preamplifier and Keithley 2000 DMM (input impedance >1010 Ohm). All measurements were performed in ambient conditions in dark. In dual-gated devices the back gate was grounded for all the measurements.

We compare performance of single-layer MoS₂ transistor in two cases: (i) we use two nanopores to apply V_{tg} and V_{ds}, while using current amplifier and voltmeter to control the current and voltage drop across the device (schematic of the setup is presented on **Figure 5.19 a**), (ii) we use source-meter unit (SMU) to perform standard two-contact measurements. In case (i) we used voltage dividers to change the source and gate voltage on the device (not shown on schematics), as detailed in **Figure 5.19 b**.

Chapter 5. Nanofluidics: ultimate osmotic power generation with 2D membranes

Furthermore, we compare case (i) and (ii). Although the characteristics of our transistor with both setups are similar, we comment on the difference in the ON state conductivity. We attribute it to the slow response of the device in case (i) of nanopore measurements. The change of transistor resistance by application of gate voltage leads to impedance change of the device and thus the applied effective voltage V_{dev} (measured with voltmeter connected in parallel). Nanopore reacts on change of impedance with certain stabilization time (from 10 to 100 of seconds). This appears to be a hysteretic effect and influences the conductivity - gate voltage measurements. In case (ii) on the other hand $V_{dev} = V_s$ is constant.

There are a number of secondary effects, which might in turn influence the measured values of two-probe conductivity. In relatively short channel devices applied V_s might partially contribute to gating of the channel and furthermore to modification of contact resistance. This could be understood comparing the values of V_s (around 100mV) and V_{tg} (780mV). We also could not exclude slight doping variations and hysteresis effects due to filling of trap states inside the transistor channel.

On the other hand, driving a device to the ON state and stabilizing the current for a reasonable amount of time, we could get a very good match in I_s - V_s characteristics, as shown on **Figure 5.19 c**. We thus conclude that although there are differences in performance in both cases which originate mainly from slow response time of nanopore, we could find a good match between the two schemes of measurements. Optimization of the response time of nanopore generators is an interesting task to be conceived in future.

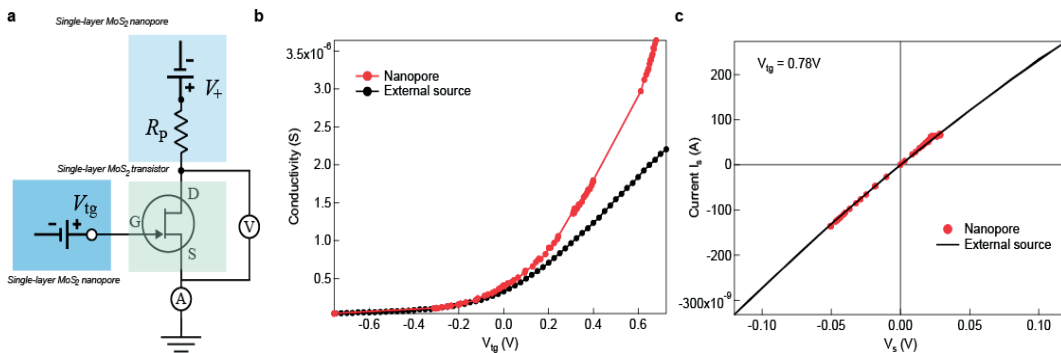


Figure 5.19. Characterization of a single-layer MoS₂ transistor with nanopores and SMU. **a.** Schematic of electrical measurements with two nanopores (V_{ds} and V_{tg}).

Chapter 5. Nanofluidics: ultimate osmotic power generation with 2D membranes

Voltage drop across the transistor channel is monitored with the voltmeter V , current is measured with current amplifier A . **b.** Comparison of nanopore measurements and standard two-probe measurements with external source. **c.** Current-voltage characteristics at $V_{\text{tg}} = 0.78\text{V}$ after current stabilization, measured with both setups.

This system is an ideal self-powered nanosystem in which all the devices are based on single-layer MoS_2 . The range of power generated by single MoS_2 nanopore device could potentially allow powering other nanoelectronic or optoelectronic devices, such as light emitting diodes, logic circuits, or biosensors. Such a system also mimics the cell membrane function where live transistors (ion channels) use membrane potential for transmembrane transport. In addition, our results also suggest that nanoelectronic devices could be osmotically driven by inserting them into cell membranes.

5.6. Single layer MoS_2 membranes for nanofluidics

We have shown that MoS_2 nanopores are promising candidates for investigating osmotic power generation for future renewable blue energy. The giant generated power can be attributed to the ultimate atomic-scale thickness of the MoS_2 membrane and the excellent water permeability of single-layer MoS_2 nanopores[189]. Using a single-component nanopore generator, we power a high-performance single-layer MoS_2 transistor and demonstrate a self-powered nanosystem. These results also provide new avenues for studying other types of membrane-based processes such as, in sea water desalination[189, 216], molecular sieving[219] or proton transport[220]. On the other hand, the nanopore generator could also find applications for other ultra-low power devices, with potential use in future electronics, as transmembrane in-vivo sensing probes or building blocks of artificial cells.

Chapter 6. Conclusion: a single molecule platform to fundamentals and applications

6.1. Conclusion

In this thesis, I have discussed the background of nanopores, described how to make individual MoS₂ nanopores, and presented the use of MoS₂ nanopores for applications in molecular sensing and beyond. To summarize, the key achievements of this thesis are the following,

- **A scalable method based on a controlled electrochemical reaction for MoS₂ nanopore fabrication with atomic precision**

Based on this single MoS₂ nanopore platform, I proposed and experimentally realized,

- **First demonstration of single nucleotide identification in solid-state nanopores**
- **First observation of quantum-like mesoscopic effects in ion transport and providing new understanding for ion channels: ionic Coulomb blockade**
- **First exploration of using a 2-dimensional membrane: single layer MoS₂ nanopores for osmotic power generation**

6.2. Future directions in solid-state nanopore sequencing

Strand sequencing: readout of sequence from an entire DNA molecule is the final goal. I have observed some primary results regarding readout of DNA heteropolymers but the statistical significance is low due to a low number of convincing events. I am integrating the following technical improvements to the current configuration.

- **Ideal solid-state nanopore sequencer: pore size 1.1 to 1.4 nm in a thin membrane (< 1 nm), noise should be as low as possible which can be now achieved by using insulating substrate. MoS₂ can be a good material choice but it can be replaced by any other comparably thin materials which are also not sticky to DNA. Current methods for fabrication of solid-state nanopores result in the large distribution of pore surface charge, chemistry and geometry, although our ECR pore formation technique could**

Chapter 6. Conclusion: a single molecule platform to fundamentals and applications

end up with the same conductance for different pores. We have yet to witness the solid-state nanopore devices as perfect, precise, and reproducible as protein pores and I think this sets the requirement for the next generation of solid-state nanopores[12] which will be the bottom up: self-assembled or synthetic chemistry approach.

- Nanopore array and high throughput: the chip should be an array of nanopores isolated from each other via lithography patterning. The fabrication of such solid-state devices should be scalable at each step, compatible with CMOS technology. A portable device with an integrated amplifier in a physical dimension (< 5 cm).
- The sequencing speed should be regulated according to the state of the art amplifier at highest bandwidth, while still remaining the minimum signal to noise ratio for required sequencing accuracy. An optimized sequencing speed of 10 to 100 nt/ms according to current requirements of the amplifier and device noise[221]. The various choices of ionic liquids and their tunable viscosity might be able to address this issue.
- The fluctuations and reproducibility. Thermal and mechanical induced fluctuations would introduce additional noise to raw data and should be reduced. A temperature regulating system should be integrated to the current configuration. Remeasuring the same molecules should be possible with the feedback control on voltage bias.
- Alternative sequencing route, also including the integration of established sequencing chemistry in other systems. Optical approaches in nanopore sensing have shown their advantages in high throughput and multiplexing [222-224]. However, employing optics may not have much uniqueness compared to single molecule real time sequencing (SMRT, PacBio) that utilizes a zero-mode waveguide[225].
- Two accuracies can be applied to the given sequence: Base-calling accuracy and assembly accuracy. Base-calling identifies the base sequence of different fragments from current signals. Assembly accuracy determines full sequences using different fragmented sequences. Using 1 M bandwidth, human genome sequencing would be done in hours and even minutes by exploiting micro-sequencer array[38].
- Transverse approaches using tunneling and field effect. Both ways will allow fast and high throughput sequencing due to their advantage in multiplexing. The reservoir does not need to be isolated. I think the key advantage lies in the sensitivity and selectivity of the device on identifying individual nucleobases. I would like to propose

Chapter 6. Conclusion: a single molecule platform to fundamentals and applications

a general standard for the future comparison: signal (including signal difference from nucleobases) to noise ratio under the same bandwidth/analysis frequency. The tunneling approach has already demonstrated excellent differentiation ability towards sequencing. Will this also be true with transverse detection with graphene or any other 2-dimensional transistor or quantum point contact? Time will tell.

- Protein sequencing. Identifying peptides which are biomolecules formed by 20 types of amino acids would be more challenging than DNA. Current methods for protein sequencing rely on Edman degradation and mass spectroscopy[226]. Nanopore sequencing platforms should in principle be applied also to single molecule protein sequencing, which is of particular importance since proteins cannot be amplified by PCR as DNA can be. However, due to technical difficulties in determining all levels, I believe this would be a task best undertaken after practical DNA sequencing.

- DNA digital data storage and readout[227]. The possibility of recording, storage and retrieval of information in DNA molecules, originally proposed by Mikhail Neiman[228], would benefit a lot from fast DNA sequencing and might be practical when solid-state sequencing is delivered. DNA can be encoded by nucleobase to store information and a nanopore sequencer would read it. Once this is accomplished, the challenge will go back to DNA synthesis and with fast and cheap synthesis or even long length be practical? Perhaps the concept of nanopore reactors can offer attractive solution for this problem.

6.3. Nanopores: artificial ion channels

I can engineer any size pore according to the needs and these artificial nanopores and can operate at extreme conditions that are not limited by physiological environment and stability of ion channels. For example, solid-state nanopores can bear much higher voltage than ion channels in lipid bilayers. My intention is to verify a physical model with solid-state nanopores, which, from my point of view, is simpler in terms of structure and chemistry than biological ion channels. Accordingly, less dimensions/parameters would need to be considered for the assumptions made before applying these models. In particular, I propose the following investigations,

Chapter 6. Conclusion: a single molecule platform to fundamentals and applications

- Incorporating a voltage gate. The experimental platform is the same as the transverse field effect configuration. The third gate electrode can be employed to adjust the charge state of the pore and therefore one might be able to observe Coulomb oscillations when measuring drain-source transmembrane conductance when the gate voltage is tuned.
- Integrating an optical setup. One should be able to gate the system using light and also observe Coulomb blockade features.

In my opinion, the current biophysics of ion channels contains too many descriptive works and existing models. By designing the ideal experiments with artificial nanopores, interpreting phenomena that are analogous to those encountered in nanoscopic and mesoscopic physics, I hope to provide a general model for ion channels.

6.4. Understanding the membrane-based process from a single nanopore

Membrane based processes are crucial to both living bodies and various engineering fields, f.eg. sea water desalination for island countries, osmotic power generation and molecular sieving. Most of the research works deal with multiple pores, which have distributions in many parameters, resulting in less-conclusive conclusions. In contrast to these, a single nanopore system could largely improve our fundamental understanding of membrane transport and provide useful information for industry-level commercialization.

Chapter 7. Nanopores-Bridging engineering and understanding

This thesis or my motivation at the beginning of the PhD was initiated from solid-state sequencing and it now ends with several experimental topics both in sensing applications and fundamental ion transport.

As a 20 year old field, nanopores are not young anymore and the community has been asking whether nanopore research has passed its plateau or not. Particularly considering the successful release of a protein nanopore sequencer MinION/GridION device from Oxford Nanopore, the rest of the work would be pure engineering efforts since the physics stays the same. Changing the type of proteins in biological pores and materials for solid-state devices would not make any difference to the physics until something new or really unique is discovered. The use of the material molybdenum disulfide in this thesis should also apply also to other 2-dimensional or atomically thin materials. Other sensing applications would just extend the nanopore research to a much broader field. Nanopore sequencing or sequencing is no longer a subject of interest for fundamental research. Therefore, one shall believe that the focus of nanopore research should trend to industry.

To some extent, I agree with the above opinion and next work will be obvious, but still nanopores can deliver unprecedented things beyond sequencing and sensing. Nanopores are a general platform that allows manipulation, measurement, reaction, and integration. I like the word "elegant" for describing nanopores. *"Everything should be made as simple as possible, but not simpler"* Albert Einstein wrote this when he was trying to explain how a good theory should be, like $E = mc^2$. I found this situation also applies to the investigation of nanopores. It is simple: you just measure the current when applying a bias but you can image how informative it is: one could extract much information about ions, biomolecules, particles or even water molecules which almost constitute the whole basic biology that we are watching. More importantly, one could design the structure of the nanopore probe atom by atom according to the needs at different scales. That is the power of engineering in creation!

Chapter 7. Nanopores-Bridging engineering and understanding

Roberts Einsenberg wrote me in email, *"It is easy to miss the physical models of biological channels because there is so much superb descriptive work about ion channels. Some of that is couched in apparently physical language, that does not conform with what physicists call physical language and I find that most physical scientists are put off (i.e., frightened to use the more emotionally relevant words) by this gap between biophysics (as biologists call it) and physics"*. I definitely agree with what he wrote above and believe there is still plenty of room here to make biology a more exact Science. Filling this gap between physics and biophysics is also one of my goals from a career aspect.

I enjoy the interdisciplinary nature of nanopore research. I am a chemist by training through bachelor studies and I started the thesis from the nanopore sensor/sequencer (single nucleotides). The most exciting part of my PhD in physics is the discovery of the single ion transistor (Coulomb blockade). As a trained engineer, I invented the generator in the last part of my PhD. There are tons of known/unknown physics behind this thesis and I love the way to explore it. I believe nanopores can still achieve new and exciting applications beyond sensing, like a single molecule reactor. There is no end and such a single molecule platform should enable many innovations at the boundary of thermal dynamics, and one might be able to observe some interesting new physics. The same should apply to other platforms or physical probes.

To finish, I think we are all ready to see how nanopore sequencing will revolutionize our way of life in the years to come. On the other hand, I hope fundamental research with model system-nanopores will also shed light on what is considered to be the complicated biological ion channels and membrane-based process. Thus, both the commercialized products and fundamental understandings can be made as simple as possible, but of course, not simpler.

Bibliography

1. Feynman, R.P., R.B. Leighton, and M. Sands, *The Feynman Lectures on Physics, Desktop Edition Volume I*. Vol. 1. 2013: Basic books.
2. Wilson, E.O., *Consilience: The unity of knowledge*. Vol. 31. 1999: Vintage.
3. Watson, J.D. and F.H. Crick, *Molecular structure of nucleic acids*. Nature, 1953. **171**(4356): p. 737-738.
4. Selvin, P.R. and T. Ha, *Single-molecule techniques*2008: Cold Spring Harbor Laboratory Press.
5. Deniz, A.A., S. Mukhopadhyay, and E.A. Lemke, *Single-molecule biophysics: at the interface of biology, physics and chemistry*. Journal of the Royal Society Interface, 2008. **5**(18): p. 15-45.
6. Hell, S.W. and J. Wichmann, *Breaking the diffraction resolution limit by stimulated emission: stimulated-emission-depletion fluorescence microscopy*. Optics letters, 1994. **19**(11): p. 780-782.
7. Betzig, E., et al., *Imaging intracellular fluorescent proteins at nanometer resolution*. Science, 2006. **313**(5793): p. 1642-1645.
8. Rust, M.J., M. Bates, and X. Zhuang, *Sub-diffraction-limit imaging by stochastic optical reconstruction microscopy (STORM)*. Nature methods, 2006. **3**(10): p. 793-796.
9. Hamill, O.P., et al., *Improved patch-clamp techniques for high-resolution current recording from cells and cell-free membrane patches*. Pflügers Archiv, 1981. **391**(2): p. 85-100.
10. Watson, J.D., *Molecular biology of the gene*. Molecular biology of the gene., 1970(2nd edn).
11. Sinden, R.R., *DNA structure and function*2012: Elsevier.

12. Wanunu, M., *Nanopores: A journey towards DNA sequencing*. Physics of life reviews, 2012. **9**(2): p. 125-158.
13. Branton, D., et al., *The potential and challenges of nanopore sequencing*. Nature Biotechnology, 2008. **26**(10): p. 1146-1153.
14. Dekker, C., *Solid-state nanopores*. Nature Nanotechnology, 2007. **2**(4): p. 209-215.
15. Hille, B., *Ion channels of excitable membranes*. Vol. 507. 2001: Sinauer Sunderland, MA.
16. Scanziani, M. and M. Häusser, *Electrophysiology in the age of light*. Nature, 2009. **461**(7266): p. 930-939.
17. Channels, I., *Structure and function of voltage-sensitive ion channels*. 1988.
18. Triggle, D.J., *L-type Calcium Channels*. Voltage-Gated Ion Channels as Drug Targets, Volume 29, 2006: p. 100-121.
19. Yellen, G., *The voltage-gated potassium channels and their relatives*. Nature, 2002. **419**(6902): p. 35-42.
20. Vergara, C., et al., *Calcium-activated potassium channels*. Current opinion in neurobiology, 1998. **8**(3): p. 321-329.
21. Deisseroth, K., *Optogenetics*. Nature methods, 2011. **8**(1): p. 26-29.
22. Fenno, L., O. Yizhar, and K. Deisseroth, *The development and application of optogenetics*. Neuroscience, 2011. **34**(1): p. 389.
23. Berneche, S. and B. Roux, *Molecular dynamics of the KcsA K⁺ channel in a bilayer membrane*. Biophysical Journal, 2000. **78**(6): p. 2900-2917.
24. Berneche, S. and B. Roux, *Energetics of ion conduction through the K⁺ channel*. Nature, 2001. **414**(6859): p. 73-77.
25. Branton, D., et al., *The potential and challenges of nanopore sequencing*. Nature Biotechnology, 2008. **26**(10): p. 1146-1153.

26. Song, L., et al., *Structure of staphylococcal α -hemolysin, a heptameric transmembrane pore*. Science, 1996. **274**(5294): p. 1859-1865.
27. Butler, T.Z., et al., *Single-molecule DNA detection with an engineered MspA protein nanopore*. Proceedings of the National Academy of Sciences, 2008. **105**(52): p. 20647-20652.
28. Bayley, H. and L. Jayasinghe, *Functional engineered channels and pores (Review)*. Molecular membrane biology, 2004. **21**(4): p. 209-220.
29. Rotem, D., et al., *Protein detection by nanopores equipped with aptamers*. Journal Of The American Chemical Society, 2012. **134**(5): p. 2781-2787.
30. Howorka, S., S. Cheley, and H. Bayley, *Sequence-specific detection of individual DNA strands using engineered nanopores*. Nature Biotechnology, 2001. **19**(7): p. 636-639.
31. Li, J., et al., *Ion-beam sculpting at nanometre length scales*. Nature, 2001. **412**(6843): p. 166-169.
32. Li, J.L., et al., *DNA molecules and configurations in a solid-state nanopore microscope*. Nature materials, 2003. **2**(9): p. 611-615.
33. Storm, A.J., et al., *Fabrication of solid-state nanopores with single-nanometre precision*. Nature materials, 2003. **2**(8): p. 537-40.
34. Novoselov, K.S., et al., *Electric field effect in atomically thin carbon films*. Science, 2004. **306**(5696): p. 666-669.
35. Garaj, S., et al., *Graphene as a subnanometre trans-electrode membrane*. Nature, 2010. **467**(7312): p. 190-193.
36. Merchant, C.A., et al., *DNA Translocation through Graphene Nanopores*. Nano Letters, 2010. **10**(8): p. 2915-2921.
37. Schneider, G.F., et al., *DNA Translocation through Graphene Nanopores*. Nano Letters, 2010. **10**(8): p. 3163-3167.
38. Di Ventra, M. and M. Taniguchi, *Decoding DNA, RNA and peptides with quantum tunnelling*. Nature Nanotechnology, 2016. **11**(2): p. 117-126.

39. Heerema, S.J. and C. Dekker, *Graphene nanodevices for DNA sequencing*. Nature Nanotechnology, 2016. **11**(2): p. 127-136.
40. Lindsay, S., *The promises and challenges of solid-state sequencing*. Nature Nanotechnology, 2016. **11**(2): p. 109-111.
41. Bell, N.A., et al., *DNA origami nanopores*. Nano Letters, 2011. **12**(1): p. 512-517.
42. Kim, M.J., et al., *Rapid fabrication of uniformly sized nanopores and nanopore arrays for parallel DNA analysis*. Advanced materials, 2006. **18**(23): p. 3149-+.
43. Howorka, S. and Z. Siwy, *Nanopore analytics: sensing of single molecules*. Chemical Society Reviews, 2009. **38**(8): p. 2360-2384.
44. Coulter, W., *Means for counting particles suspended in a fluid*. US Patent, 2656508. United States Patent Office. Patentiert am, 1953. **20**: p. 1953.
45. Kasianowicz, J.J., et al., *Characterization of individual polynucleotide molecules using a membrane channel*. Proceedings of the National Academy of Sciences of the United States of America, 1996. **93**(24): p. 13770-3.
46. Church, G., et al., *Measuring physical properties*, 1998, Google Patents.
47. Laszlo, A.H., et al., *Decoding long nanopore sequencing reads of natural DNA*. Nature Biotechnology, 2014. **32**(8): p. 829-33.
48. Bayley, H., *Nanopore sequencing: from imagination to reality*. Clinical chemistry, 2015. **61**(1): p. 25-31.
49. Manrao, E.A., et al., *Reading DNA at single-nucleotide resolution with a mutant MspA nanopore and phi29 DNA polymerase*. Nature Biotechnology, 2012. **30**(4): p. 349-353.
50. Garaj, S., et al., *Molecule-hugging graphene nanopores*. Proceedings of the National Academy of Sciences of the United States of America, 2013. **110**(30): p. 12192-6.

51. Sathe, C., et al., *Computational investigation of DNA detection using graphene nanopores*. *Acs Nano*, 2011. **5**(11): p. 8842-8851.
52. Wells, D.B., et al., *Assessing graphene nanopores for sequencing DNA*. *Nano Letters*, 2012. **12**(8): p. 4117-4123.
53. Shankla, M. and A. Aksimentiev, *Conformational transitions and stop-and-go nanopore transport of single-stranded DNA on charged graphene*. *Nature communications*, 2014. **5**.
54. Venkatesan, B.M. and R. Bashir, *Nanopore sensors for nucleic acid analysis*. *Nature Nanotechnology*, 2011. **6**(10): p. 615-624.
55. Tabard-Cossa, V., et al., *Noise analysis and reduction in solid-state nanopores*. *Nanotechnology*, 2007. **18**(30): p. 305505.
56. Lee, M.-H., et al., *A low-noise solid-state nanopore platform based on a highly insulating substrate*. *Scientific reports*, 2014. **4**.
57. Liu, S., et al., *Boron nitride nanopores: highly sensitive DNA single-molecule detectors*. *Advanced materials*, 2013. **25**(33): p. 4549-54.
58. Lagerqvist, J., M. Zwolak, and M. Di Ventra, *Fast DNA sequencing via transverse electronic transport*. *Nano Letters*, 2006. **6**(4): p. 779-782.
59. Tsutsui, M., et al., *Identifying single nucleotides by tunnelling current*. *Nature Nanotechnology*, 2010. **5**(4): p. 286-290.
60. Xie, P., et al., *Local electrical potential detection of DNA by nanowire-nanopore sensors*. *Nature Nanotechnology*, 2012. **7**(2): p. 119-125.
61. Traversi, F., et al., *Detecting the translocation of DNA through a nanopore using graphene nanoribbons*. *Nature Nanotechnology*, 2013. **8**(12): p. 939-945.
62. Ohshiro, T., et al., *Single-Molecule Electrical Random Resequencing of DNA and RNA*. *Scientific reports*, 2012. **2**: p. 501.

63. Girdhar, A., et al., *Graphene quantum point contact transistor for DNA sensing*. Proceedings of the National Academy of Sciences, 2013. **110**(42): p. 16748-16753.
64. Liu, H., et al., *Translocation of single-stranded DNA through single-walled carbon nanotubes*. Science, 2010. **327**(5961): p. 64-67.
65. Liu, S., et al., *Boron nitride nanopores: highly sensitive DNA single-molecule detectors*. Advanced materials, 2013. **25**(33): p. 4549-4554.
66. Langecker, M., et al., *Synthetic lipid membrane channels formed by designed DNA nanostructures*. Science, 2012. **338**(6109): p. 932-936.
67. Kwok, H., K. Briggs, and V. Tabard-Cossa, *Nanopore fabrication by controlled dielectric breakdown*. Plos One, 2014. **9**(3): p. e92880.
68. Siwy, Z.S. and S. Howorka, *Engineered voltage-responsive nanopores*. Chemical Society Reviews, 2010. **39**(3): p. 1115-1132.
69. Hoogerheide, D.P., S. Garaj, and J.A. Golovchenko, *Probing surface charge fluctuations with solid-state nanopores*. Physical Review Letters, 2009. **102**(25): p. 256804.
70. Hornblower, B., et al., *Single-molecule analysis of DNA-protein complexes using nanopores*. Nature methods, 2007. **4**(4): p. 315-317.
71. Dudko, O.K., et al., *Extracting kinetics from single-molecule force spectroscopy: nanopore unzipping of DNA hairpins*. Biophysical Journal, 2007. **92**(12): p. 4188-4195.
72. Storm, A.J., et al., *Fast DNA translocation through a solid-state nanopore*. Nano Letters, 2005. **5**(7): p. 1193-1197.
73. Talaga, D.S. and J. Li, *Single-molecule protein unfolding in solid state nanopores*. Journal Of The American Chemical Society, 2009. **131**(26): p. 9287-9297.

74. Langecker, M., et al., *Nanopores Suggest a Negligible Influence of CpG Methylation on Nucleosome Packaging and Stability*. Nano Letters, 2014. **15**(1): p. 783-790.
75. Keyser, U.F., et al., *Direct force measurements on DNA in a solid-state nanopore*. Nature Physics, 2006. **2**(7): p. 473-477.
76. Derrington, I.M., et al., *Subangstrom single-molecule measurements of motor proteins using a nanopore*. Nature Biotechnology, 2015. **33**(10): p. 1073-1075.
77. Lee, J. and H. Bayley, *Semisynthetic protein nanoreactor for single-molecule chemistry*. Proceedings of the National Academy of Sciences, 2015. **112**(45): p. 13768-13773.
78. Venta, K., M. Wanunu, and M. Drndić, *Electrically controlled nanoparticle synthesis inside nanopores*. Nano Letters, 2013. **13**(2): p. 423-429.
79. Siria, A., et al., *Giant osmotic energy conversion measured in a single transmembrane boron nitride nanotube*. Nature, 2013. **494**(7438): p. 455-458.
80. Geim, A.K. and K.S. Novoselov, *The rise of graphene*. Nature materials, 2007. **6**(3): p. 183-191.
81. Radisavljevic, B., et al., *Single-layer MoS₂ transistors*. Nature Nanotechnology, 2011. **6**(3): p. 147-150.
82. Venta, K., et al., *Differentiation of short, single-stranded DNA homopolymers in solid-state nanopores*. ACS Nano, 2013. **7**(5): p. 4629-36.
83. Wanunu, M., et al., *Rapid electronic detection of probe-specific microRNAs using thin nanopore sensors*. Nature Nanotechnology, 2010. **5**(11): p. 807-814.
84. Astier, Y., O. Braha, and H. Bayley, *Toward single molecule DNA sequencing: Direct identification of ribonucleoside and deoxyribonucleoside 5'-monophosphates by using an engineered protein nanopore equipped with a molecular adapter*. Journal Of The American Chemical Society, 2006. **128**(5): p. 1705-1710.

85. Liu, S., et al., *Fast and controllable fabrication of suspended graphene nanopore devices*. *Nanotechnology*, 2012. **23**(8).
86. Xu, Q., et al., *Controllable Atomic Scale Patterning of Freestanding Monolayer Graphene at Elevated Temperature*. *Acs Nano*, 2013. **7**(2): p. 1566-1572.
87. Postma, H.W.C., *Rapid Sequencing of Individual DNA Molecules in Graphene Nanogaps*. *Nano letters*, 2010. **10**(2): p. 420-425.
88. Husale, S., et al., *ssDNA Binding Reveals the Atomic Structure of Graphene*. *Langmuir*, 2010. **26**(23): p. 18078-18082.
89. Schneider, G.F., et al., *Tailoring the hydrophobicity of graphene for its use as nanopores for DNA translocation*. *Nature Communications*, 2013. **4**: p. 2619.
90. Wang, Q.H., et al., *Electronics and optoelectronics of two-dimensional transition metal dichalcogenides*. *Nature Nanotechnology*, 2012. **7**(11): p. 699-712.
91. Radisavljevic, B., M.B. Whitwick, and A. Kis, *Integrated circuits and logic operations based on single-layer MoS₂*. *Acs Nano*, 2011. **5**(12): p. 9934-8.
92. Novoselov, K.S., et al., *Two-dimensional atomic crystals*. *Proceedings of the National Academy of Sciences of the United States of America*, 2005. **102**(30): p. 10451-3.
93. Zhan, Y.J., et al., *Large-Area Vapor-Phase Growth and Characterization of MoS₂ Atomic Layers on a SiO₂ Substrate*. *Small*, 2012. **8**(7): p. 966-971.
94. Liu, K.K., et al., *Growth of Large-Area and Highly Crystalline MoS₂ Thin Layers on Insulating Substrates*. *Nano letters*, 2012. **12**(3): p. 1538-1544.
95. Dumcenco, D., et al., *Large-area epitaxial monolayer MoS₂*. *ACS nano*, 2015. **9**(4): p. 4611-4620.
96. Petrone, N., et al., *Chemical Vapor Deposition-Derived Graphene with Electrical Performance of Exfoliated Graphene*. *Nano letters*, 2012. **12**(6): p. 2751-2756.

97. Feng, J., et al., *Electrochemical reaction in single layer MoS₂: nanopores opened atom by atom*. Nano Letters, 2015. **15**(5): p. 3431.
98. Liu, K., et al., *Atomically thin molybdenum disulfide nanopores with high sensitivity for DNA translocation*. ACS nano, 2014. **8**(3): p. 2504-2511.
99. Karunadasa, H.I., et al., *A Molecular MoS₂ Edge Site Mimic for Catalytic Hydrogen Generation*. Science, 2012. **335**(6069): p. 698-702.
100. Huang, J.L., Y.E. Sung, and C.M. Lieber, *Field-Induced Surface Modification on the Atomic Scale by Scanning Tunneling Microscopy*. Applied Physics Letters, 1992. **61**(13): p. 1528-1530.
101. Bohmisch, M., et al., *Nanostructuring on WSe₂ with the atomic force microscope by a potential controlled electrochemical reaction*. Applied Physics Letters, 1996. **69**(13): p. 1882-1884.
102. Ataca, C., et al., *Mechanical and Electronic Properties of MoS₂ Nanoribbons and Their Defects*. Journal of Physical Chemistry C, 2011. **115**(10): p. 3934-3941.
103. Walker, M.I., et al., *Free-standing graphene membranes on glass nanopores for ionic current measurements*. Applied Physics Letters, 2015. **106**(2): p. 023119.
104. Briggs, K., et al., *Kinetics of nanopore fabrication during controlled breakdown of dielectric membranes in solution*. Nanotechnology, 2015. **26**(8): p. 084004.
105. Kowalczyk, S.W., et al., *Modeling the conductance and DNA blockade of solid-state nanopores*. Nanotechnology, 2011. **22**(31): p. 315101.
106. Puster, M., et al., *Toward sensitive graphene nanoribbon-nanopore devices by preventing electron beam-induced damage*. ACS nano, 2013. **7**(12): p. 11283-9.
107. Fischbein, M.D. and M. Drndic, *Electron beam nanosculpting of suspended graphene sheets*. Applied Physics Letters, 2008. **93**(11).

108. Bonde, J., et al., *Hydrogen evolution on nano-particulate transition metal sulfides*. Faraday Discussions, 2008. **140**: p. 219-231.
109. Beale, M., et al., *Microstructure and formation mechanism of porous silicon*. Applied Physics Letters, 1985. **46**(1): p. 86-88.
110. Hulliger, F., *Structural chemistry of layer-type phases*. Vol. 5. 2012: Springer Science & Business Media.
111. Raillon, C., et al., *Fast and automatic processing of multi-level events in nanopore translocation experiments*. Nanoscale, 2012. **4**(16): p. 4916-4924.
112. Heerema, S.J., et al., *1/f noise in graphene nanopores*. Nanotechnology, 2015. **26**(7): p. 074001.
113. Yusko, E.C., et al., *Controlling protein translocation through nanopores with bio-inspired fluid walls*. Nature Nanotechnology, 2011. **6**(4): p. 253-60.
114. Raillon, C., et al., *Nanopore detection of single molecule RNAP-DNA transcription complex*. Nano letters, 2012. **12**(3): p. 1157-64.
115. Maier, J., *Nanoionics: ion transport and electrochemical storage in confined systems*. Nature materials, 2005. **4**(11): p. 805-815.
116. Valov, I., et al., *Atomically controlled electrochemical nucleation at superionic solid electrolyte surfaces*. Nature materials, 2012. **11**(6): p. 530-535.
117. Clarke, J., et al., *Continuous base identification for single-molecule nanopore DNA sequencing*. Nature Nanotechnology, 2009. **4**(4): p. 265-270.
118. Wanunu, M., et al., *DNA translocation governed by interactions with solid-state nanopores*. Biophysical Journal, 2008. **95**(10): p. 4716-25.
119. Sung, W. and P. Park, *Polymer translocation through a pore in a membrane*. Physical Review Letters, 1996. **77**(4): p. 783.
120. Panja, D., G.T. Barkema, and A.B. Kolomeisky, *Through the eye of the needle: recent advances in understanding biopolymer translocation*. Journal of Physics: Condensed Matter, 2013. **25**(41): p. 413101.

121. Kramers, H.A., *Brownian motion in a field of force and the diffusion model of chemical reactions*. Physica, 1940. **7**(4): p. 284-304.
122. Hänggi, P., P. Talkner, and M. Borkovec, *Reaction-rate theory: fifty years after Kramers*. Reviews of Modern Physics, 1990. **62**(2): p. 251.
123. Fologea, D., et al., *Slowing DNA translocation in a solid-state nanopore*. Nano Letters, 2005. **5**(9): p. 1734-1737.
124. Di Fiori, N., et al., *Optoelectronic control of surface charge and translocation dynamics in solid-state nanopores*. Nature Nanotechnology, 2013. **8**(12): p. 946-51.
125. Kowalczyk, S.W., et al., *Slowing down DNA translocation through a nanopore in lithium chloride*. Nano Letters, 2012. **12**(2): p. 1038-1044.
126. Trepagnier, E.H., et al., *Controlling DNA capture and propagation through artificial nanopores*. Nano Letters, 2007. **7**(9): p. 2824-2830.
127. Peng, H.B. and X.S.S. Ling, *Reverse DNA translocation through a solid-state nanopore by magnetic tweezers*. Nanotechnology, 2009. **20**(18).
128. King, G. and J. Golovchenko, *Probing nanotube-nanopore interactions*. Physical Review Letters, 2005. **95**(21): p. 216103.
129. Soni, G.V. and A. Meller, *Progress toward ultrafast DNA sequencing using solid-state nanopores*. Clinical chemistry, 2007. **53**(11): p. 1996-2001.
130. Meller, A., L. Nivon, and D. Branton, *Voltage-driven DNA translocations through a nanopore*. Physical Review Letters, 2001. **86**(15): p. 3435-3438.
131. Fologea, D., et al., *Detecting single stranded DNA with a solid state nanopore*. Nano letters, 2005. **5**(10): p. 1905-1909.
132. Fologea, D., et al., *DNA conformation and base number simultaneously determined in a nanopore*. Electrophoresis, 2007. **28**(18): p. 3186-3192.
133. Welton, T., *Room-temperature ionic liquids. Solvents for synthesis and catalysis*. Chemical reviews, 1999. **99**(8): p. 2071-2084.

134. Hallett, J.P. and T. Welton, *Room-temperature ionic liquids: solvents for synthesis and catalysis*. 2. Chemical reviews, 2011. **111**(5): p. 3508-3576.
135. Joshi, M.D. and J.L. Anderson, *Recent advances of ionic liquids in separation science and mass spectrometry*. Rsc Advances, 2012. **2**(13): p. 5470-5484.
136. Wang, J.-H., et al., *Direct extraction of double-stranded DNA into ionic liquid 1-butyl-3-methylimidazolium hexafluorophosphate and its quantification*. Analytical chemistry, 2007. **79**(2): p. 620-625.
137. Shimojo, K., et al., *Extractive solubilization, structural change, and functional conversion of cytochrome c in ionic liquids via crown ether complexation*. Analytical chemistry, 2006. **78**(22): p. 7735-7742.
138. Kokorin, A.I., *Ionic liquids: theory, properties, new approaches* 2011: InTech.
139. Keskin, S., et al., *A review of ionic liquids towards supercritical fluid applications*. Journal Of Supercritical Fluids, 2007. **43**(1): p. 150-180.
140. Carda-Broch, S., A. Berthod, and D.W. Armstrong, *Solvent properties of the 1-butyl-3-methylimidazolium hexafluorophosphate ionic liquid*. Analytical and Bioanalytical Chemistry, 2003. **375**(2): p. 191-199.
141. Khupse, N.D., S.R. Kurolikar, and A. Kumar, *Temperature dependent viscosity of mixtures of ionic liquids at different compositions*. Indian Journal of Chemistry Section a-Inorganic Bio-Inorganic Physical Theoretical & Analytical Chemistry, 2010. **49**(5-6): p. 727-730.
142. Feng, J., et al., *Identification of single nucleotides in MoS₂ nanopores*. Nature Nanotechnology, 2015. **10**(12): p. 1070-1076.
143. Davenport, M., et al., *Squeezing Ionic Liquids through Nanopores*. Nano Letters, 2009. **9**(5): p. 2125-2128.
144. Yusko, E.C., R. An, and M. Mayer, *Electroosmotic flow can generate ion current rectification in nano- and micropores*. ACS Nano, 2010. **4**(1): p. 477-87.

145. Chandran, A., D. Ghoshdastidar, and S. Senapati, *Groove Binding Mechanism of Ionic Liquids: A Key Factor in Long-Term Stability of DNA in Hydrated Ionic Liquids?* Journal Of The American Chemical Society, 2012. **134**(50): p. 20330-20339.
146. Tasserit, C., et al., *Pink noise of ionic conductance through single artificial nanopores revisited.* Physical Review Letters, 2010. **105**(26): p. 260602.
147. Simonsson, T., *G-quadruplex DNA structures--variations on a theme.* Biological Chemistry, 2001. **382**(4): p. 621-8.
148. Ding, Y.H., et al., *Binding Characteristics and Molecular Mechanism of Interaction between Ionic Liquid and DNA.* Journal Of Physical Chemistry B, 2010. **114**(5): p. 2033-2043.
149. Cardoso, L. and N.M. Micaelo, *DNA molecular solvation in neat ionic liquids.* Chemphyschem : a European journal of chemical physics and physical chemistry, 2011. **12**(2): p. 275-7.
150. Zhang, P.F., et al., *Ionic liquids with metal chelate anions.* Chemical Communications, 2012. **48**(17): p. 2334-2336.
151. Gershow, M. and J. Golovchenko, *Recapturing and trapping single molecules with a solid-state nanopore.* Nature Nanotechnology, 2007. **2**(12): p. 775-779.
152. Perrin, M.L., E. Burzuri, and H.S.J. van der Zant, *Single-molecule transistors.* Chemical Society Reviews, 2015. **44**(4): p. 902-919.
153. Aviram, A. and M.A. Ratner, *Molecular Rectifiers.* Chemical Physics Letters, 1974. **29**(2): p. 277-283.
154. Nitzan, A. and M.A. Ratner, *Electron transport in molecular wire junctions.* Science, 2003. **300**(5624): p. 1384-1389.
155. Park, J., et al., *Coulomb blockade and the Kondo effect in single-atom transistors.* Nature, 2002. **417**(6890): p. 722-725.
156. Krems, M. and M. Di Ventra, *Ionic Coulomb blockade in nanopores.* Journal of Physics: Condensed Matter, 2013. **25**(6): p. 065101.

157. Zwolak, M., J. Lagerqvist, and M. Di Ventra, *Quantized Ionic Conductance in Nanopores*. Physical Review Letters, 2009. **103**(12).
158. Kaufman, I.K., P. McClintock, and R. Eisenberg, *Coulomb blockade model of permeation and selectivity in biological ion channels*. New Journal of Physics, 2015. **17**(8): p. 083021.
159. Sparreboom, W., A. van den Berg, and J.C.T. Eijkel, *Principles and applications of nanofluidic transport*. Nature Nanotechnology, 2009. **4**(11): p. 713-720.
160. Powell, M.R., et al., *Electric-field-induced wetting and dewetting in single hydrophobic nanopores*. Nature Nanotechnology, 2011. **6**(12): p. 798-802.
161. Jain, T., et al., *Heterogeneous sub-continuum ionic transport in statistically isolated graphene nanopores*. Nature Nanotechnology, 2015. **10**(12): p. 1053-1057.
162. Kurnikova, M.G., et al., *A lattice relaxation algorithm for three-dimensional Poisson-Nernst-Planck theory with application to ion transport through the gramicidin A channel*. Biophysical Journal, 1999. **76**(2): p. 642-656.
163. Feng, J., et al., *Observation of ionic Coulomb blockade in nanopores*. Nature materials, 2016.
164. Gorter, C., *A possible explanation of the increase of the electrical resistance of thin metal films at low temperatures and small field strengths*. Physica, 1951. **17**(8): p. 777-780.
165. Beenakker, C.W.J., *Theory of Coulomb-Blockade Oscillations in the Conductance of a Quantum Dot*. Physical Review B, 1991. **44**(4): p. 1646-1656.
166. Kouwenhoven, L.P., et al., *Electron transport in quantum dots*, in *Mesoscopic electron transport* 1997, Springer. p. 105-214.
167. Fulton, T.A. and G.J. Dolan, *Observation of Single-Electron Charging Effects in Small Tunnel-Junctions*. Physical Review Letters, 1987. **59**(1): p. 109-112.

168. Datta, S., *Electronic transport in mesoscopic systems* 1997: Cambridge university press.
169. Farimani, A.B., K. Min, and N.R. Aluru, *DNA base detection using a single-layer MoS₂*. *Acs Nano*, 2014. **8**(8): p. 7914-7922.
170. Ho, C., et al., *Electrolytic transport through a synthetic nanometer-diameter pore*. *Proceedings of the National academy of Sciences of the United States of America*, 2005. **102**(30): p. 10445-10450.
171. Cervera, J., B. Schiedt, and P. Ramirez, *A Poisson/Nernst-Planck model for ionic transport through synthetic conical nanopores*. *Europhysics Letters*, 2005. **71**(1): p. 35-41.
172. Radenovic, A., et al., *Fabrication of 10 nm diameter hydrocarbon nanopores*. *Applied Physics Letters*, 2008. **93**(18).
173. Parsegian, A., *Energy of an ion crossing a low dielectric membrane: solutions to four relevant electrostatic problems*. *Nature*, 1969. **221**(5183): p. 844-846.
174. Zhang, J., A. Kamenev, and B.I. Shklovskii, *Conductance of ion channels and nanopores with charged walls: A toy model*. *Physical Review Letters*, 2005. **95**(14).
175. Zhang, J., A. Kamenev, and B. Shklovskii, *Ion exchange phase transitions in water-filled channels with charged walls*. *Physical Review E*, 2006. **73**(5): p. 051205.
176. Richards, L.A., et al., *Quantifying barriers to monovalent anion transport in narrow non-polar pores*. *Physical Chemistry Chemical Physics*, 2012. **14**(33): p. 11633-11638.
177. Stein, D., M. Kruithof, and C. Dekker, *Surface-charge-governed ion transport in nanofluidic channels*. *Physical review letters*, 2004. **93**(3): p. 035901.
178. Lee, J., et al., *Stabilization of graphene nanopore*. *Proc. Natl Acad. Sci. USA*, 2014. **111**(21): p. 7522-7526.

179. Schneider, W.-D., *Coulomb blockade phenomena observed in supported metallic nanoislands*. *Frontiers in Physics*, 2013. **1**: p. 13.
180. Romero, H.E. and M. Drndic, *Coulomb blockade and hopping conduction in PbSe quantum dots*. *Physical Review Letters*, 2005. **95**(15).
181. Iqbal, M., *An introduction to solar radiation*2012: Elsevier.
182. Pattle, R., *Production of electric power by mixing fresh and salt water in the hydroelectric pile*. *Nature*, 1954. **174**: p. 660.
183. Loeb, S., *Osmotic Power-Plants*. *Science*, 1975. **189**(4203): p. 654-655.
184. Kim, D.-K., et al., *Power generation from concentration gradient by reverse electrodialysis in ion-selective nanochannels*. *Microfluidics and nanofluidics*, 2010. **9**(6): p. 1215-1224.
185. <http://www.wetsalt.nl/participanten.htm>.
186. Lee, C., et al., *Large apparent electric size of solid-state nanopores due to spatially extended surface conduction*. *Nano letters*, 2012. **12**(8): p. 4037-4044.
187. Shan, Y., et al., *Surface modification of graphene nanopores for protein translocation*. *Nanotechnology*, 2013. **24**(49): p. 495102.
188. Ge, P., et al., *Hydrogen evolution across nano-Schottky junctions at carbon supported MoS₂ catalysts in biphasic liquid systems*. *Chemical Communications*, 2012. **48**(52): p. 6484-6486.
189. Heiranian, M., A.B. Farimani, and N.R. Aluru, *Water desalination with a single-layer MoS₂ nanopore*. *Nature communications*, 2015. **6**.
190. Liu, X., et al., *Top-down fabrication of sub-nanometre semiconducting nanoribbons derived from molybdenum disulfide sheets*. *Nature communications*, 2013. **4**: p. 1776.
191. Logan, B.E. and M. Elimelech, *Membrane-based processes for sustainable power generation using water*. *Nature*, 2012. **488**(7411): p. 313-319.

192. Vlassiouk, I., S. Smirnov, and Z. Siwy, *Ionic selectivity of single nanochannels*. Nano letters, 2008. **8**(7): p. 1978-1985.
193. Bocquet, L. and E. Charlaix, *Nanofluidics, from bulk to interfaces*. Chemical Society Reviews, 2010. **39**(3): p. 1073-1095.
194. Cao, L., et al., *Towards understanding the nanofluidic reverse electrodialysis system: well matched charge selectivity and ionic composition*. Energy & Environmental Science, 2011. **4**(6): p. 2259-2266.
195. Herino, R., et al., *Porosity and pore size distributions of porous silicon layers*. Journal of the electrochemical society, 1987. **134**(8): p. 1994-2000.
196. Weinstein, J.N. and F.B. Leitz, *Electric power from differences in salinity: the dialytic battery*. Science, 1976. **191**(4227): p. 557-559.
197. Audinos, R., *Reverse electrodialysis. Study of the electric energy obtained by mixing two solutions of different salinity*. Journal of Power Sources, 1983. **10**(3): p. 203-217.
198. Turek, M. and B. Bandura, *Renewable energy by reverse electrodialysis*. Desalination, 2007. **205**(1): p. 67-74.
199. Suda, F., T. Matsuo, and D. Ushioda, *Transient changes in the power output from the concentration difference cell (dialytic battery) between seawater and river water*. Energy, 2007. **32**(3): p. 165-173.
200. Veerman, J., et al., *Reverse electrodialysis: Comparison of six commercial membrane pairs on the thermodynamic efficiency and power density*. Journal of Membrane Science, 2009. **343**(1): p. 7-15.
201. Wu, J., et al., *Electrophoretically induced aqueous flow through single-walled carbon nanotube membranes*. Nature Nanotechnology, 2012. **7**(2): p. 133-139.
202. Plimpton, S., *Fast parallel algorithms for short-range molecular dynamics*. Journal of computational physics, 1995. **117**(1): p. 1-19.
203. Hockney, R.W. and J.W. Eastwood, *Computer simulation using particles* 1988: CRC Press.

204. Nosé, S., *A unified formulation of the constant temperature molecular dynamics methods*. The Journal of chemical physics, 1984. **81**(1): p. 511-519.
205. Hoover, W.G., *Canonical dynamics: equilibrium phase-space distributions*. Physical Review A, 1985. **31**(3): p. 1695.
206. Barati Farimani, A. and N. Aluru, *Spatial diffusion of water in carbon nanotubes: from fickian to ballistic motion*. The Journal of Physical Chemistry B, 2011. **115**(42): p. 12145-12149.
207. Liang, T., S.R. Phillpot, and S.B. Sinnott, *Parametrization of a reactive many-body potential for Mo-S systems*. Physical Review B, 2009. **79**(24): p. 245110.
208. Joung, I.S. and T.E. Cheatham III, *Determination of alkali and halide monovalent ion parameters for use in explicitly solvated biomolecular simulations*. The Journal of Physical Chemistry B, 2008. **112**(30): p. 9020-9041.
209. Wu, Y. and N. Aluru, *Graphitic carbon-water nonbonded interaction parameters*. The Journal of Physical Chemistry B, 2013. **117**(29): p. 8802-8813.
210. Probstein, R.F., *Physicochemical hydrodynamics: an introduction* 2005: John Wiley & Sons.
211. <http://www.openfoam.com/> (2011).
212. Nandigana, V.V. and N. Aluru, *Understanding anomalous current-voltage characteristics in microchannel-nanochannel interconnect devices*. Journal of colloid and interface science, 2012. **384**(1): p. 162-171.
213. Nandigana, V.V. and N. Aluru, *Nonlinear Electrokinetic Transport Under Combined AC and DC Fields in Micro/Nanofluidic Interface Devices*. Journal of Fluids Engineering, 2013. **135**(2): p. 021201.
214. Nandigana, V.V. and N. Aluru, *Characterization of electrochemical properties of a micro-nanochannel integrated system using computational impedance spectroscopy (CIS)*. Electrochimica Acta, 2013. **105**: p. 514-523.

215. Waduge, P., et al., *Direct and scalable deposition of atomically thin low-noise MoS₂ membranes on apertures*. ACS nano, 2015. **9**(7): p. 7352-7359.
216. Surwade, S.P., et al., *Water desalination using nanoporous single-layer graphene*. Nature nanotechnology, 2015. **10**(5): p. 459-464.
217. Tian, B., et al., *Coaxial silicon nanowires as solar cells and nanoelectronic power sources*. Nature, 2007. **449**(7164): p. 885-889.
218. Xu, S., et al., *Self-powered nanowire devices*. Nature nanotechnology, 2010. **5**(5): p. 366-373.
219. Joshi, R., et al., *Precise and ultrafast molecular sieving through graphene oxide membranes*. Science, 2014. **343**(6172): p. 752-754.
220. Walker, M.I., et al., *Measuring the proton selectivity of graphene membranes*. Applied Physics Letters, 2015. **107**(21): p. 213104.
221. Rosenstein, J.K., et al., *Integrated nanopore sensing platform with sub-microsecond temporal resolution*. Nature methods, 2012. **9**(5): p. 487-492.
222. Ivankin, A., et al., *Label-free optical detection of biomolecular translocation through nanopore arrays*. Acs Nano, 2014. **8**(10): p. 10774-10781.
223. Anderson, B.N., et al., *Probing solid-state nanopores with light for the detection of unlabeled analytes*. Acs Nano, 2014. **8**(11): p. 11836-11845.
224. Huang, S., et al., *High-throughput optical sensing of nucleic acids in a nanopore array*. Nature Nanotechnology, 2015.
225. Eid, J., et al., *Real-time DNA sequencing from single polymerase molecules*. Science, 2009. **323**(5910): p. 133-138.
226. Shevchenko, A., et al., *Mass spectrometric sequencing of proteins from silver-stained polyacrylamide gels*. Analytical chemistry, 1996. **68**(5): p. 850-858.
227. Church, G.M., Y. Gao, and S. Kosuri, *Next-generation digital information storage in DNA*. Science, 2012. **337**(6102): p. 1628-1628.
228. <https://sites.google.com/site/msneiman1905/eng>.

Jiandong Feng

Laboratory of Nanoscale Biology, Institute of Bioengineering, School of Engineering
Swiss Federal Institute of Technology in Lausanne (EPFL)
Route Cantonale, 1015 Lausanne, Switzerland
jiandong.feng@epfl.ch

Born: 08 Jan 1992, China

Current Position

Doctoral Assistant (PhD student). Advisor: Prof. Aleksandra Radenovic

Education

2013-2016 **Swiss Federal Institute of Technology in Lausanne (EPFL)**
PhD Candidate in Physics (admitted as exceptional PhD student without Master degree)
Max Planck-EPFL Center for Molecular Nanoscience and Technology
Doctoral School for Nanoscience and Technology
Planned PhD defense in June 2016

2009-2013 **Zhejiang University**
Bachelor of Science
Major: Chemistry

Current Research

I am working on developing and applying nanopore tools (MoS_2 pore) to probe biology and physics at single molecule level, with multiple interests from quantum mechanics, Coulomb blockade, electrochemistry, nanofabrication, single molecule techniques, nanofluidics, to next generation DNA sequencing. On the application side of my research, I demonstrated the identification of single nucleotides in MoS_2 nanopores, for the first time in the field of solid-state nanopores. I also invented a scalable method for mass production of individual nanopores using controlled electrochemistry with atomic precision. I aim to realize solid-state nanopore sequencing. On the other side, I am also interested in fundamentals of biophysics and based on nanopore experiment, I discovered Coulomb blockade for the first time in ionic transport, as the counterpart of quantum dots, and proposed a new mesoscopic understanding for ion channel transport. From an engineering perspective, measurements with individual nanopores can also further our fundamental understanding of membrane based processes. I realized the ultimate osmotic power conversion for the first time with a two-dimensional membrane.

Publication

Osmotic power generation measured with single-layer MoS_2 nanopores
8. Jiandong Feng*, Michael Graf, Ke Liu, Dmitry Ovchinnikov, Dumitru Dumcenco, Mohammad Heiranian, Vishal Nandigana, Narayana R Aluru, Andras Kis, Aleksandra

Radenovic*, Single-layer MoS₂ nanopores as osmotic nanopower generators, accepted in **Nature** (corresponding author)

Ionic coulomb blockade

7. Jiandong Feng*, Ke Liu, Michael Graf, Dumitru Dumcenco, Andras Kis, Massimiliano Di Ventra, Aleksandra Radenovic*. Observation of ionic Coulomb blockade in nanopores. **Nature Materials**, 2016, DOI:10.1038/nmat4607 (corresponding author)

First instance of quantum-like mesoscopic effects in ion transport and providing new understanding for ion channels, featured on EPFL news, Science Daily, Phys.org, et al.

MoS₂ nanopore DNA sequencing approach

6. Jiandong Feng, et al. Identification of single nucleotides in MoS₂ nanopores. **Nature Nanotechnology**, 2015, DOI: 10.1038/nnano.2015.219.

First realization of single nucleotides identification in solid-state nanopores field, featured on EPFL news, Science Daily, GenomeWeb, Phys.org, et al.

Scalable nanopore fabrication method: ECR

5. Jiandong Feng, et al. Electrochemical reaction in single-layer MoS₂: nanopores opened atom by atom. **Nano letters**, 2015, 15(5): 3431-3438.

A scalable method for nanopore fabrication with atomic precision, featured on EPFL STI news

4. Ke Liu, Jiandong Feng, Andras Kis, Aleksandra Radenovic. Atomically Thin Molybdenum Disulfide Nanopores with High Sensitivity for DNA Translocation. **ACS Nano**, 2014, 8(3): 2504-2511

Undergraduate publications

3. Xiao Li; Jie Tan; Jiekai Yu; Jiandong Feng; Aiwu Pan; Shu Zheng; Jianmin Wu. **Analytica chimica acta**, 2014, 849, 27-35. (Undergraduate work on mass spectra)

2. Jiandong, Feng; Jianmin Wu. **Small**, 2012, 8, 24, 3786–3790. (Undergraduate work on electrochemistry)

1. Jiandong, Feng; Weijie, Zhao; Bin, Su; Jianmin, Wu. **Biosensor and Bioelectronics**, 2011, 30, 21-27. (Summer work on optical sensors in first college year)

Patents

1. Jiandong Feng, Ke Liu, Aleksandra Radenovic, MOLECULAR SENSING DEVICE. WO2015121394

2. Jiandong Feng, Ke Liu, Aleksandra Radenovic, NANOPORE FORMATION METHOD, EU/WO pending

Conferences and Presentations

1. *"Nanosensor for DNA detection"*. The 3rd Chinese Analytical Chemistry Meeting for Life Sciences, Peking University, China, August 19-22, 2010.
2. *"Novel nanosensor based on DNA nanolock"*. The 243rd ACS National Meeting, San Diego, United States, March 25-29, 2012. (Oral)
3. *"Secondary Biosensors"*. 2012 National Symposium on Micro/NanoScale Bioseparations and Bioanalysis, 7th National Conference on Micro Total Analysis Systems & 3rd International (West Lake) Forum on Microfluidic Analysis, Hangzhou, China, 23-25 April, 2012.
4. *"Atomically Thin Molybdenum Disulfide Nanopores with High Sensitivity for DNA Translocation"*. DNA in Nanotechnology Forum. Chalmers, Sweden, 27-28, November, 2013.
5. *"DNA translocation through MoS₂ nanopores"*. Gordon Research Conference: Single Molecule Approaches to Biology, Lucca, Italy, 13-18, July 2014.
6. CECAM workshop, EPFL, Switzerland, 29-31, October, 2014
7. *"Reading single nucleotides in MoS₂ nanopores"*. Swissnanopore conference, Lenzerheide, Switzerland, 22-27, March, 2015
8. *"Identification of single nucleotides in MoS₂ nanopores"*. Gordon Research Conference: Nanomechanical interface, HongKong, China, 19-24, July, 2015
9. *"Probing single DNA nucleotides with MoS₂ nanopores"*. International Symposium on Chemical Biology, Geneva, 13-15, January, 2016
10. *"Observation of ionic Coulomb blockade in nanopores"*. International Conference on Biological Oscillations, Lancaster, 10-14, April, 2016 (Oral presentation in the special section of multi-ion dynamics and Coulomb blockade oscillations in biological ion channels)
11. *"Probing chemical structures and physical processes with nanopores"* The 7th International Symposium on Bioanalysis, Biomedical Engineering and Nanotechnology, Changsha, China, May, 2016 (Invited speaker).

Teaching Activities

Teaching assistant, Fundamentals of biophotonics, master course for bioengineering students in EPFL (Prof. Aleksandra Radenovic)

Teaching assistant, Fundamentals of biosensors and electronic biochips, master course for bioengineering, chemistry and electrical engineering, life science students in EPFL (Prof. Carlotta Guiducci)

Honors and Awards

1. Chinese Government Award for Outstanding Self-Financed Students Abroad,

2015

2. Gordon Research Conference Graduate Students Travel Award, 2014
3. First Prize of Research and Innovation of Zhejiang University, 2012
4. First Prize of Research and Innovation of Zhejiang University, 2011
5. Featured twice by Department of Chemistry in Zhejiang University as outstanding undergraduate student
http://www.chem.zju.edu.cn/chinese/redirect.php?catalog_id=496&object_id=29623
http://www.chem.zju.edu.cn/chinese/redirect.php?catalog_id=184&object_id=36274
6. Featured as the website cover of Institute of Bioengineering in EPFL for the month of April 2016
<http://bioengineering.epfl.ch/page-114862.html>

